Delft University of Technology

Strategies of tailoring 2D MXenes for enhancing Sulfur-Based battery performance

Wang, Hao; de Kogel, Albert; Wang, Zerui; Zou, Rujia; Wang, Xuehang

DOI
10.1016/j.cej.2025.159924

Publication date
2025

Document Version
Final published version

Published in
Chemical Engineering Journal

Citation (APA)
Wang, H., de Kogel, A., Wang, Z., Zou, R., & Wang, X. (2025). Strategies of tailoring 2D MXenes for enhancing Sulfur-Based battery performance. *Chemical Engineering Journal*, *506*, Article 159924. https://doi.org/10.1016/j.cej.2025.159924

Chemical Engineering Journal 506 (2025) 159924

Contents lists available at ScienceDirect

Chemical Engineering Journal

journal homepage: www.elsevier.com/locate/cej

Review

Strategies of tailoring 2D MXenes for enhancing Sulfur-Based battery performance

Hao Wang [a,b], Albert de Kogel [a], Zerui Wang [a], Rujia Zou [b], Xuehang Wang [a,*]

[a] *Department of Radiation Science and Technology, Faculty of Applied Sciences, Delft University of Technology, Mekelweg 15, 2629JB, Delft, the Netherlands*
[b] *State Key Laboratory for Modification of Chemical Fibers and Polymer Materials, College of Materials Science and Engineering, Donghua University, Shanghai 201620, China*

ARTICLE INFO

Keywords:
MXene
MXene modification
Li-S batteries
Sulfur-based batteries
Energy storage

ABSTRACT

MXenes, a thriving class of two-dimensional (2D) transition metal carbides, nitrides, and carbonitrides, demonstrate considerable potential in diverse electrochemical energy storage applications. To leverage MXenes for high-performance sulfur-based batteries, researchers have employed various strategies to modify their properties, aiming to tackle challenges such as the notorious shuttle effect induced by soluble polysulfides, sluggish redox reaction kinetics, and substantial volume expansion during the lithiation process. This review article offers an overview of MXene modification strategies, emphasizing their significant potential in adjusting the composition, surface chemistry, and morphology to address one or more challenges specially in sulfur cathodes. We first discuss internal regulation methods of MXene, including surface group engineering, heteroatom doping, and high-entropy MXene synthesis, which have been demonstrated to enhance MXene-polysulfide interactions and facilitate polysulfide conversion. Subsequently, we provide a summary of the recent design methods and advancements made in MXene-derived and MXene-based composites, with a particular emphasis on electronic structure reconstruction at the heterointerface and their synergistic roles in Li-S batteries. Following this, we outline the utilization of MXenes to address the challenges encountered in metal-sulfur batteries beyond Li-S batteries. Concluding the review, we offer prospects for the future development of utilizing MXenes in practical sulfur-based batteries.

1. Introduction

Sustainable development in modern society aims to reduce fossil fuel consumption and CO_2 emissions, which drives the rapid development of energy storage technologies [1]. Lithium-ion batteries (LIBs) have achieved tremendous success for energy storage in portable electronics, electric vehicles, and smart energy storage grids [2,3]. However, LIBs are approaching their energy density limit (420 Wh kg^{-1}, 1400 Wh L^{-1}), and their raw materials are expensive and have limited resources. To address the escalating demand for large-scale and high-density energy storage, researchers have been exploring next-generation energy storage devices beyond LIBs to facilitate advancements in technologies such as long-range electric vehicles [4–6]. Sulfur is a promising electrode material due to its natural abundance and high theoretical capacity (~1672 mAh g^{-1}). Sulfur can serve as cathode materials to couple with several metal anodes, such as univalent metals (Li, Na, and K) and multivalent metals (Ca, Mg, and Al) [7].

Among all metal-sulfur battery systems, lithium-sulfur (Li-S) battery is the most widely studied due to its highest theoretical gravimetric energy density of 2672 Wh kg^{-1} [6,8]. However, several notorious problems particularly related to sulfur cathodes hinder the commercialization of Li-S batteries [9]. First, both sulfur (S_8) and its discharge product lithium sulfide (Li_2S) are electronically insulating, which leads to slow reaction rate and very low utilization of active materials [10]. During electrochemical cycling in the Li-S system, charges are stored via a multi-step reaction, which forms intermediate products known as “lithium polysulfides” (Li_2S_n, $3 \leq n \leq 8$, or LiPS). LiPS are soluble in ether-based electrolytes, causing rapid capacity decay through the shuttle effect as the schematic illustration in Fig. 1a [11,12]. Furthermore, the final discharge step is a solid–solid transformation from Li_2S_2 to Li_2S, contributing half of the theoretical capacity. In reality, this reaction is difficult to complete due to its high activation barrier, limiting the practical capacity of Li-S batteries (Fig. 1b) [13–15]. Lastly, the structural integrity of the electrode is compromised by the 80% volume

---

* Corresponding author.
E-mail address: x.wang-22@tudelft.nl (X. Wang).

https://doi.org/10.1016/j.cej.2025.159924
Received 23 October 2024; Received in revised form 31 December 2024; Accepted 23 January 2025

expansion after sulfur lithiation, leading to contact loss between the electrode and the current collector and, consequently, battery failure [16].

Many efforts have been made to address the challenges in Li-S batteries, including improving the conductivity, confining sulfur species, and introducing electrocatalysts. Various carbon materials such as mesoporous carbon [17], carbon nanotubes [18], and graphene [19], were employed as sulfur host materials to adapt the volume change and improve the electrode conductivity. Due to their insufficient adsorption to soluble polysulfides, carbon materials failed to address the severe shuttle effect (Fig. 1b). Polar materials with higher binding energies to LiPS, such as TiO_2 [20] and MoS_2 [21], can effectively inhibit the shuttle effect. However, the sluggish reaction kinetics of sulfur species remain a major challenge in achieving a satisfactory capacity. More recently, facilitating polysulfides conversion with catalysts has been regarded as a crucial method to improving reaction rate and addressing the shuttling phenomenon [22]. High catalytic activity is typically associated with a strong adsorption of polysulfides on the catalysts [23,24]. A trapping-diffusion-conversion mechanism further elucidates the conversion pathways of LiPS on electrocatalysts, underscoring that the optimal cathode requires both strong adsorptive and active catalytic capabilities [25]. Novel electrode materials that can fulfill all these criteria are still in the developmental stage.

An emerging family of 2D transition metal carbides, nitrides, and carbonitrides, known as MXenes, has garnered significant attention in the realm of electrochemical energy storage applications [26–28]. MXene exhibits a range of desirable properties for energy storage applications, including its flexible layered structure, tunable surface groups, high conductivity, and robust mechanical strength [29]. However, pristine MXene synthesized via the etching method exhibits limited adsorption ability and inferior electrochemical catalytic effect for sulfur species, posing challenges in achieving satisfactory Li-S electrochemical performance. For example, the electrochemical properties of MXenes are highly related to their surface terminal groups. MXenes with –F and –OH groups generally demonstrate higher conductivity but lower adsorption abilities for LiPS compared to those with –O terminations [30–32]. MXenes also encounter significant restacking issues, which limit the ion accessibility to their interlayer space [33]. However, it is possible to modify MXenes to enhance their functions in Li-S batteries thanks to their diverse composition, tunable surface chemistry and flexible interlayer space. MXene can also be fabricated into MXene-based hybrids to provide characteristics that cannot be achieved by a single material [34]. More importantly, MXenes can deliver superb catalytic capabilities to facilitate the conversion of LiPS through appropriate modification, thereby improving the electrochemical reaction kinetics for outstanding battery performance (Fig. 1b) [35]. MXene has garnered tremendous attention with the number of publications increasing by over 350% in the past five years from 2019 to 2023 (Fig. 1c). The initial exploration of MXene in Li-S batteries was published in 2015 [36], followed by rapid development (Fig. 1 d, e). Despite several review papers discussing the application and history of MXene in sulfur-based batteries [37,38], there is still a lack of a comprehensive review specifically focusing on strategies for modifying MXenes, including pure MXenes, MXene derivatives, and MXene composites, to achieve specific functions to enhance sulfur-based batteries performance.

Herein, we present a review summarizing the design and modification strategies and recent processes of MXenes aimed at enhancing the performance of sulfur-based batteries. As illustrated in Fig. 2, we commence this review with the fundamental properties, composition, and synthesis methods of MXene. These aspects elucidate MXene's potential for application in sulfur-based batteries, laying the foundation for

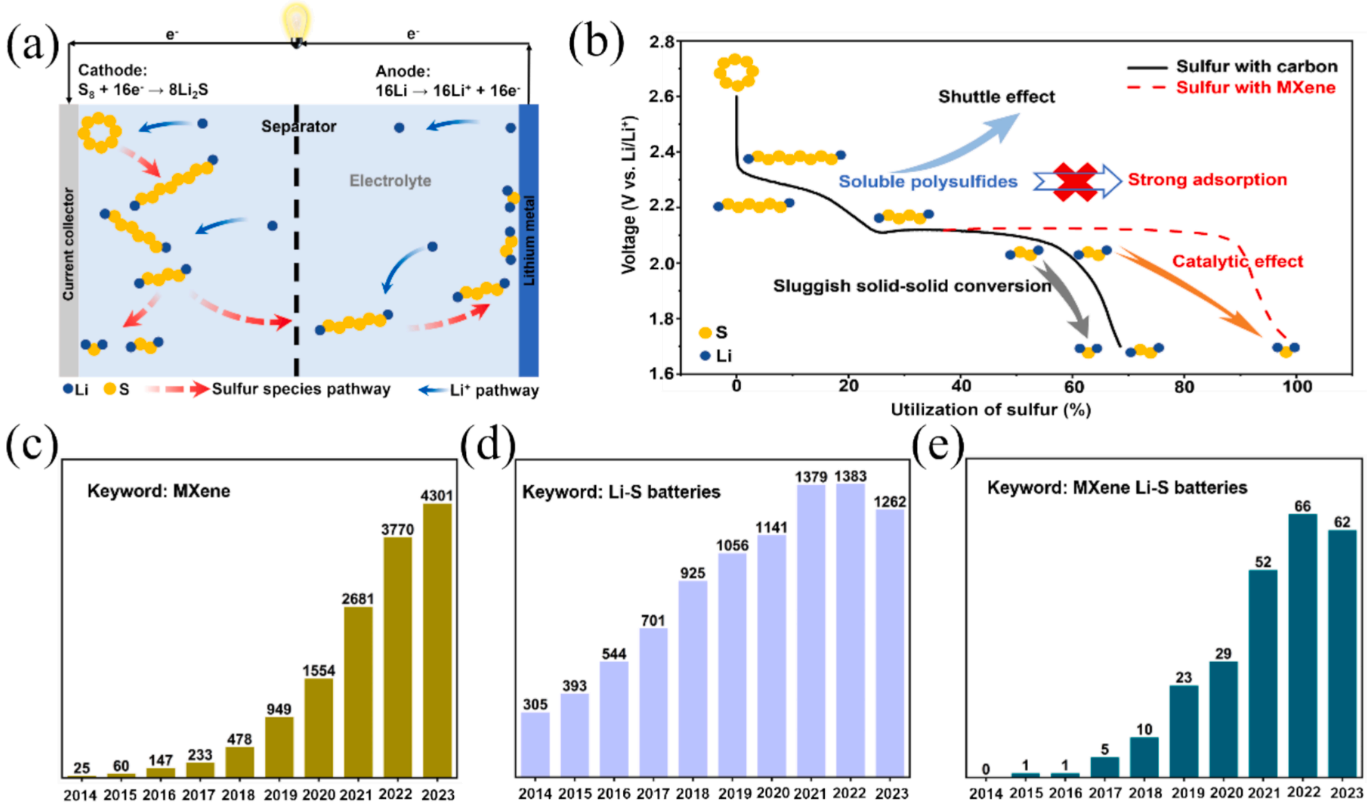

Fig. 1. (a) A schematic illustration of the sulfur reduction process in Li-S batteries. (b) Discharge profile of sulfur with carbon as cathode, the dashed red line represents the expected discharge profile by sulfur with MXene as cathode. Annual number of publications from 2014 to 2023 based on Web of Science using the keyword (c) "MXene", (d) "Li-S batteries", and (e) "MXene Li-S batteries", respectively. (For interpretation of the references to color in this figure legend, the reader is referred to the web version of this article.)

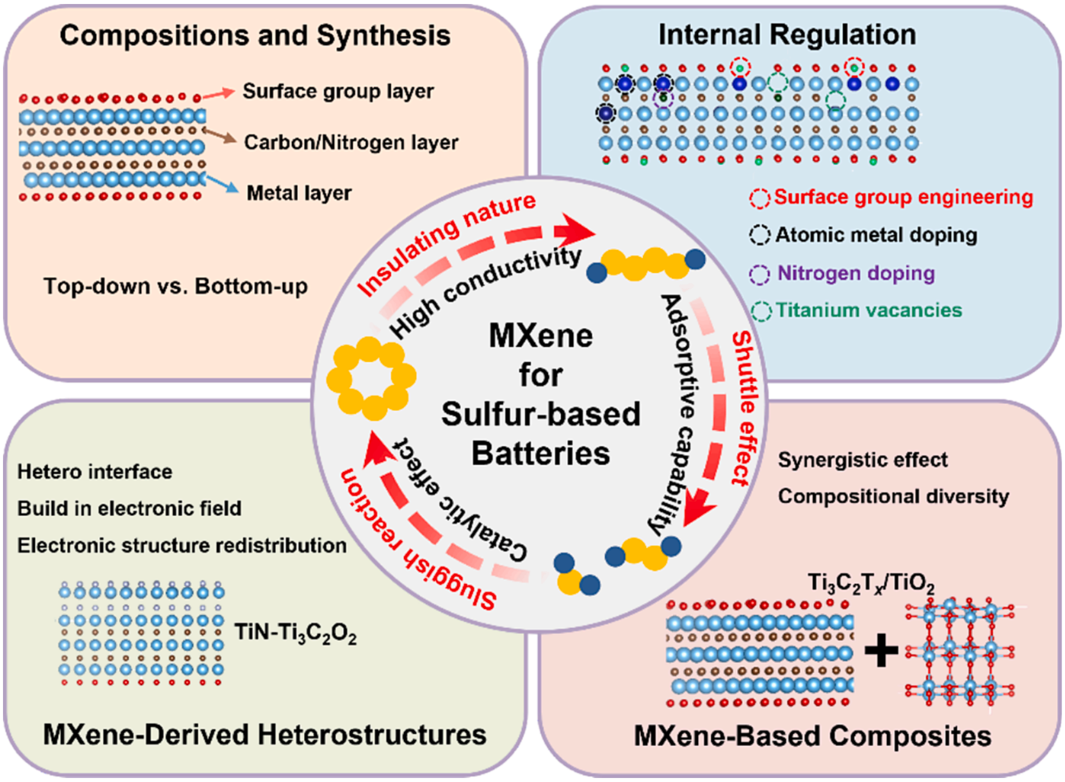

Fig. 2. A schematic illustration of the highlight of this review, including compositions and synthesis of MXene, various design and modification methods of MXene for high performance sulfur-based batteries.

all subsequent discussions. Following this, we categorize and summarize various design and modification methods of MXene tailored to address the challenges faced by sulfur cathodes. This includes internal regulation of MXene such as surface group engineering, atomic doping, and the preparation of high-entropy MXene to enhance the interaction between MXene and LiPS. Next, our focus shifts to the in-situ formation of heterostructures derived from MXene, highlighting the importance of reconstructing chemical composition, band structure, and electronic properties at the heterointerface and their impact on Li-S electrochemistry. Furthermore, we outline the fabrication of MXene-based hybrids and delve into the principles of combining MXene with other materials to achieve synergistic effects that single materials cannot provide. Inspired by the achievements of MXene in Li-S batteries, we broaden our discussion to encompass its potential in addressing challenges across various other metal-sulfur batteries. Finally, we outline the remaining challenges and offer prospects for further developing MXene-based Li-S and other metal-sulfur batteries.

2. Mxene composition and synthesis

The chemical formula of MXene is represented as $M_{n+1}X_nT_x$, where M stands for early transition metals, X denotes carbon and/or nitrogen, n is an integer ranging from 1 to 4, and T_x stands for surface groups (Fig. 3a) [34]. To date, over 50 distinct MXenes have been synthesized, with computational methods predicting thousands more MXene compositions [39]. The most common MXenes are single transition metal MXenes, such as Ti_2CT_x [40], V_2CT_x [41], Ti_2NT_x [42], $Ti_4N_3T_x$ [43], and the metal-vacancy-containing $Mo_{1.33}C$ [44]. For MXenes with two metal species, two forms exist: MXenes with ordered double-metal structure and MXenes with solid solution structure, as shown in Fig. 3b. For example, $Mo_2TiC_2T_x$ and $Mo_2Ti_2C_3T_x$ are arranged in the order of Mo-Ti-Mo and Mo-Ti-Ti-Mo, respectively [45]. Meanwhile, two different metal atoms randomly occupy the M−sites in solid solution MXenes, such as $Ti_yNb_{2-y}CT_x$ and $Nb_yV_{2-y}CT_x$ [46]. Inspired by advancements in the field of high-entropy compounds, high-entropy MXenes with at least four metal species have been recently developed [47,48]. Density functional theory (DFT) simulation has revealed that increasing the number of metal species leads to enhanced stability, following the entropy-stabilization principle [48].

Based on the currently available MXene synthesis methods, the synthesis route can be roughly categorized into top-down and bottom-up methods. In the top-down method, MXenes are acquired through the selective removal of the A layers from the MAX ($M_{n+1}AX_n$) phase. Notably, A represents A-group elements in the periodic table, primarily IIIA and IVA elements such as Al and Si. HF etching is the earliest and the most widely used method to etch the MAX phase (Fig. 3c) [49]. Following the etching step, an intercalating agent is frequently employed to transform the compact MXene structure into an expanded accordion-like stacked structure, after which mechanical exfoliation (such as ultrasonic treatment) is carried out to obtain single or few layers of MXene. Commonly used intercalating agents include dimethyl sulfoxide [50], urea [51], and isopropyl amine [42]. Due to the toxicity and practical hazards associated with HF, etchants combined with fluoride salts and hydrochloric acid (e.g., LiF-HCl) have been employed as substitutes for HF for synthesizing MXene [52]. A mixture of surface groups, including −F, −Cl, −O, and –OH, can be introduced during the acidic etching process. The stoichiometry of the surface terminations is influenced by the etching environment. Taking $Ti_3C_2T_x$ as an example, the chemical formula is $Ti_3C_2(OH)_{0.06}F_{0.25}O_{0.84}$ after LiF-HCl etching, while it becomes $Ti_3C_2(OH)_{0.12}F_{0.8}O_{0.52}$ after HF etching [53]. Additionally, F-rich and OH-free terminated $Ti_3C_2T_x$ MXene can be synthesized using anhydrous solvents [54].

Many efforts have been made to develop fluorine-free methods or it can be referred to “green synthesis method”, driven by the concerns regarding environmental issues associated with fluorine compounds [55]. These methods include molten salt etching [56], alkali treatment hydrothermal etching [57], electrochemical etching [58], and photo-Fenton approach [59]. The molten salt method involves immersing

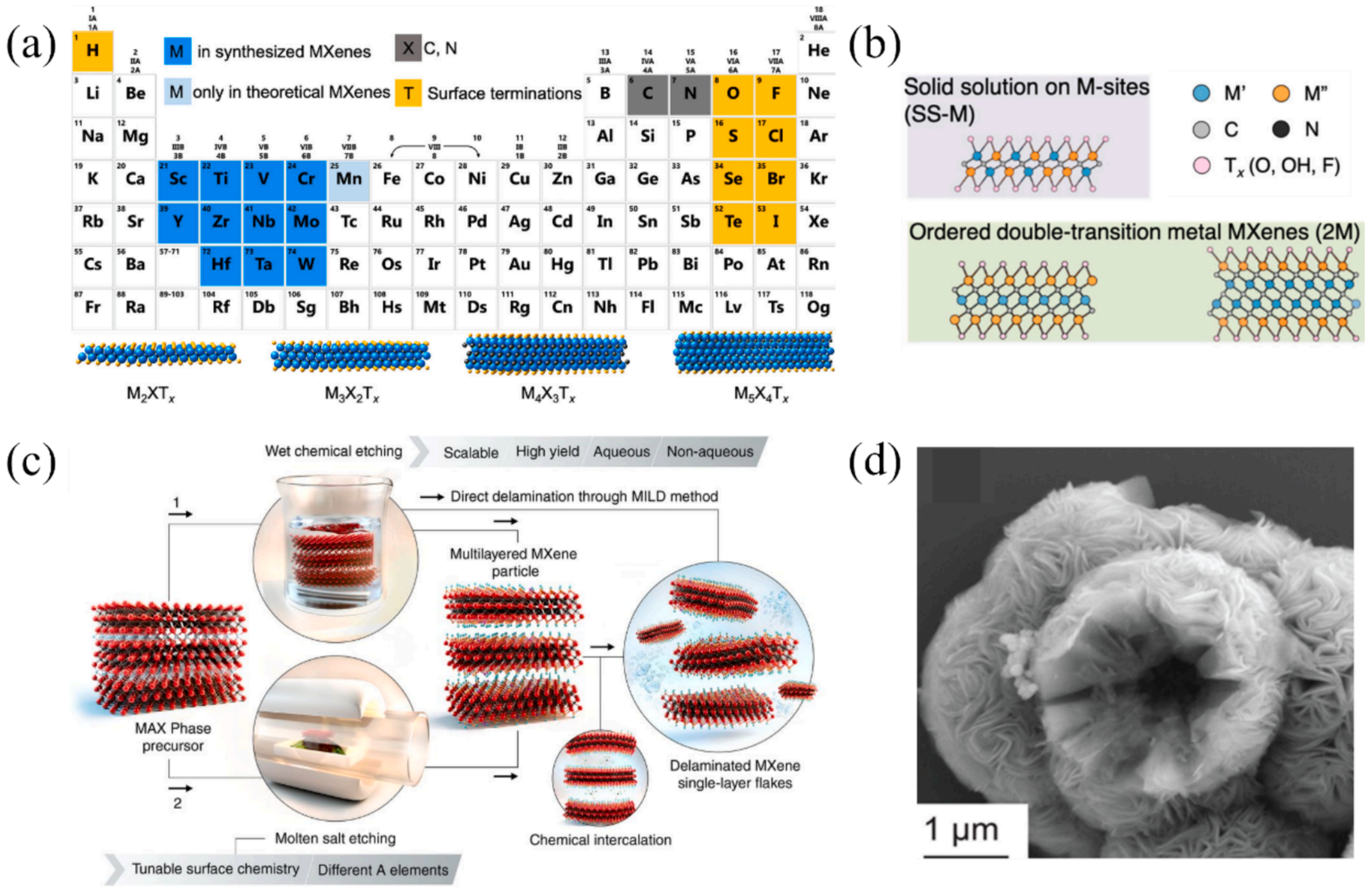

Fig. 3. (a) Periodic table showing possible elemental compositions of MXene. The chemical formula of MXene can be represented as $M_{n+1}X_nT_x$: while blue represents the transition metals M that have been synthesized successfully in MXene, light blue represents that only exist in theoretical simulations; gray represents X (X = C/N); and yellow represents surface groups T_x. Reproduced with permission: Copyright 2021, American Chemical Society [34]. (b) Atomic structures for solid solution on M−sites (SS-M) and ordered double-transition-metal MXenes (2 M) Reproduced with permission: Copyright 2020, American Chemical Society [45]. (c) Schematic illustration displaying the synthesis of MXene through etching the A layers from MAX phases. Reproduced with permission: Copyright 2020, American Association for the Advancement of Science [49]. (d) Scanning electron microscopy (SEM) image of a CVD-Ti_2CCl_2 microsphere. Reproduced with permission: Copyright 2023, American Association for the Advancement of Science [66]. (For interpretation of the references to color in this figure legend, the reader is referred to the web version of this article.)

the MAX precursors in Lewis acidic molten salt at elevated temperatures, where the A layers are selectively removed due to their weak bonding energy to early transition metal atoms (Fig. 3c). Simultaneously, molten salt ions undergo reduction reactions (e.g., Cu^{2+} is reduced to metallic Cu), leading to the formation of MXenes with selective surface groups [56]. The development of molten salt methods facilitates the synthesis of MXenes with stoichiometric single terminations, including halide-terminated ($Ti_3C_2Cl_2$, $Ti_3C_2Br_2$, and $Ti_3C_2I_2$) and chalcogenide-terminated (Nb_2CO_2, Nb_2CS_2, Nb_2CSe_2, and Nb_2CTe_2) MXenes [56,60,61]. Recently, Huang et al. reported another Se-terminated MXene Nb_2CSe_2 prepared through a novel one-step “vapor-active” method [62].

Various bottom-up methods have been investigated in the pursuit of large-scale and controllable production of MXene, including chemical vapor deposition (CVD) [63], ion sputtering [64], and wet chemical amalgamation [65]. These methods tend to offer higher controllability, uniformity, and scalability. For instance, large-area and uniform 2D ultra-thin α-Mo_2C crystals can be synthesized using CH_4 as the carbon source and copper foil placed on molybdenum foil as the catalyst for CVD. The size, thickness, and morphology of Mo_2C crystals can all be tuned by adjusting temperature and the growth time [63]. Additionally, bottom-up methods also offer possibilities for the morphology control of MXene. Ti_2CCl_2 was grown on the Ti surface at 950 °C by CVD using a gas mixture of Ar/$TiCl_4$/CH_4. The resulting structure exhibited a distinctive “flower-like” vesicle morphology (Fig. 3d), which is formed through step-by-step buckling and releasing of MXene [66].

Different MXene synthesis methods exhibit distinct advantages and limitations, with the choice of method being critical for Li-S batteries. HF etching and HCl/LiF etching are straightforward and widely used techniques for producing monolayer or few-layer MXenes. However, it poses safety risks due to the use of hydrofluoric acid and results in MXenes with a high concentration of −F functional groups, which limits their polysulfide adsorption capacity. Molten salt etching offers precise control over surface groups, enhancing the electrical conductivity and polysulfide interaction of MXenes. Such process requires high-temperature processing, leading to significant energy consumption, and often results in large, bulk products with relatively low surface area. Besides, few layers MXene prepared by molten salt method also requires special delamination process, which results in low yield [67]. Electrochemical etching is a safer alternative that allows for surface chemistry control, but it is slower and yields lower product quantities. CVD method provides excellent control over surface chemistry and is scalable for mass production, but it remains underexplored in the context of MXene synthesis, requiring high temperatures and vacuum conditions, which complicates its application. For Li-S battery applications, methods that maximize surface area, electrical conductivity, and polysulfide adsorption are preferred. Thus, molten salt etching and CVD show the most promise but require further optimization and research to improve product purity and scalability.

3. MXene properties and internal regulation for high-performance Li-S batteries

The variety of MXene compositions and synthesis methods enable researchers to optimize the properties of MXenes to improve the performance of Li-S batteries. In this section, we first summarize the properties of pristine MXene and discuss its functions in Li-S batteries, including its roles as sulfur host materials or as the coating materials for separators. Then, we review various internal modification strategies that have been applied to MXenes to boost its properties for high performance Li-S batteries.

3.1. MXene properties and its application in Li-S batteries

Many MXenes possess high electronic conductivity, which is a key advantage for their application in Li-S batteries [68]. The electronic conductivity of $Ti_3C_2T_x$ MXene achieved 20,000 S cm^{-1} when the Ti_3AlC_2 MAX phase with excess aluminum was used as the precursors [69]. Nitride MXenes are anticipated to exhibit higher electrical conductivity than carbide MXenes because nitrogen contributes more electrons than carbon. However, nitride MXenes are unstable in HF solution, and the preparation of nitride MXene is more complicated than that of carbide MXene [70]. Besides, the creation of vacancies in the metal layer of MXene has an impact on electronic conductivity. For example, $Mo_{1.33}C$ exhibited higher electrical conductivity and better electrochemical performance than Mo_2C [44]. For multi-metal MXenes, the metal atoms on the surface play a more significant role in electrical conductivity than inner metals [71], and preparing high-entropy MXenes may also enhance electrical conductivity [72].

Benefiting from their high conductivity, MXenes have been directly employed as sulfur host to improve the cathode conductivity. The first research that applied MXenes in Li-S batteries was published in 2015 by Nazar et al. [36]. They utilized delaminated Ti_2C (d-Ti_2C) combined with 70 wt% sulfur as a composite cathode. X-ray photoelectron spectroscopy (XPS) analysis indicated that the Ti-OH fraction in the 70%S/d-Ti_2C cathode decreased compared to pristine Ti_2C. The decrease in Ti-OH groups is attributed to the replacement of –OH by sulfur (or S^{2-}) during the cathode preparation process, resulting in the formation of Ti-S bonds. These formed Ti-S bonds serve as active centers to facilitate the conversion from S_8 to Li_2S (Fig. 4a). Despite d-Ti_2C having neither a high specific surface area nor a well-ordered pore structure, the 70%S/d-Ti_2C cathode achieved excellent reversible capacity of 1200 mAh g^{-1} at 0.2C and long-term cycling stability of 400 cycles at 0.5C. Later, Zhao fabricated layered Ti_3C_2 MXene (L-Ti_3C_2) with an accordion-like morphology and utilized it as a sulfur host material [73]. The individually separated MXene layers provided space for sulfur loading, allowing for 57.6 wt% sulfur to be evenly distributed between the MXene layers by annealing at 155 °C. The rapid electron transport along the

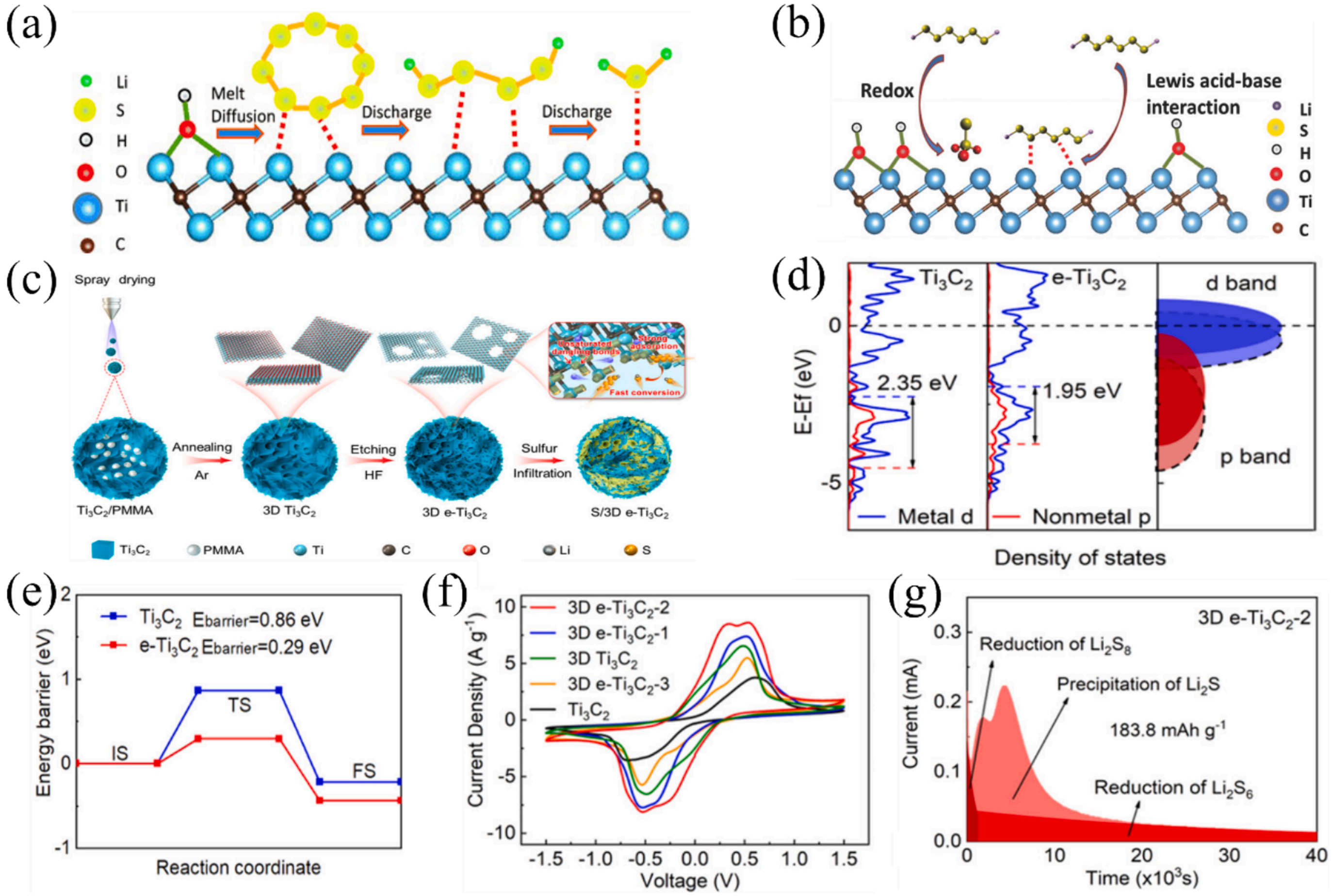

Fig. 4. (a) Schematic illustration showing the replacement of the Ti-OH bond on the MXene surface with a S-Ti-C bond by heat treatment or by contact with polysulfides. Reproduced with permission: Copyright 2015, Wiley [36]. (b) Schematic demonstrating the two-step interaction between a hydroxyl-decorated MXene phase and polysulfides. Reproduced with permission: Copyright 2016, Wiley [74]. (c) Schematic illustration of the fabrication of S/3D e-Ti_3C_2 microspheres. (d) Density of states analysis of Ti and C in Ti_3C_2 and e-Ti_3C_2, respectively. (e) Energy profiles of Li_2S decomposition on Ti_3C_2 and e-Ti_3C_2 surfaces. (f) CV curves of symmetric cells prepared with various types of Ti_3C_2 and e-Ti_3C_2 at 10 mV s^{-1}. (g) Li_2S electrochemical deposition profiles of e-Ti_3C_2-2. Reproduced with permission: Copyright 2021, American Chemical Society [75].

MXene flakes can facilitate the electrochemical reactions of the intercalated sulfur. Moreover, the accordion-like structure can adapt the significant volume expansion during Li-S battery discharging. As a result, the S/L-Ti_3C_2 composite cathode delivered a high initial discharge capacity of 1291 mAh g^{-1} and a high retention of 75.1% after 100 cycles. In 2017, Nazar's group explored the application of Ti_3C_2 and Ti_3CN MXene in Li-S battery for their surface reactivity using XPS and DFT calculations [74]. They revealed that the adsorption of MXene to LiPS is based on a Lewis acid base interaction, while MXene acts as a Lewis acid by accepting electron pairs from the Lewis basic polysulfides, facilitating strong adsorption. Specifically, the surface terminations of –OH are consumed by interactions with polysulfides via thiosulfate formation, and the uncoordinated Ti on the surface bonds with sulfur to form Ti-S bonds, resulting in strong adsorption of polysulfides. This study provided a unique explanation of how MXene can trap polysulfides and improve cycling stability (Fig. 4b). This work achieved a long lifespan of over 1200 cycles with an ultralow decay rate of 0.043% per cycle at 1.5 mg cm^{-2} of sulfur loading.

Since then, the utilization of MXene in Li-S batteries has experienced rapid expansion, and the catalytic ability of MXene in boosting the conversion of LiPS has gradually received more attention. Chen et al. prepared hierarchically porous MXene microspheres (e-Ti_3C_2) with tunable edges as a multifunctional catalyst for Li-S batteries (Fig. 4c) [75]. During synthesis, HF was employed to remove the in-situ formed Ti-O bonds, creating numerous unsaturated Ti sites with abundant pores in the framework. Simulation results suggested that the edge of Ti_3C_2 contained abundant unsaturated Ti sites, which could act as multifunctional active sites to chemically anchor LiPS, lower the Li^+ transport barriers, and electrocatalytically accelerate LiPS conversion and Li_2S decomposition. As shown in Fig. 4d, the unsaturated Ti reduces the energy gap between Ti 3d and C 2p in e-Ti_3C_2, thereby weakening the strength of S-S bonds and facilitating LiPS decomposition. Moreover, the Li_2S decomposition energy on the surface of e-Ti_3C_2 (0.29 eV) is significantly smaller than that on the Ti_3C_2 surface (0.86 eV), indicating that e-Ti_3C_2 can promote the transformation of solid-phase Li_2S to liquid-phase polysulfide (Fig. 4e).

In addition to the theoretical perspective mentioned above, the electrocatalytic ability was further confirmed by experimental studies such as symmetric cyclic voltammetry (CV) and Li_2S nucleation test [76,77]. A symmetric CV test is conducted with the same electrode material placed on both sides of a separator in Li_2S_6-containing electrolytes. The peaks shown on the CV curves reflect the redox activity of Li_2S_6 on the electrode. Fig. 4f shows the CV curves of pristine Ti_3C_2, 3D Ti_3C_2, and e-Ti_3C_2 dried at different temperatures. The 3D e-Ti_3C_2-2 sample, corresponding to the e-Ti_3C_2 dried at 60 °C, exhibited the highest current density and lowest redox potentials among all samples. It demonstrated the most rapid charge transfer and improved redox reaction kinetics of the sample for sulfur species conversion. A Li_2S nucleation test can be further performed to evaluate the energy barrier for converting liquid LiPS to solid Li_2S. In this test, the samples are utilized as cathodes in the cells with lithium metal as anodes and Li_2S_8-containing solvents as electrolytes. As shown in Fig. 4g, the cells were first discharged from open circuit potential to 2.06 V galvanostatically at 0.112 mA, and then discharged from 2.05 V potentiostatically until the current fell below 0.01 mA. Based on the Li_2S deposition profiles, the Li_2S precipitation capacity on 3D e-Ti_3C_2-2 was calculated to be 183.8 mAh g^{-1} [76]. The sample exhibited high capacity and short response time for Li_2S nucleation, indicating a low Li_2S nucleation barrier. With all these merits, the S/e-Ti_3C_2 cathode delivered a high capacity of 803.4 mAh g^{-1} after 500 cycles and a high areal capacity of 5.6 mAh cm^{-2} with a high sulfur loading (6.1 mg cm^{-2}) and lean electrolyte/sulfur ratio (5.2 μL mg^{-1}) [75].

Recently, several high-entropy compounds have achieved significant success for improving the performance of Li-S batteries [78–80]. Yang et al. reported the successful synthesis of high-entropy MXene ($(Ti_{1/3}V_{1/3}Zr_{1/6}Nb_{1/6}Ta_{1/6})_2C_xN_{1-x}$ (HE CN-MXene) with all metal elements randomly and uniformly dispersed in the metal layers [48]. The HE CN-MXene exhibited strong mechanical properties attributed to the stable integration of various-sized metal atoms. High electrical conductivity was also observed in the HE CN-MXene due to the redistribution of electrons [78]. Furthermore, the metal layers with five different metals offered abundant active sites to capture and convert LiPS. Benefiting from these advantages, Li-S batteries with HE CN-MXene showed high-rate performance of 702 mAh g^{-1} at 4C and stable cycling capability (738 mAh g^{-1} under 1C after 300 cycles). Another high entropy MXene, $TiVNbMoC_3$, was proved to present an electronic enrichment state near the 0 eV Fermi level based on density of states (DOS) simulations [72]. $TiVNbMoC_3$ exhibited several advantageous properties compared with transition metal carbides and Ti_4C_3 MXene, including higher binding energy to LiPS, lower Li-ion transport barrier, and lower Li_2S decomposition energy barrier. As a result, the cell with $TiVNbMoC_3$ achieved outstanding long-cycling performance, with a decay rate as low as 0.026% per cycle at 1C and 0.031% per cycle at 2C for 1200 cycles [72].

MXene holds great potential for free-standing and binder-free electrodes due to its 2D structure and excellent mechanical properties, which lays the foundation for its possible application in flexible devices and wearable electronics [81,82]. 2D Ti_2C MXene can withstand large strains of 9.5% under biaxial tensions. It can also endure strains of 18% and 17% under uniaxial tensions along the x-axis and y-axis, respectively [83]. Moreover, surface groups have a significant impact on MXene's mechanical properties. For instance, by tuning the surface groups to Ti_2CO_2, the tensile strength can be increased to 20% (biaxial), 28% (uniaxial along the x-axis), and 26.5% (uniaxial along the y-axis), outperforming graphene (15% biaxial). A strong free-standing MXene paper was reported to withstand stresses of approximately 41.3 MPa with around 0.8% elastic strain [84]. Fig. 5a shows a MXene paper with amorphous sulfur uniformly distributed between MXene layers, prepared by vapor deposition. This freestanding $Ti_3C_2T_x$/S paper showed good mechanical flexibility (Fig. 5b). The fracture strain decreased to 1.8% for the freestanding MXene/S paper compared to 2.2% for the MXene paper (Fig. 5c). It's worth mentioning that MXene/S could be bent convexly or concavely while still maintaining flexibility without any damage. Interestingly, MXene/S paper exhibited an even higher fracture stress (79.6 MPa) than pure MXene paper (45.8 MPa). However, due to the tightly compacted structure, the sulfur loading was limited to 30 wt%. To improve the sulfur loading, Alshareef et al. fabricated a freestanding membrane by encapsulating sulfur in $Ti_3C_2T_x$ MXene with different flake sizes (Fig. 5d) [85]. Firstly, crumbled $Ti_3C_2T_x$ (C-$Ti_3C_2T_x$) with a size distribution of 20–200 nm was utilized to wrap sulfur particles. Subsequently, $Ti_3C_2T_x$ with a large size of 1–3 μm (L-$Ti_3C_2T_x$) was employed as a conductive scaffold to improve the mechanical strength of the membrane. Consequently, a 3D hierarchical structure was prepared, featuring numerous active sites to chemically immobilize LiPS and abundant space to load sulfur while accommodating volume expansion. This freestanding cathode, with 69.6 wt% sulfur loading, could achieve an excellent areal capacity of 2.1 mAh g^{-1} and energy density of 652 Wh kg^{-1} based on the whole weight of cathode at 3C. It also delivered a notable volumetric capacity of 2.7 Ah cm^{-3} after 200 cycles with the sulfur loading of 4.0 mg cm^{-2}. Furthermore, as MXene flakes are negatively charged, they could be effectively dispersed in water, forming MXene-based inks suitable for various printing technologies [86,87]. As shown in Fig. 5e, f, the concentrated and viscous S@$Ti_3C_2T_x$ ink can be cast on Al foils using doctor blade deposition. The resulting freestanding S@$Ti_3C_2T_x$ film could deliver 1170 mAh g^{-1} at 2C and maintain 1170 mAh g^{-1} after 175 cycles [57].

Separator modification is another effective method to address the shuttle effect and accelerate sulfur species conversion [88]. Due to the restacking issue of 2D MXenes, modifying the separator with MXene can block ion transfer pathways, thereby limiting charge transfer at high-rate current density. Moreover, the restacking also buries many active surface sites within the densely packed MXene layers, weakening the interaction between MXene and LiPS [89]. Therefore, rational

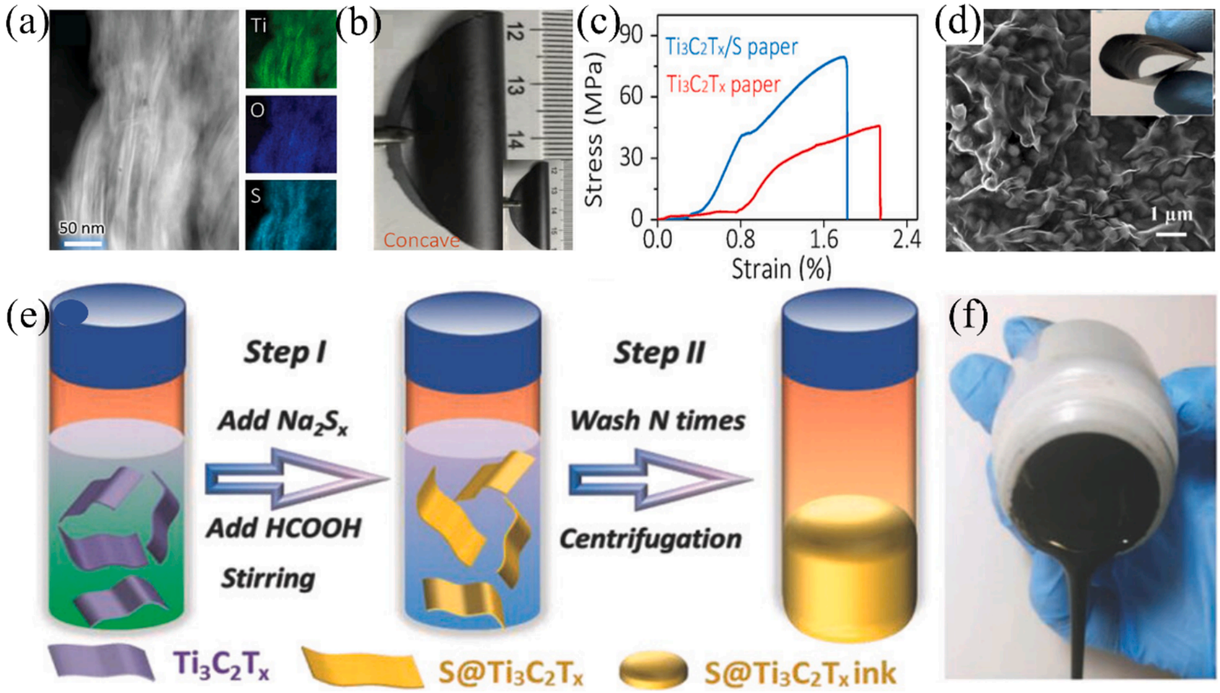

Fig. 5. (a) Cross-section SEM image of $Ti_3C_2T_x$/S paper and corresponding energy dispersive X-ray spectroscopy (EDX) elemental mapping of Ti, O, and S elements. (b) Photographs of freestanding $Ti_3C_2T_x$/S paper when bending, showing good mechanical flexibility. (c) Stress–strain curve of the $Ti_3C_2T_x$/S paper and pure $Ti_3C_2T_x$ paper. Reproduced with permission: Copyright 2019, Wiley [84]. (d) SEM image of S@PCL membrane, inset is the photograph of the free-standing, flexible S@PCL cathode (S mass loading: 4.0 mg cm^{-2}). Reproduced with permission: Copyright 2021, Elsevier [85]. (e) Schematic explaining the preparation, and (f) Optical image of S@$Ti_3C_2T_x$ ink, showing its viscous nature. Reproduced with permission: Copyright 2018, Wiley [57].

morphology modification is crucial to maximize the utilization of MXene's active surface and optimize separator design. As shown in Fig. 6a, $Ti_3C_2T_x$ MXene membranes with controllable in-plane pores were prepared via an "oxidation-etching" method [90]. Cu^{2+} catalysts facilitate the partial oxidation of $Ti_3C_2T_x$ flakes to TiO_2, and the concentration of Cu^{2+} determines the porosity of the in-plane pores. MXene membranes with abundant pores (Fig. 6b) enable lithium ions to pass freely while blocking the shuttling of LiPS, thereby enabling high sulfur utilization even at high current densities. Consequently, Li-S batteries with optimized MXene membranes exhibited significantly

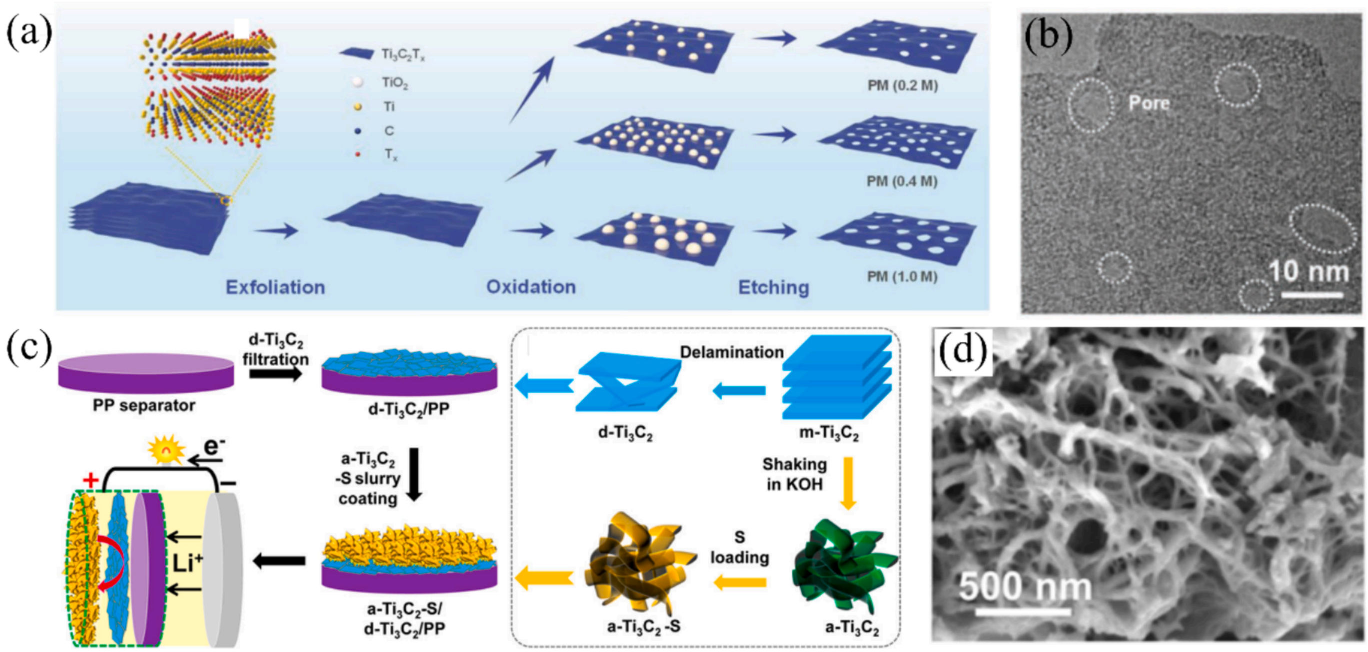

Fig. 6. (a) Schematic illustration of the synthesis of porous MXene (PM). (b) SEM image of porous $Ti_3C_2T_x$ MXene. Reproduced with permission: Copyright 2021, Wiley [90]. (c) Left: schematic illustration of the fabrication of the flexible and integrated a-Ti_3C_2-S/d-Ti_3C_2/PP electrode for Li-S batteries. Right: schematic illustration of the preparation of d-Ti_3C_2 nanosheets and a-Ti_3C_2-S hybrid. (d) SEM image of a-Ti_3C_2-S hybrid. Reproduced with permission: Copyright 2018, American Chemical Society [92].

improved rate capability, delivering 677.6 mAh g^{-1} at 2C. Cutting 2D MXene into 0D quantum dots before coating it on the separator is another method to provide open ion transport channels [91]. Due to its small size, 0D MXene can further prevent MXene restacking and offer more active sites to capture and catalyze the dissolved LiPS. In another example, MXene is employed both as the modifier for the separator and as the host material for sulfur [92]. As illustrated in Fig. 6c, delaminated MXene (d-Ti_3C_2) is applied to cover the separator, thereby preventing the shuttle effect of LiPS. Simultaneously, the d-Ti_3C_2 undergoes conversion into a MXene nanoribbon framework (a-Ti_3C_2) through KOH treatment, serving as the host material for sulfur (Fig. 6d). The nanoribbon framework features open and interconnected macropores with a large surface area, ensuring high sulfur loading and rapid ion transport for efficient charging/discharging processes. This MXene-based Li-S battery can operate without current collector and demonstrates a high reversible capacity of 1062 mAh g^{-1} at 0.2C.

3.2. MXene surface group engineering

The surface chemistry of MXene is one of the main factors influencing the performance of MXene-based Li-S batteries. The electrical conductivity, which is essential for electron transport in the sulfur electrode, is affected by the type of present surface groups. Nb_2CCl_2 exhibits higher conductivity than conventional Nb_2CT_x with mixed –O, –OH, and –F terminal groups [61], and Nb_2CSe_2 even surpasses that of the conventional Nb_2CT_x MXene by over 2000 times [62]. More importantly, the adsorptive and catalytic effects differ among different surface groups, which allows the researchers to optimize the surface groups to enhance its performance in Li-S electrochemistry.

Computational simulations have been employed to elucidate the roles of various surface groups in the adsorption and conversion kinetics of LiPS. DFT simulation revealed that both –F and –O on the Ti_2C MXene can mitigate the shuttle effect, but the suppression mechanisms are different. For –F groups, polysulfides tend to be anchored on Ti_2CF_2 rather than dissolve in the electrolyte. This is due to the higher binding energy of polysulfides on Ti_2CF_2 compared to that of dimethoxyethane (DME) and1,3-dioxolane (DOL). Meanwhile, the –O group on the Ti_2CO_2 can facilitate the transformation of long-chain LiPS (Li_2S_8, Li_2S_7, and Li_2S_6) into insoluble elemental sulfur to address the shuttle effect. Additionally, the conductivity of Ti_2CO_2 transfers from semiconductor to metallic features after anchoring LiPS, thereby supporting the redox reaction of LiPS intermediates [32]. Another first principle study revealed that Ti_2CS_2 exhibits a higher binding energy toward LiPS compared to Ti_2CF_2 and Ti_2CO_2 MXenes (Fig. 7a). Besides, Ti_2CS_2 can also facilitate electrochemical activity due to its metallic features [93]. Wei et al. proposed an universal atomic surface group modification approach to enhance the adsorption and electrocatalytic effect of $Ti_3C_2T_2$ MXene for Li-S batteries. They investigated $Ti_3C_2T_2$ with five different surface terminations (T = N, O, F, S, and Cl), all of which exhibited metallic conductivity. Among them, $Ti_3C_2S_2$ and $Ti_3C_2O_2$ can promote the conversion from LiPS to Li_2S due to their lower decomposition barrier of Li_2S_6. $Ti_3C_2S_2$ and $Ti_3C_2O_2$ also exhibit a lower Li^+ diffusion barrier, which may enhance the high-rate performance. Meanwhile, Ti_3C_2 with single –S/-N/-O surface group offer moderate adsorption energies to LiPS, which can suppress LiPS dissolution and shuttling. Similarly, Wang et al. calculated the LiPS adsorption strength of various surface groups on $Ti_3C_2T_x$. They observed that adsorption strength increases in the following order: Cl, F, N, O, S [94]. Among these surface groups, –O and –S terminated Ti_3C_2 exhibited superior electrocatalytic properties for Li_2S decomposition. Interestingly, they also found that vacancies can significantly impact the adsorption ability. Although the adsorption strength of $Ti_3C_2Cl_2$ to Li_2S_8 is only 0.7–1.1 eV, it can be increased to 2.5–3.5 eV by creating 1/16Cl deficiencies [94]. For vanadium carbide MXenes, bare V_2C without terminations showed extremely high adsorption energies, ranging from −6.42 eV for Li_2S to −19.52 eV for S_8. Although the strong adsorption energies effectively

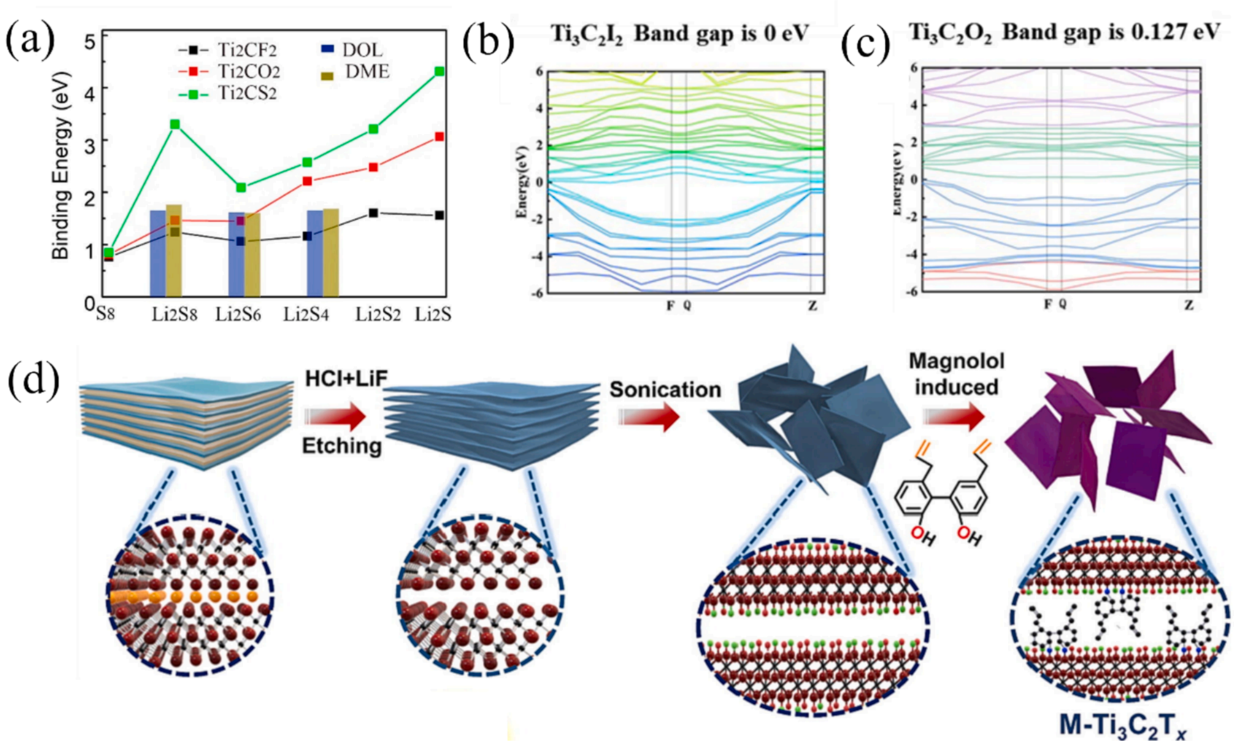

Fig. 7. (a) Comparison of the binding energies of polysulfides with Ti_2CS_2, Ti_2CO_2, Ti_2CF_2, and electrolyte solvent molecules (DME and DOL). Reproduced with permission: Copyright 2018, Elsevier [93] (b) Band Structures of $Ti_3C_2I_2$. (c) Band Structures of $Ti_3C_2O_2$. Reproduced with permission: Copyright 2022, American Chemical Society [99] (d) Schematic illustration of the synthesis of Magnolol-modified $Ti_3C_2T_x$ (M−$Ti_3C_2T_x$). Reproduced with permission: Copyright 2022, Elsevier [103].

immobilize Li_2S_n, excessive adsorption can lead to the decomposition of Li_2S_n, preventing their further reduction. Meanwhile, V_2C with sulfur terminations (V_2CS_2) demonstrated moderate adsorption, which provides sufficient capability to address the shuttle effect while preventing the decomposition of Li_2S_n and facilitating Li_2S_n conversion. Besides, V_2CS_2 can maintain metallic properties after adsorbing LiPS, thereby enhancing electrochemical activity during battery cycling [95].

Experimentally, several approaches have been employed to introduce different surface groups aimed at enhancing LiPS adsorption and conversion. As discussed in section 2, the etchant composition and etching environment influence the composition of surface groups of MXene. MXenes prepared by HF etching contain more –OH and −F groups [26]. They primarily adsorb polysulfides via Lewis acid-base interaction. The –OH groups would react with LiPS to produce thiosulfate, followed by forming Ti-S bonds to absorb polysulfides [74,96]. The surface groups of MXenes can also be tuned by post-treatment. Dang et al. fabricated Nb_2C MXene with a uniformly O-terminated surface through heat treatment [97]. They demonstrated the superior catalytic activity of Nb_2CO_2 compared to other surface groups and bare surfaces. Another work reported the oxygen-functionalized Ti_3C_2 MXene (O-Ti_3C_2) prepared via pyrolysis [98]. The oxygen groups on the O-Ti_3C_2 can regulate the D-band center of Ti atoms, bringing it closer to the Fermi level and thereby enhancing electrocatalytic activity. The O-Ti_3C_2 was utilized on both the anode and cathode sides: it improved the electrode affinity towards LiPS and the reaction kinetics of LiPS conversion on the cathode side; Meanwhile, it enabled the formation of a dendrite-free Li anode by promoting high-flux Li diffusion. A practical and flexible Li-S pouch cell employing this design achieved an impressive areal capacity of 5.2 mAh cm^{-2} over 30 cycles with sulfur loading up to 6.7 mg cm^{-2} and lean electrolytes of electrolyte-to-sulfur ratio of 6.0 mL g^{-1} [98]. However, the preparation of O-terminated MXenes essentially involves oxidizing the surface of MXenes. Therefore, it is crucial to precisely control the degree of oxidation during post-treatment to avoid the formation of TiO_2, as it would significantly reduce the conductivity of MXene. In contrast, an I-terminated Ti_3C_2 MXene (I-MXene) was produced by annealing a mixture of potassium iodide and the few-layer MXene under an inert gas environment at high temperature [99]. The I-MXene effectively immobilizes LiPS through Ti-S bonds and boosts the reaction kinetics of LiPS conversion. Notably, the band gap of $Ti_3C_2I_2$ is near 0 eV (Fig. 7b), which is much lower than that of $Ti_3C_2O_2$ (Fig. 7c), indicating the high electronic conductivity of I-MXene. Leveraging these advantages, the cell employing I-MXene exhibited a notable initial discharge capacity of 1308 mAh g^{-1} and retained 761 mAh g^{-1} after 100 cycles at 0.2C.

In addition to single-atom surface groups, larger groups can also be utilized to graft on MXene surface. Ammonia and Ti_3C_2 MXene were used to synthesize Ti_3C_2-NH_2 nanosheets through a straightforward sealed thermal method. The presence of –NH_2 effectively enhanced the mechanical strength of MXene [100,101]. Amide- and imino-terminated MXenes can be synthesized by reacting halogen-terminated MXenes with deprotonated organic amines [102]. As shown in Fig. 7d, The reaction between magnolol and $Ti_3C_2T_x$ in N,N-Dimethylformamide (DMF) can be represented by the following equation: $Ti_3C_2O_x(OH)_yF_z + nROH = Ti_3C_2O_x(OH)_y(OR)_{z\text{-}n} + nHF$. When the magnolol-modified $Ti_3C_2T_x$ ($M-Ti_3C_2T_x$) was employed as a sulfur host material, the surface chemistry not only facilitated the formation of C-S bonds, but also resulted in the uniform dispersion of sulfur atoms through inverse vulcanization owing to the symmetrical bisphenol and diallyl groups of magnolol. The as-prepared S/$M-Ti_3C_2T_x$ electrode delivered a high reversible capacity of 7.68 mAh cm^{-2} at a high sulfur loading of 7.2 mg cm^{-2} and a low decay rate of 0.07% [103].

3.3. Heteroatom doping

Unlike surface engineering, which only modifies the outermost layer, atomic-scale doping can replace atoms within the lattice of MXene. The reconstitution of the electronic state for MXene, modified by heteroatom doping, creates a more uniform distribution across the MXene surface, thus improving the conductivity [31], adsorption, and catalytic conversion of LiPS [104]. Heteroatom doping is categorized as anion doping, cation doping, and co-doping, depending on the different dopant atoms.

3.3.1. Anion-doped MXene

Nitrogen doping on graphene is widely studied and is considered beneficial for charge transfer and LiPS immobilization for Li-S batteries [105]. Recently, there have also been some reports about nitrogen-doping MXene, inheriting the same idea. Unlike graphene, where nitrogen atoms can only substitute carbon atoms, there are three possible nitrogen-doping sites on carbide MXene: surface adsorption on MXene; substitution of other terminations to form −N surface groups; lattice substitution of carbon to form Ti-N bonds. [94,106,107]. The lattice substitution of carbon atoms tunes the Fermi level to a lower state as nitrogen contains more electrons, thus enhancing the electrical conductivity [31]. A DFT study demonstrated that replacing some carbon atoms with nitrogen in Ti_2CO_2 can increase the conductivity from semiconductive to metallic conductive [108].

The interaction between MXene and LiPS also changes after nitrogen doping, directly impacting Li-S batteries. The binding energy between nitrogen-doped Ti_3C_2 (N-Ti_3C_2) and Li_2S_4 (14.27 eV) is much higher than that of Ti_3C_2 (10.59 eV) as shown in Fig. 8a [109]. The strong chemical adsorption of N-Ti_3C_2 significantly improves the confinement ability towards LiPS. It should be noted that this work utilizes MXene without functional groups to simulate the Lewis acid-based chemical bonds, as there is no binding energy shifts for −F terminations on MXene surface. The effect of surface groups was carefully considered for other cases since the adsorption effect significantly differs among different surface groups [94]. Song et al. utilized melamine formaldehyde (MF) spheres as a sacrificial template along with a nitrogen source to prepare porous N-doped Ti_3C_2 MXene (P-NTC), demonstrating enhanced electrocatalytic ability for Li-S chemistry [107]. As depicted in Fig. 8b, after removing the MF templates by annealing in Ar gas at 500 °C, nitrogen dopants were uniformly distributed on MXene. Ti-N bonds were detected by XPS, confirming successful doping. The N-doped surface increased the electron density and exhibited larger adsorption energy to Li atoms, enhanced the interfacial interaction with Li_2S clusters, and facilitated nucleation of Li_2S from LiPS. Regarding the reverse oxidation process, the decomposition energy barrier for Li_2S on the N-doped MXene (0.14 eV) is also lower than on pure MXene (0.19 eV), indicating a superior bidirectional electrocatalytic effect towards the redox reaction of Li-S chemistry. As a result, the N-doped MXene contributed to a long-life Li-S battery with a low capacity decay rate of 0.033% per cycle at 2C over 1200 cycles. In another study, MF spheres were again utilized as the sacrificial template and nitrogen source to prepare a freestanding N-Ti_3C_2@S/graphene cathode for Li-S battery via a straightforward slurry-free method [110]. The as-prepared electrode provided a high initial capacity of 1342.6 mAh g^{-1} at 0.1C with a low capacity decay rate of 0.067% per cycle. HCl-treated melamine can also be utilized as the nitrogen source to prepare the N-doped MXene. For example, 3D N-Ti_3C_2 MXene@CNT microspheres were prepared via spray drying and subsequent pyrolysis progress [111]. The resulting sample contained CNTs in its 3D network, which improved porosity and conductivity. Meanwhile, the N-doped MXene exhibited enhanced adsorption to LiPS species, which aided in trapping the LiPS in the porous microspheres. When applied as a sulfur host material, N-Ti_3C_2 MXene@CNT showed superior cycling stability at high current density (647 mAh g^{-1} after 650 cycles at 4C) and high sulfur loading (3 and 6 mg cm^{-2}).

N-Ti_3C_2 MXene was also utilized to adjust the Li^+ stripping/plating performance, which is important for the anode design of Li-S batteries [112]. As shown in Fig. 8c, N-$Ti_3C_2T_x$ was applied to both cathode and anode of a Li-S battery. On the anode side, the N-$Ti_3C_2T_x$ was 3D printed on the top of Li foil, which reduced overpotentials for the Li^+ stripping/

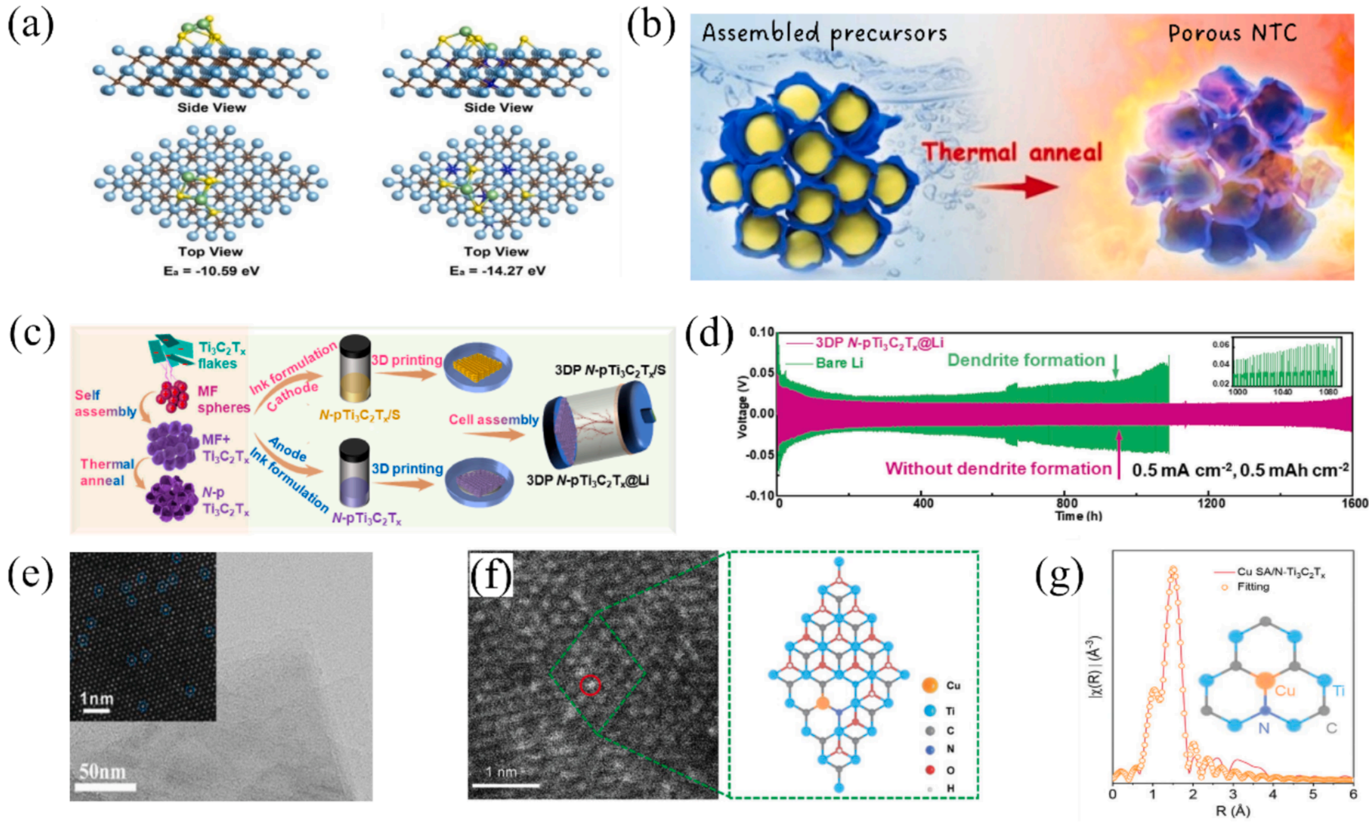

Fig. 8. (a) The optimized structures and adsorption energies of Li_2S_4 on the surface of Ti_3C_2 (left) and N-Ti_3C_2 (right). Reproduced with permission: Copyright 2019, Elsevier [109]. (b) Schematic illustration of the melamine–formaldehyde (MF) templating synthesis of P-NTC: the blue sheets represent MXene, and the yellow spheres represent MF spheres. Reproduced with permission: Copyright 2020, Elsevier [107]. (c) Schematic diagram of the preparation of Li-S battery dual electrodes utilizing of 3DP framework of N-p$Ti_3C_2T_x$. (d) Voltage-time graph of Li symmetric cells in the presence/absence of 3DP N-p$Ti_3C_2T_x$ interlayer at 0.5 mA cm^{-2} with a Li stripping/plating capacity of 0.5 mAh cm^{-2}. Reproduced with permission: Copyright 2021, Elsevier [112]. (e) The aberration-corrected high-angle annular dark-field scanning transmission electron microscopy (HAADF-STEM) image of SA-Zn-MXene, showing the presence of many single zinc atoms as marked with blue circles. Reproduced with permission: Copyright 2022, Wiley [121]. (f) Magnified atomic-resolution HAADF-STEM image and the illustration of the structure model. (g) Fourier-transformed extended X-ray absorption fine structure (FT-EXAFS) fitting curves of Cu SA/N-$Ti_3C_2T_x$. The inset shows the local atomic structure of Cu (Ti, cyan; C, gray; N, blue; Cu, orange). Reproduced with permission: Copyright 2023, Wiley [125]. (For interpretation of the references to color in this figure legend, the reader is referred to the web version of this article.)

plating. The overpotential remained low after 1600 h (~15 mV), which was much lower than that of pure Li (Fig. 8d).

In addition to the extensively studied N-Ti_3C_2 MXene as sulfur hosts, N-Mo_xC nanosheets were successfully synthesized and utilized as separator modifiers [113]. The N-Mo_xC contained multi-dimensional networks, which improved both physical blocking and chemical adsorption to LiPS while providing many active sites to catalyze Li-S reversible reactions. The Li-S battery with N-Mo_xC modified separator exhibited a remarkable capacity of 1067 mA h g^{-1} at 0.5C, and an enhanced cycling performance of 610 mA h g^{-1} after 500 cycles at 1C with a capacity decay rate of 0.09% per cycle.

It is worth mentioning that there are other anion-doped MXenes being prepared, although not all of them have been employed in Li-S batteries. For example, phosphorus (P) atoms tend to occupy titanium vacancies due to the lowest formation free energy ($\Delta G_{P^*} = -0.028$ eV·Å^{-2}), and subsequently form bonds with surface groups on MXene ($\Delta G_{P^*} = 0.013$ eV·Å^{-2}) [114]. Additionally, sulfur and iodine atoms are more likely to bond with titanium as surface groups to form $Ti_3C_2S_2$ [115] or $Ti_3C_2I_2$ [99], which has already been discussed in section 3.2.

3.3.2. Cation-doped MXene

Various metal species, including Nb [116], V [117], Co [118], and Ru [119], have successfully doped MXenes and promoted their catalytic effect. For instance, Co was used to occupy Mo positions in Mo_2CT_x MXene and there was no cobalt-containing phases was detected [118]. Furthermore, the diverse coordination of Co atoms with other anions would enhance the adsorptive and catalytic activity of MXene [120].

Atomic-level metal doping on MXene can create new catalytic active sites, thereby reducing the reaction barrier for LiPS conversion. Yang et al. investigated the effect of Zn metal doping in Ti_3C_2 MXene [121]. During the etching process of Ti_3AlC_2 MAX with zinc chloride molten salt, single-atom zinc was implanted into the MXene (SA-Zn-MXene). As shown in the aberration-corrected high-angle annular dark-filed scanning transmission electron microscopy (HAADF-STEM) image (Fig. 8e), the white (or brighter) dots correspond to the doped Zn atoms in Ti_3C_2. The implantation of Zn atoms has increased the DOS around Fermi level, resulting in an elevation of energy levels within the valence band and thereby is beneficial for electron excitation in the SA-Zn-MXene. When introduced into a sulfur cathode, SA-Zn-MXene exhibited superior affinity to LiPS because of the high electronegativity of zinc in the MXene. The utilization of SA-Zn-MXene lowered the reaction barrier for the conversion from Li_2S_2 to Li_2S, decreasing it from 0.92 eV in pristine MXene to 0.71 eV. Consequently, the SA-Zn-MXene with 89 wt% sulfur delivered a high capacity of 1210 mAh g^{-1} at 0.2C and a high areal capacity of 5.3 mAh cm^{-2}. In 2023, Yang et al. reported another effective strategy for enhancing Li-S battery performance by doping single-atom Zn on S-terminated Ti_2C MXenes ($Ti_{2-x}Zn_xCS_2$) [122]. Doping single-atom Zn can create new Lewis acid-base sites, offering suitable adsorption towards LiPS. The lithium diffusion barrier on the surface of $Ti_{2-x}Zn_xCS_2$ is only 0.215 eV, which is lower than a lot of other wellresearched electrode materials such as graphite (~0.40 eV), graphene (~0.28 eV), O-terminated Ti_3C_2 MXene (~0.28 eV), and MoS_2 (~0.22 eV).

Metal species have also been introduced onto the MXene surface in the form of metal nanoparticles. This approach can enhance the anchoring strength of MXene to LiPS and accelerate Li-S redox reactions. Zhang et al. reported outstanding Li-S battery performance using Co nanoparticles-loaded Ti_2C MXene [123]. However, the enhanced performance is not attributed to the modified properties of MXene after Co loading, but rather to the synergistic effect of the two individual materials.

3.3.3. Co-doped MXene

Non-metal and metal atoms co-doped MXene may combine the advantages of both types of doping and deliver superior catalytic effects on Li-S batteries. For example, in the case of N, V-co-doped $Ti_3C_2T_x$ MXene, N-doping enhances electrical conductivity, while V-doping, with its highly polar features, contributes to inhibiting LiPS shuttling [124]. Moreover, the atomic size of vanadium is close to that of titanium, yet vanadium possesses a wider range in valence state, which is beneficial to accelarate the speed of electron transport. In 2023, Chen et al. reported a general vacancy-assisted strategy for implanting several metal atoms into the metal layer of nitrogen-doped MXenes (M−SA/N-$Ti_3C_2T_x$, M = Cu, Co, Ni, Mn, Zn, In, Sn, Pb, and Bi) [125]. Firstly, the few-layer $Ti_3C_2T_x$ nanoflakes with plenty of Ti vacancies were synthesized using an improved delamination method. The Ti vacancies exhibited high activity for reducing metal ions and served as anchoring sites for single metal atoms. Taking Cu SA/N-$Ti_3C_2T_x$ as a study instance: $CuCl_2$, melamine, and $Ti_3C_2T_x$ were mixed together and annealed at 500 °C. Cu^{2+} underwent the reduction process to occupy Ti vacancies, while nitrogen from melamine was doped onto the MXene. The introduction of nitrogen into MXene resulted in the redistribution of electronic structure and electrnegativity environment, thereby stabilizing the new implanted metal atoms and decreasing energy barriers to facilitate the conversion from LiPS to Li_2S_2/Li_2S. The isolated Cu atoms coordinated with N and C atoms to form the Cu-N_1C_2 unit, as shown in Fig. 8f and g. These asymmetric Cu-N_1C_2 units acted as new active sites for LiPS conversion, exhibiting higher binding energies and larger electron clouds compared to pristine $Ti_3C_2T_x$. When Cu SA/N-$Ti_3C_2T_x$ was used as a separator modifier, the Li-S battery showed the best performance among all tested metal dopants. It delivered high rate performance of 925 mAh g^{-1} at 3C, long cycling stability for over 1000 cycles, and high sulfur utilization (5.28 mg cm^{-2} with a sulfur loading of 7.19 mg cm^{-2}) [125].

4. Heterostructures and derivatives preparation from MXene

Although several internal modification methods have enabled MXene to improve the performance of Li-S batteries, MXenes still face the restacking issue due to intermolecular interactions such as Van der Waals forces and hydrogen bonding [126]. Fortunately, MXene-derived heterostructures can solve the restacking issue. The formation of heterogeneous interfaces on MXene affects its chemical composition, morphology, band structure, and charge carrier concentration [127]. When tuned properly, the chemisorption and conversion kinetics of LiPS on MXene-based heterostructures can be greatly improved while avoiding MXene restacking [128]. Moreover, the 2D layered structure and diverse metal compositions of MXenes provide the possibility to serve as templates for preparing morphology-controllable compounds [129]. This section summarizes the application of MXene-derived heterostructures and its derivatives in Li-S batteries.

4.1. Mxene-derived heterostructures

Many studies confirmed that transition metal oxides have strong adsorption to polysulfides, which can suppress the shuttle effect and increase the cycling life of Li-S batteries [130–133]. However, due to the poor conductivity of oxides, adding plenty of conductive carbon in electrode is usually necessary, which will inevitably sacrifice sulfur loading and energy density. Inducing partial surface oxidation, a simple but effective method to create MXene-metal oxide heterostructures, is a way to enhance the chemisorption to LiPS and promote its conversion while maintaining the high conductivity of the MXene matrix.

From the perspective of crystal structure, the mismatch of lattice parameters causes the occurrence of stress at the interface between Ti_3C_2 MXene and the oxidation layer TiO_2. Chen et al. performed simulations to investigate the electronic configuration and its impact on the surface adsorption properties of sulfur species after applying strain [134]. Compared to Ti_3C_2 with a surface oxidation layer (o-Ti_3C_2) in Fig. 9a, 5% lattice tensile strain was applied to the sample of o-TS-Ti_3C_2 (Fig. 9b). This small tensile strain did not impact the geometric configuration of o-TS-Ti_3C_2, but the length of Ti-Ti bond was extended compared to o-Ti_3C_2, which weakened the atomic interactions between each atom, resulting in a narrowed energy band. The partial DOS of the d-band was further analyzed to elucidate the changes in its band structure after applying the tensile strain. The o-Ti_3C_2 initially exhibited a d-band center of ~1.39 eV. However, in the case of o-TS-Ti_3C_2, there was orbital splitting coupled with an upshift of the d-band center, resulting in a significantly enhanced metal-absorbate interaction (Fig. 9c). Additionally, an increased DOS above the Fermi level and a reduced band gap were both evident in o-TS-Ti_3C_2, suggesting improved electrical conductivity. The o-TS-Ti_3C_2 also exhibited a much higher binding energy (2.75 eV) to Li_2S compared to o-Ti_3C_2 (2.12 eV), which would promote the nucleation and growth process of Li_2S on o-TS-Ti_3C_2 surface.

Hydrothermal treatment is a common technique to form MXene-oxide heterostructures by partially oxidizing MXenes. Yang's research showed that the hydrothemal duration effectively regulates the conversion from $Ti_3C_2T_x$ MXene to TiO_2 [135]. During the initial stage of hydrothermal treatments, the −F groups on the MXene surface is largely removed and replaced by −O groups. Then, some MXene flakes are further oxidized to TiO_2, crafting a TiO_2-MXene heterostructure. With longer oxidation time, the particle size of TiO_2 grows larger while its color changes from black to cloudy-white. This oxidation process during the hydrothermal treatment was verified by X-ray diffraction (XRD) and XPS measurements. As shown in Fig. 9d, the MXene's characteristic (002) peak decreased gradually as the oxidation proceeded, and the signature peaks for TiO_2 became stronger. XPS analysis in Fig. 9e examined the evolution process of F and O elements from 0 h to 4 h of hydrothermal treatment. The F terminals were gradually removed as the Ti-O bonds became increasingly stronger. Notably, only Ti-O peaks remained after 8 h of hydrothermal treatment, indicating that $Ti_3C_2T_x$ MXene was fully oxidized. Although TiO_2 has a strong adsorption ability for polysulfides, its conductivity is poor. It is necessary to balance the ratio between TiO_2 and MXene to achieve the optimal effect of both adsorption and conductivity. As illustrated in the schematic diagram (Fig. 9f), the TiO_2 nanoparticles serve as adsorption centers to trap LiPS. Meanwhile, the hetero-interface between MXene and TiO_2 guarantees fast diffusion of anchored LiPS from TiO_2 to MXene for further conversion. This TiO_2-MXene heterostructure combines several advantages, including high conductivity, large surface area, strong adsorption, and excellent catalytic activity for Li-S batteries. The heterostructure prepared by 4 h of hydrothermal treatment exhibited the best performance in Li-S batteries among all hydrothermal-treated samples. Its capacity decay rate was only 0.028% per cycle under 2C after 1000 cycles.

The surface oxidation process is also influenced by hydrothermal temperature. For example, Xiao et al. treated V_2C MXene by hydrothermal method at different temperatures of 140, 160, and 180 °C for 12 h [136]. The morphology of the corresponding products V_2C-140, V_2C-160, and V_2C-180, are completely different. As shown in SEM images, the structure of V_2C-140 was very similar to its precursor V_2C MXene, exhibiting a particular accordion-like structure (Fig. 10a). There were only tiny nanoribbons between the adjacent V_2C layers.

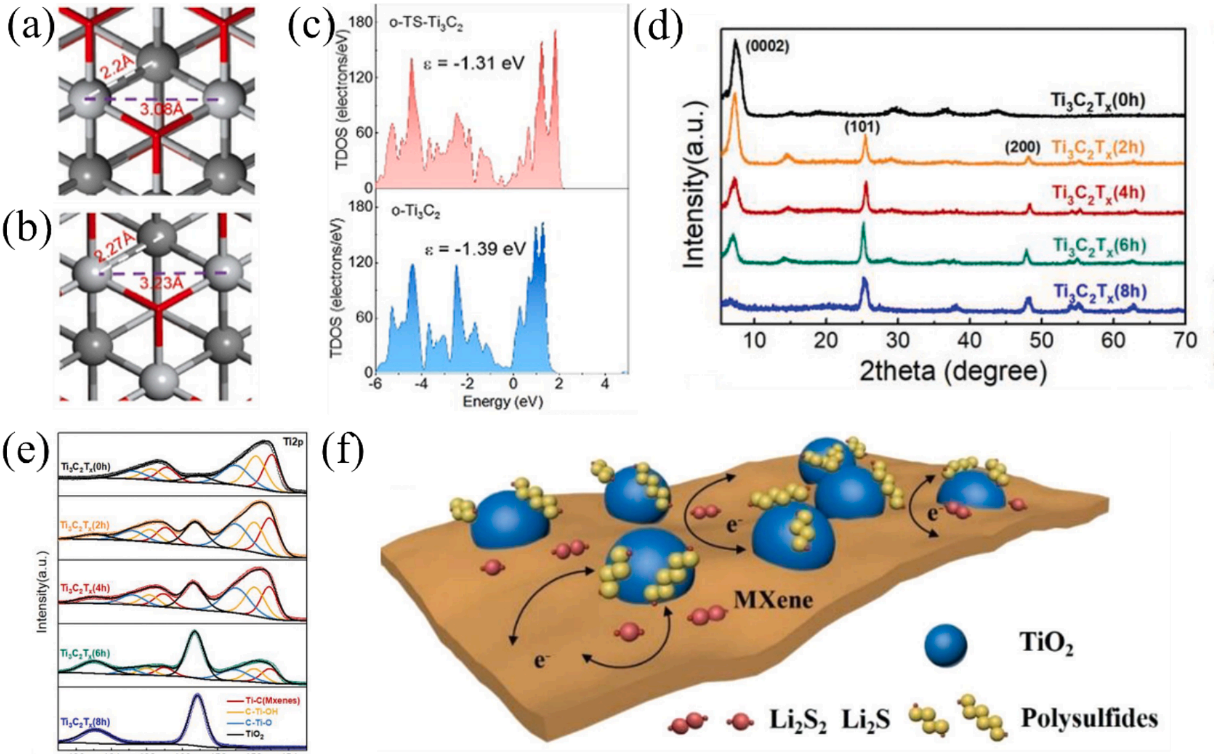

Fig. 9. Illustration for the design of strained Ti_3C_2: crystal structure and bond length of a)Ti_3C_2 MXene with oxidation layer (o-Ti_3C_2) and b)o-Ti_3C_2 was applied 5% lattice tensile strain (o-TS-Ti_3C_2); c) Density of states of Ti-3d orbitals for o-Ti_3 C_2 and o-TS-Ti_3C_2. Reproduced with permission: Copyright 2021, Wiley [134]. (d) XRD patterns of $Ti_3C_2T_x$ MXene with different oxidation times from 0 to 8 h. (e) Ti2p XPS spectra of $Ti_3C_2T_x$ MXene with different oxidation times from 0 to 8 h. (f) Schematic illustration of LiPS trapping and conversion process on TiO_2-$Ti_3C_2T_x$ heterostructures. Reproduced with permission: Copyright 2019, Wiley [135].

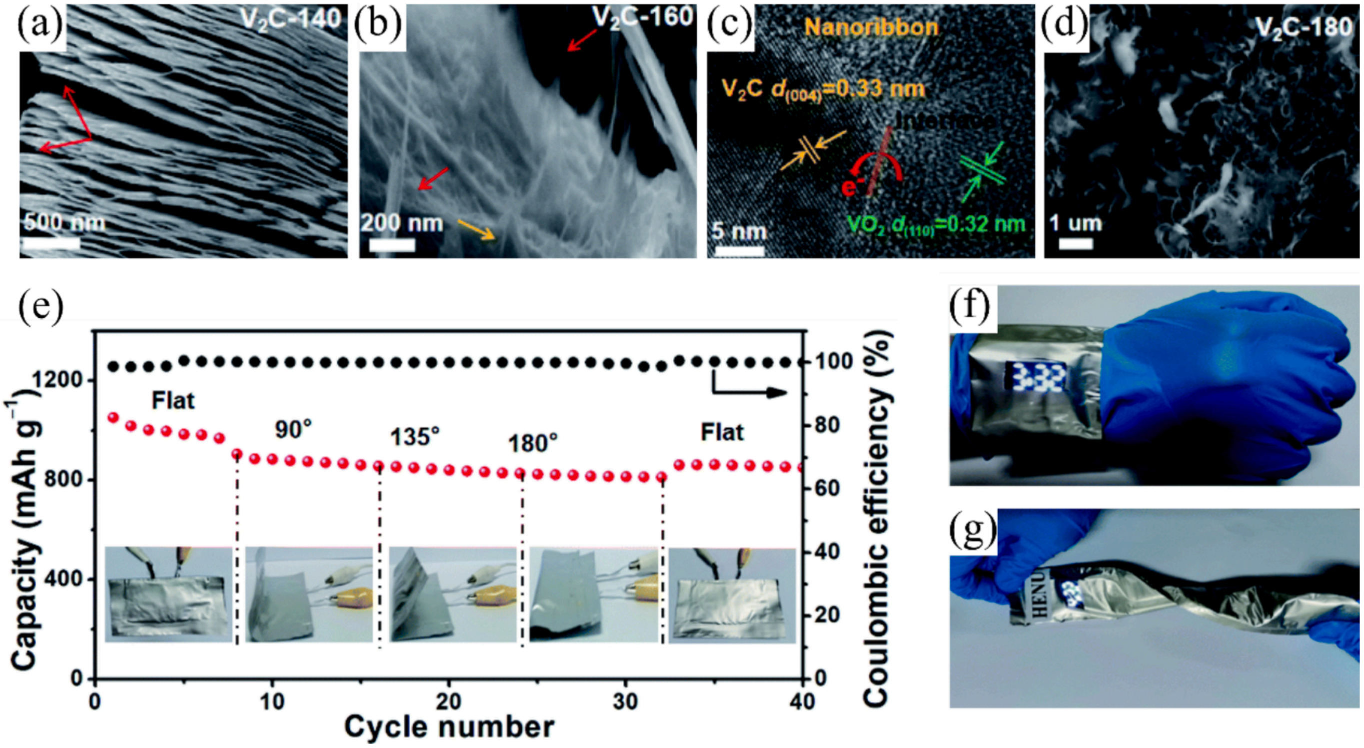

Fig. 10. (a) SEM image of V_2C-140 (140 °C hydrothermal treatment). (b) SEM image of V_2C-160 (160 °C hydrothermal treatment). (c) High-resolution transmission electron microscopy (HRTEM) images of V_2C-160 with the V_2C-VO_2 heterostructure. (d) Transmission electron microscopy (TEM) images of V_2C-180 (180 °C hydrothermal treatment). (e) Cycling performance of a flexible Li-S pouch cell at 0.2C based on the V_2C-160/S electrode under various bending angles. (f) and (g) Photographs showing the flexible bracelet battery powering an electronic watch. Reproduced with permission: Copyright 2021, Royal Society of Chemistry [136].

When the temperature increased to 160 °C, more nanoribbons aggregated between V_2C layers, forming an interlaced 3D structure (Fig. 10b). In the sample V_2C-160, the hetero-interface between V_2C (004) planes and VO_2 (110) planes was observed by high-resolution transmission electron microscopy (HRTEM) (Fig. 10c), which confirmed the formation of V_2C/VO_2 heterostructure. However, the layered structure of V_2C MXene completely vanished after hydrothermal treatment at 180 °C. Instead, a large number of randomly distributed entwined nanoribbons were observed (Fig. 10d). V_2C-160 demonstrated the largest specific surface area (156 m^2 g^{-1}) compared to V_2C-140 (52 m^2 g^{-1}) and V_2C-180 (99 m^2 g^{-1}). The nanoribbons between V_2C MXene layers prevented the restacking of MXene, which was beneficial for LiPS trapping and charge transfer. More importantly, V_2C-160 retained enough mechanical strength to fabricate free-standing electrodes after partial oxidation and sulfur loading. A pouch Li-S battery was assembled based on S/V_2C-160 cathode with a mass loading of 6.0 mg cm^{-2} and lean electrolytes (4.5 μL mg^{-1}_{sulfur}). The battery exhibited a capacity of 1052 mAh g^{-1} at a flat state, and there was no obvious capacity decay after physical bending/folding (Fig. 10e). Furthermore, the authors manufactured a wristwatch powered by this flexible Li-S pouch battery (Fig. 10f and g), demonstrating its enormous potential in flexible electronics applications. Additionally, V_2C MXene can be partially oxidized to different vanadium oxide species (e.g., VO_2 and V_2O_5) due to the wide range valence of vanadium. Both V_2C/V_2O_5 and V_2C/VO_2 heterostructures were verified to improve the sulfur confinement and accelerate the redox reaction kinetics [137,138].

Wei et al. proposed a one-step universal hydrothermal approach to prepare MO_x-MXene (M stands for Ti, V, and Nb) heterostructures directly from the MAX phase [139]. First, the MAX phase precursor ($Ti_3AlC_2/V_2AlC/Nb_2AlC$) was sealed with LiF/HCl solution for hydrothermal treatment. The sealed condition prevented the leakage of the in-situ formed HF and enhanced the etching efficiency. Simultaneously, an oxidation layer formed on the surface of MXene during the hydrothermal process. Among all the synthesized samples, VO_x-V_2C showed the best catalytic ability based on the Li_2S nucleation experiment. The VO_x-V_2C/S cathode also exhibited the best performance with 1645.98 mAh cm^{-3} or 1135.16 mAh g^{-1} (based on the whole mass of the composite cathode) at 0.2C.

High-temperature annealing under oxygen-containing gases (e.g., CO_2 and H_2O) was also used to oxidize MXene. Lee et al. oxidized delaminated $Ti_3C_2T_x$ MXene using CO_2 at high temperatures [140]. They found that the annealing temperature significantly impacts the properties of the resulting MXene. The MXenes annealed at 400, 500, and 600 °C could form free-standing films via filtrations. In comparison, the samples annealed at 700, 800, and 900 °C were fine powder-like after filtration due to the formation of the crystal rutile phase TiO_2. Song et al. prepared a Nb_2C/Nb_2O_5 heterostructure by annealing MXene under water steam environment at 600 °C for 10 min [141]. Notably, Nb_2C MXene can be fully oxidized after 30 min of annealing. This should be avoided as full oxidation leads to complete consumption of MXene and, hence, low conductivity. More importantly, the heterostructure offered unique electronic states that played a crucial role in the adsorption of LiPS, the diffusion of Li-ions, and the nucleation and decomposition of Li_2S. To investigate the adsorption ability, Li_2S_6 was taken as an example to construct adsorption structure with Nb_2C, Nb_2O_5, O-Nb_2C, and C-Nb_2O_5 (both from Nb_2C/Nb_2O_5 heterostructure), as shown in Fig. 11a. The adsorption energies of Li_2S_6 on Nb_2C (002), Nb_2O_5 (180), O-Nb_2C (002), and C-Nb_2O_5 (180) surfaces were estimated to be −1.98, −1.49, −2.35, and −1.72 eV, respectively. The enhanced adsorption energies at the hetero-interface are advantageous for inhibiting the migration of LiPS. Furthermore, O-Nb_2C and C-Nb_2O_5 exhibited lower Li^+ diffusion energy barriers than the pure Nb_2C and Nb_2O_5. It has also been observed that the decomposition energy barriers of Li_2S on O-Nb_2C (0.46 eV) and C-Nb_2O_5 (0.53 eV) were much lower than that of Nb_2C (0.57 eV) and Nb_2O_5 (0.95 eV), indicating enhanced catalytic effects of O- and C-Nb_2O_5.

In oxygen-free or inert gases, MXenes can be oxidized because of the existence of oxygen-containing surface groups or the addition of other organics [142]. This process is similar to those used to increase the oxygen surface groups through heat treatment [97]. But the oxidation process of MXenes goes further until the formation of metal oxides. For

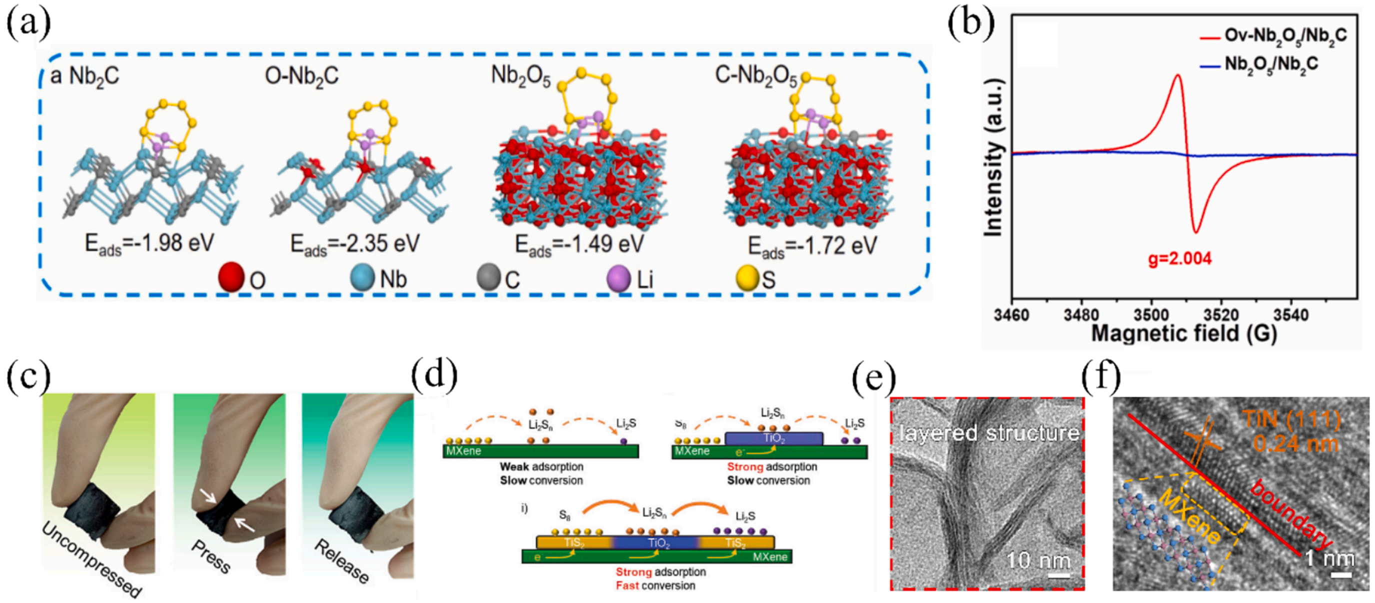

Fig. 11. (a) Optimized configurations of Li_2S_6 adsorption on the surface of Nb_2C, O-Nb_2C, Nb_2O_5, and C-Nb_2O_5. Reproduced with permission: Copyright 2022, Elsevier [141]. (b) Electron paramagnetic resonance (EPR) spectra of Ov-Nb_2O_5/Nb_2C and Nb_2O_5/Nb_2C tested at room temperature. Reproduced with permission: Copyright 2021, Elsevier [150]. (c) Photographs of the supercompression and elasticity of Mo-Ti/Mx-GN aerogel. Reproduced with permission: Copyright 2022, American Chemical Society [151]. (d) Schematic illustration of the conversion process of sulfur on the MXene, TiO_2@MXene, and TiS_2/TiO_2@MXene, respectively. Reproduced with permission: Copyright 2023, Wiley [152]. (e) TEM image of $Ti_3C_2T_x$-TiN heterostructure (MX-TiN). (f) HRTEM image of $Ti_3C_2T_x$-TiN heterostructure. Reproduced with permission: Copyright 2022, Springer [153].

example, delaminated Ti_3C_2 MXene was annealed with polydopamine (PDA) at 800 °C to fabricate N-doped carbon-coated Ti_3C_2-TiO_2 heterostructure (Ti_3C_2-TiO_2@NC) [143]. During the high-temperature pyrolysis, the rich hydroxyl and carbonyl from PDA facilitated the oxidation from Ti_3C_2 to TiO_2. Ta_4C_3 MXene shows higher air stability than Ti-based and other metal-based MXenes. Ta_4C_3 also possesses good mechanical properties with a high Young's modulus of 384 GPa [144]. For this kind of highly stable MXenes, pretreatment with oxidizing agents is necessary before the annealing process. First, dilute H_2O_2 was used to pre-oxidize and provide additional oxygen elements. Then, Ta_4C_3 was partially oxidized into quantum dot-sized Ta_2O_5 decorated on the surface of MXene during calcination under Ar/H_2 at 900 °C. The corresponding Li-S battery reached a high initial capacity of 801.9 mAh g^{-1} with a low decay rate of 0.086% per cycle for 500 cycles.

Modifying the electronic states of metal oxides presents a promising opportunity for achieving efficient surface catalysis, which is a critical factor in controlling the redox reactions of polysulfides in Li-S batteries [145]. For example, titanium dioxide with vacancies (TiO_{2-x}) showed a favorable adsorption ability towards LiPS. It can also catalyze the conversion of LiPS and the nucleation of Li_2S [146,147]. The oxide species generated by partially oxidizing MXenes typically contain a significant number of oxygen vacancies when there is insufficient oxygen. Alternatively, reduction treatments can also generate oxygen vacancies, such as annealing in a reducing atmosphere [148,149]. For example, oxygen vacancy-rich Nb_2O_5/Nb_2C heterojunction (Ov-Nb_2O_5/Nb_2C) catalysts were prepared from Nb_2C MXene by annealing it under H_2/Ar atmosphere. The oxygen vacancies only appeared in the sample annealed under H_2/Ar, not in the sample annealed in pure Ar, which was confirmed by the characteristic electron paramagnetic resonance (EPR) signal at $g = 2.004$ (Fig. 11b) [150]. In another work, Ti_nO_{2n-1}/$Ti_3C_2T_x$ hierarchical bifunctional electrocatalyst anchored on graphene was synthesized for free-standing and high-energy Li-S battery [151]. It is noteworthy that the incorporation of Ti_nO_{2n-1}/$Ti_3C_2T_x$ enhanced the mechanical properties of graphene aerogel. The composite aerogel can recover its original size even under high compression strain (Fig. 11c).

Nevertheless, the formation of oxides will inevitably reduce the electrical conductivity, which is undesirable in battery systems as it may lead to battery failure in practical applications. Compared to oxides, sulfides and nitrides, when combined with MXenes, can maintain higher conductivity and catalytic performance, making them more promising for applications of sulfur cathodes. For instance, TiS_2/TiO_2 was grown on the surface of Ti_3C_2 MXene (TiS_2/TiO_2@MXene) through a one-step partial sulfurization process [152]. During the sulfurization process, sulfur powder turned into sulfur gas at 600 °C, and then reacted with the exposed MXene. The sulfurization reaction can be expressed as $Ti_3C_2T_x + S \rightarrow Ti_3C_2T_x' + TiS_2 + CS_2$ (g). Simultaneously, part of Ti_3C_2 was oxidized to TiO_2 due to the presence of −O/−OH groups. TiS_2 and TiO_2 on the MXene surface played different roles in the redox reactions of Li-S battery. TiO_2 showed a much larger binding energy with Li_2S_6 (3.78 eV) compared to TiS_2 (1.12 eV) and F-terminated Ti_3C_2 MXene (1.05 eV). However, the high energy barrier for the Li_2S decomposition into polysulfides on the TiO_2 (1.31 eV) and MXene (0.89 eV) impeded reversible reactions. In contrast, the dissociation of Li_2S from TiS_2 should be easily due to the low energy barrier of 0.31 eV. Hence, the presence of both TiO_2 and TiS_2 led to the synergistic effect, which enabled the effective adsorption and rapid conversion of sulfur species (Fig. 11d). Simultaneously, the highly conductive MXene guaranteed fast electron transfer. Due to all the merits mentioned above, the S/TiS_2/TiO_2@MXene cathode delivered an initial capability of 1232 mA h g^{-1} at 0.1C, and superb cycling stability with 86.7% capacity retained after 100 cycles. Additionally, the cathode exhibited a highly compact structure with a high bulk density of 1.76 g cm^{-3}. Hence, the cathode showed an outstanding volumetric capacity of 1315 Ah L^{-1} (based on the the whole cathode) under the sulfur loading of 5.2 mg cm^{-2} and low electrolyte/sulfur ratio of 6 μL mg^{-1} [152].

In our previous study, ultrathin Ti_3C_2-TiN (MX-TiN) heterostructures were synthesized by annealing Ti_3C_2 MXene under Ar/NH_3 at 800 °C [153]. The surface of Ti_3C_2 MXene was oxidized to TiO_2 (MX-TiO_2) when NH_3 was absent. The sample annealed for 30 min was chosen for a case study to prevent the complete conversion of MXene to TiN. TEM images in Fig. 11e validated that the MX-TiN maintained the 2D layered structure. Upon further inspection with high-resolution TEM, the boundary between TiN and Ti_3C_2 MXene was discernible (Fig. 11f). DFT simulations indicated that all kinds of sulfur species (Li_2S_8, Li_2S_6, Li_2S_4, Li_2S_2, and Li_2S) interacted stronger with MX-TiN than with pristine $Ti_3C_2T_x$ MXene. The high-resolution S2p XPS revealed the coexistence of polysulfide (LiPS), thiosulfate ($[S_2O_3]^{2-}$), and polythionate ($[O_3S_2$-$(S)_{x-2}$-S_2O_3) after immersing MX-TiN in Li_2S_4 solution. The formation of sulfur species other than the polysulfides further confirmed the strong chemical interaction between MX-TiN and LiPS [154]. Based on the conversion energy calculated across multiple steps of LiPS conversions, it was identified that the transformation from Li_2S_2 to Li_2S should be the rate-limiting step. The conversion of Li_2S_2 to Li_2S on the surface of MX-TiN showed a much lower energy barrier than that of pristine MXene. Additionally, compared to S/MX-TiO_2 and S/MXene cathode, the high conductivity of TiN resulted in the lowest resistance for the cell with the S/MX-TiN cathode. The cathode using MX-TiN as the sulfur host materials achieved high-rate capability (593.9 mAh g^{-1} at 5C), long cycling stability (79.8% capacity retention after 1000 cycles), and high-areal capacity (8.27 mAh cm^{-2}) at a high mass loading of 10.16 mg cm^{-2} with lean electrolytes.

The above discussion highlights the heterogeneous structures derived from MXene in combination with oxides, sulfides, and nitrides. Each of these materials exhibits unique advantages. What if these materials were integrated to synthesize a highly chaotic MXene-based heterostructure? In a very recent report, Ti_3C_2 MXene simultaneously underwent oxidation, sulfuration, and nitridation to produce TiO_2, TiS_2, and TiN, together with the pristine MXene (TiS_2/TiN/TiO_2/$Ti_3C_2T_x$) to create a high-entropy heterostructure [155]. This MXene-derived high-entropy heterostructure acts as an excellent electrocatalyst in sulfur cathode. Compared to the moderately chaotic MXene-based heterostructure (TiO_2/TiN/$Ti_3C_2T_x$), it exhibits superior catalytic ability, especially in lowering the Gibbs energy barriers in both of Li_2S_2/Li_2S reduction and decomposition.

4.2. *MXene derivatives*

As an alternative approach to the partial oxidation/sulfuration/nitridation of MXenes, many researchers also worked on the complete transformation of MXene [129,147,156]. Sun and his colleagues fabricated porous carbon nanosheets decorated with oxygen vacancy-rich Ti_nO_{2n-1} quantum dots(OV-T_nQDs@PCN) from the $Ti_3C_2T_x$ MXene precursor [129]. As shown in Fig. 12**a**, H_2O_2 was used to oxidize MXene, which was then annealed at 1000 °C under Ar/H_2 to create oxygen vacancies. The porous carbon nanosheets in the final product originated from the carbon elements in $Ti_3C_2T_x$, and they inherited the 2D morphology of the MXene nanosheet (Fig. 12b). The OV-T_nQDs@PCN sheet, with a thickness of ~3.5 nm, showed a rough surface, which provided enough space to accommodate the volume change during discharge. The confinement effect of porous carbon prevented further growth and aggregation of crystalline oxides. The ultrafine Ti_nO_{2n-1} quantum dots, with a diameter of only ~3.3 nm, exposed more surface oxygen vacancies, improving interaction with LiPS. First-principle DFT calculations revealed that introducing oxygen vacancies enhanced the chemical interaction for Li_2S_4 by shortening the bond lengths between Li_2S_4 and T_nQDs. To investigate the electrochemical reactions during battery cycling, the authors performed in situ Raman, as shown in Fig. 12c. During the initial discharge process from open circuit potential (OCP) to 2.30 V, the primary characteristic peaks for S_8 and S_8^{2-} gradually diminished, following by the formation of polysulfides (S_x^{2-}, $x = 4$–8) and $S_2O_3^{2-}$. Afterward, the peaks of S_x^{2-} and $S_2O_3^{2-}$ vanished, while new peaks of S_4^{2-} and $S_xO_6^{2-}$ emerged and increased during further discharge

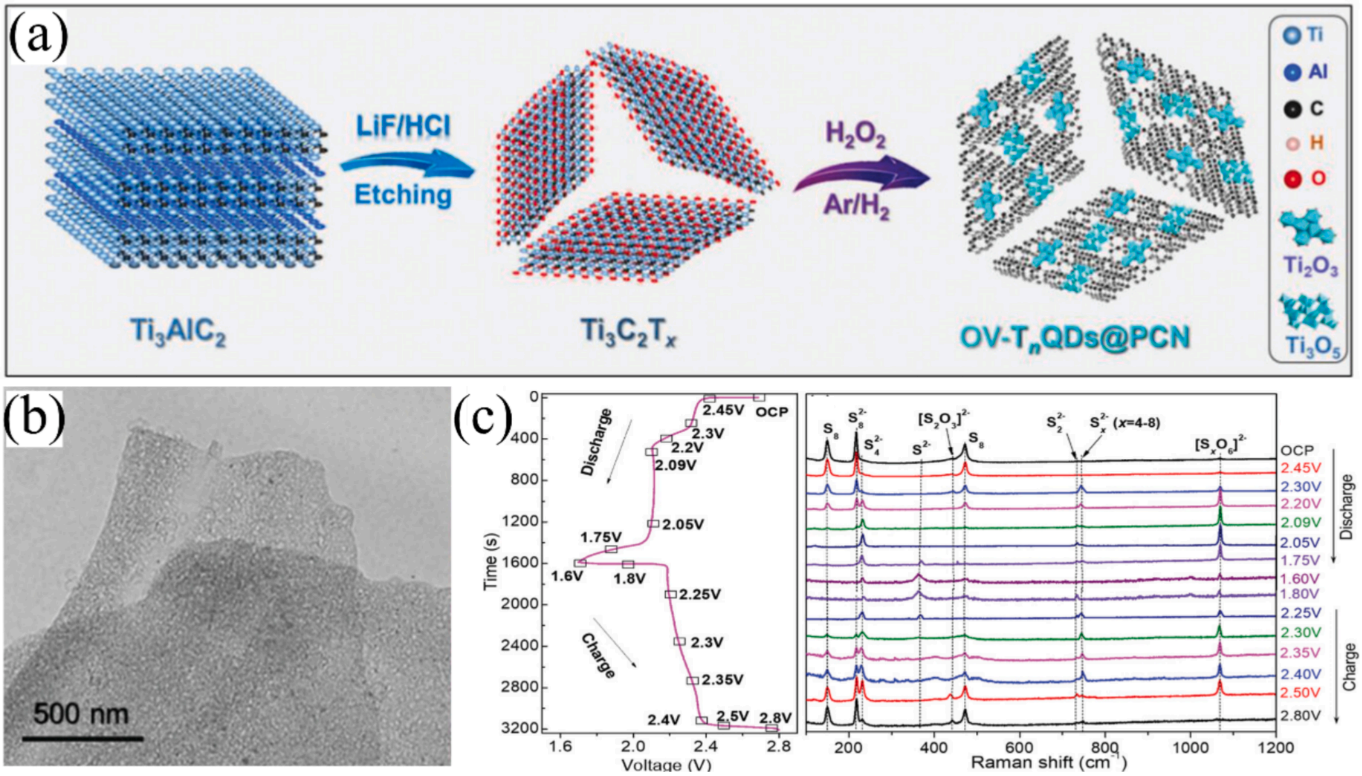

Fig. 12. (a) Schematic preparation procedure of OV-TnQDs@PCN. (b) TEM image of OV-T_nQDs@PCN. (c) First discharge/charge profiles and corresponding in situ Raman spectra of OV-T_nQDs@PCN/S. Reproduced with permission: Copyright 2021, Wiley [129].

(2.30–2.05 V). The S^{2-} peak appeared and gradually increased to become the dominant peak at the final discharge from 2.05 to 1.60 V. The reaction process was concluded as $S_8 \rightarrow S_x^{2-} + S_2O_3^{2-} \rightarrow S_4^{2-} + S_xO_6^{2-} \rightarrow S^{2-}$. During the charging process, the opposite reaction was observed, implying good reversibility under the catalytic effect of OV-T_nQDs@PCN. As a result, the OV-T_nQDs@PCN/S cathode exhibited high capacity retention of 88% after 1000 cycles at 2C. In another report, $Ti_3C_2T_x$ MXene was utilized as the sacrificial material to construct TiO_2 anatase/rutile homojunction (A/R-TiO_2) with oxygen vacancies. Such configuration was reported to exhibit efficient LiPS immobilization and highly effective catalytic effects on the LiPS conversion [147].

A similar strategy was also applicable for preparing metal oxides/sulfides by sacrificing non-Ti-based MXenes. Nb_2C MXene was oxidized to prepare Nb_2O_5 with an amorphous carbon composite (Nb_2O_5/C) [156]. The Nb_2O_5/C with high conductivity was directly employed as a sulfur host, which mitigated the shuttle effect and accelerated LiPS conversion. In addition, V_2CT_x was applied as both a vanadium source and structural template to obtain 3D V_3S_4@C flakes by annealing it with thioacetamide [157]. Temperature optimization revealed that the sample obtained from 700 °C annealing achieved the best performance. The corresponding Li-S battery delivered high-rate capability (690.1 mAh g^{-1}) and long cycling life with a low capacity decay rate of 0.06% over 1000 cycles at 2C.

5. Fabrication of MXene-based composites

Besides MXene-based heterostructures directly derived from MXene's precursor, combing MXene with other materials to fabricate MXene-based composites allows for the selection of other materials tailored to address specific issues. In this way, the composites inherit the material properties of each component, which can exert synergistic effects to address the issues that cannot be solved by MXene (or another material) alone. This also provides more options and possibilities for the application of MXene in the cathode of Li-S batteries. This section summarizes and categorizes various MXene-based composites used in Li-S batteries, including MXene-carbon, MXene-transition metal compounds, MXene-MOF, and MXene-organic composites, and provides principles for selecting suitable materials for composite integration.

5.1. MXene-carbon composites

MXenes exhibit good dispersibility in water due to their hydrophilic surface terminations and negatively charged surface. However, they tend to restack during the drying process, losing accessible surface area. The restacking problem also hides the active sites, preventing their interaction with sulfur species. Besides, the interfacial ion transport resistance will also be larger, leading to lower rate capability. To address the restacking issue of MXenes, researchers incorporated MXene with various carbon materials, which could bring about good conductivity, large specific surface area, and diverse morphologies to the composites.

Mesoporous carbon possesses a large pore volume, an interconnected porous framework, and high conductivity, making it suitable for sulfur storage. The abundant pores can also accommodate the sulfur expansion during lithiation and provide space for electrolyte infiltration. In 2009, Nazar and her co-workers utilized a well-known mesoporous carbon CMK-3 as a sulfur host, which exhibited a high reversible capacity of 1320 mAh g^{-1} [17]. The mesoporous carbon not only served as the high-speed electron transport pathway but also confined sulfur within its porous structure. However, due to the nonpolar characteristics of carbon materials, their adsorption with LiPS is very limited, leading to poor cycling stability. A porous 2D carbon/MXene composite was synthesized by uniformly grafting mesoporous carbon on both sides of the MXene (OMC-g-MXene) [158]. During the synthesis process, the organic Polyether-F127/resol composites were attached on both sides of MXene flakes due to the interaction between the –OH/-F terminations of MXene and the polymer groups. By annealing the as-synthesized precursor under H_2/Ar at 500 °C, the organic F127/resol was transformed into ordered mesoporous carbon. Meanwhile, the bonds between the organics and MXene were converted into electronically conductive bridges. Due to the constructed mesoporous structure, the OMC-g-MXene exhibited a high specific surface area of 202.36 m^2 g^{-1}, which is much larger than the densely packed MXene with a surface area of 17.52 m^2 g^{-1}. Moreover, many vacancies and defects were formed during the synthesis process, benefiting ion migration and catalysis effect. As shown in the discharge/charge curves in Fig. 13a, Q1 and Q2 represented the capacity of the first and second plateau, respectively. Q1 represents the capacity for the reduction of S_8 to Li_2S_n ($n \geq 4$), while Q2 is the capacity for further conversion of Li_2S_4 into Li_2S/Li_2S_2. In this situation, the Q2/Q1 represents the amount of LiPS conversion to the final product, which also reflects the catalytic ability of the LiPS conversion. The battery with OMC-g-MXene exhibited a high Q2/Q1 ratio of 2.25 (Fig. 13b) and a longer second plateau than pure MXene or OMC, indicating enhanced sulfur utilization.

During the early stages of MXene application in Li-S batteries in 2017, carbon nanotubes (CNTs) were already being used as interlayer spacers [74]. By introducing merely 10 wt% of CNT to Ti_2C and Ti_3C_2 MXene, or 20 wt% to Ti_3CN MXene, the surface area of MXene-CNT composites increased significantly, exceeding the sum of pristine MXene and CNT (Fig. 13c). In these composites, CNTs were well dispersed in-between MXene sheets, effectively inhibiting the restacking of MXene and increasing the porosity of composites to accommodate more sulfur. Additionally, the presence of CNTs increased the electronic conductivity in-plane and across the nanosheets. Compared to the S/Ti_2C cathode without CNTs, enhanced electrochemical performance was observed even at a higher sulfur content (83 vs. 70 wt%) and a larger areal loading (1.5 vs. 1.0 mg cm^{-2}). Under more precise control, MXene and CNTs can form more regular and complex structures. As shown in Fig. 13d, a unidirectional freeze-drying method was applied to fabricate MXene/CNT aerogels [159]. During this process, ice crystals grew in a specific direction, aiding the alignment of MXene nanosheets to create lamellar aerogels. After the freeze-drying process, the open structure of the aerogels (Fig. 13 e-g) improved the electrode/electrolyte contact. This structure was capable of physically blocking LiPS shuttling and increased the exposure of LiPS to the MXene surface to enhance chemical trapping and catalytic conversion. Moreover, the CNTs also established a highly conductive network, facilitating rapid charging/discharging capabilities [96]. The corresponding Li-S battery delivered a remarkable capacity of 712 mAh g^{-1} with a high sulfur loading of 7 mg cm^{-2}. Additionally, it demonstrated exceptional cycling stability, with only 0.025% capacity loss per cycle over 800 cycles at 0.5C. In our previous work, we fabricated a 3D cage-like S-CNT@MXene framework. First, nano-sized sulfur particles were attached to CNTs to form S-CNT spheres. Then, S-CNT was coated with a layer of MXene. The addition of highly conductive CNTs prevented the MXene restacking and expanded the Li^+ diffusion channels, which ensured stable cycling under high currents. Additionally, the MXene that is coated as the outer layer confined the sulfur conversion within the cage, inhibiting the shuttle effect. The synergistic effect resulted in a high Li-S battery performance

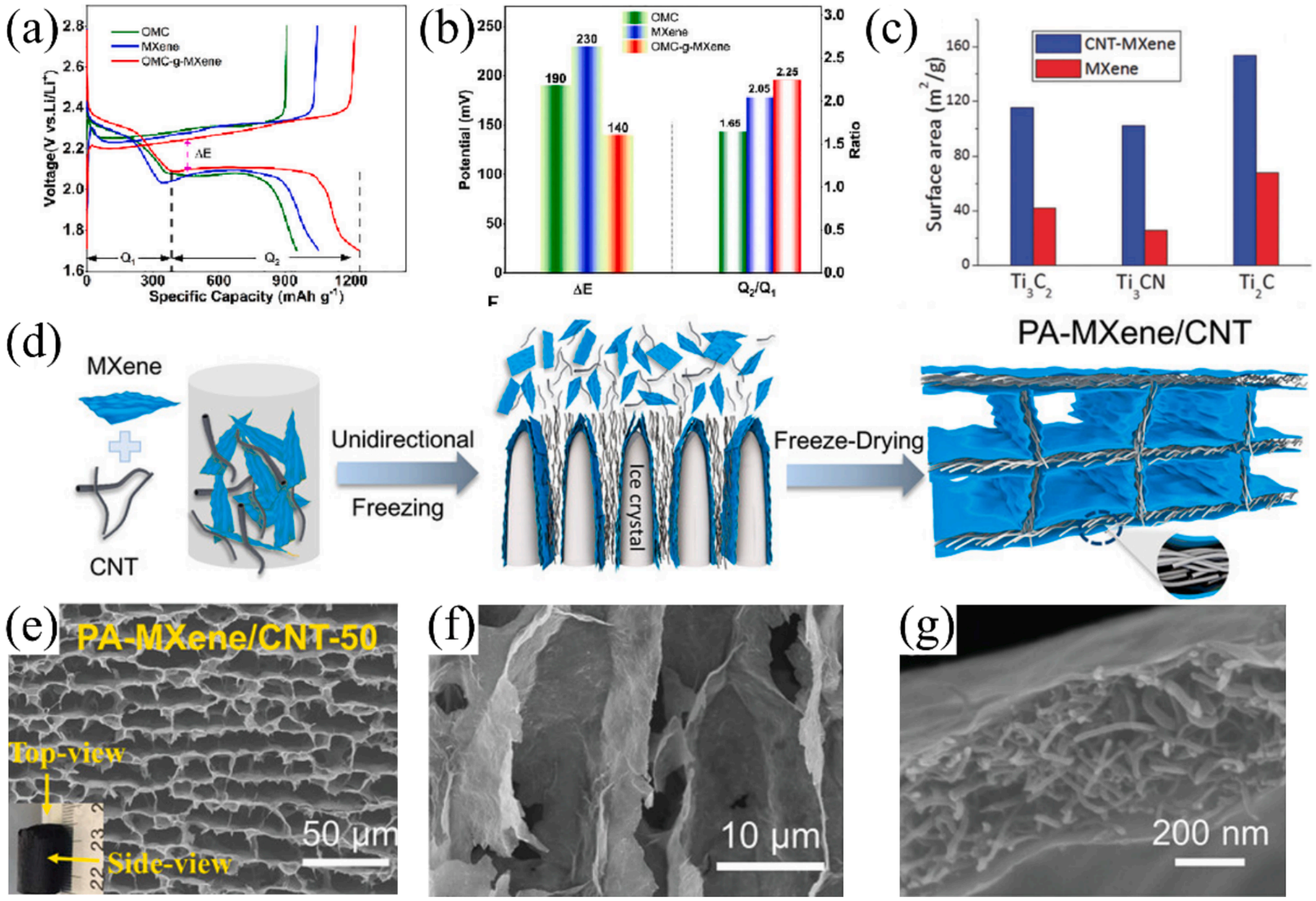

Fig. 13. (a) Comparison of discharge–charge profiles of Li-S batteries based on various modified separators at 0.2C. (b) The corresponding summaries of ΔE and Q_2/Q_1 ratio at 0.2C. Reproduced with permission: Copyright 2023, American Chemical Society [158]. (c) Comparison of the surface area of delaminated MXene nanosheets and CNT-MXene composites, measured by the BET method. Reproduced with permission: Copyright 2017, Wiley [74]. (d) Schematic assembly process of PA-MXene/CNT aerogel by unidirectional freeze-drying. SEM images of (e) top-view (inset is a photo of the PA-MXene/CNT-50 monolith), (f) SEM image of side-view and (g) high magnification of the PA-MXene/CNT-50 aerogel. Reproduced with permission: Copyright 2021, Wiley [159].

that the battery delivered a high capacity of 557.3 mAh g^{-1} at 8C and experienced minimal capacity loss after 150 cycles under a high current density of 4C [96].

Graphene, the most extensively investigated 2D material, possesses great structural flexibility and conductivity. Graphene can be combined with MXene to construct a 3D conductive network, shortening the ion/electron transport distance and enhancing the reaction kinetics and rate performance [160]. Due to its lightweight and 2D structure, graphene is a suitable material for preparing conductive aerogels [161]. The MXene/graphene hybrid (MX/G) aerogel can easily be synthesized using a one-step hydrothermal process followed by freeze-drying [162]. It's worth noting that adding some ascorbic acid during the hydrothermal process promotes the reduction of graphene and prevents the oxidation of MXene. The as-prepared MX/G aerogel is 3D porous-structured and free-standing. It can be used directly in Li-S batteries by loading Li_2S_6 catholyte as cathodes without using conductive carbon, binder, and current collector. The aerogel with 30 wt% MXene (MX/G-30) delivered a high capacity of 946 mAh g^{-1} at 1C after activating for 3 cycles at 0.05C. Additionally, the MX/G-30 electrode exhibited only 0.07% capacity decay per cycle and maintained a high Coulombic efficiency of close to 100%. In another research, the oxidation resistance of $Ti_3C_2T_x$ MXene was significantly improved because of the presence of reduced graphene (rGO) [163]. Liu et al. employed a $Ti_3C_2T_x$/GO composite as a functional interlayer between the separator and sulfur to trap LiPS species. The porous and rough surface of the $Ti_3C_2T_x$/GO composite also improved the wettability of the commercial separator in an ether-based electrolyte [164].

5.2. Mxene-transition metal compound composites

MXene-transition metal compound compositions are among the most widely studied in Li-S batteries due to their diversity and simple synthesis process. For instance, transition metal oxides exhibit natural surface polarity and possess high adsorption affinities to LiPS. Transition metal sulfides, selenides, and antimonides show moderate adsorption ability to LiPS and demonstrate outstanding catalytic effects to facilitate the conversion of LiPS [165,166]. The shuttle effect can also be alleviated by the rapid nucleation and decomposition of Li_2S [22]. Moreover, metal compounds usually possess higher bulk material densities than carbon, which is advantageous for preparing compact electrodes and achieving higher volumetric energy density [128].

A MoS_2-MXene composite was reported to modify the separators of Li-S batteries. As shown in Fig. 14**a**, ionic liquid-assisted ultrasonic exfoliated MoS_2 (IL-MoS_2) and $Ti_3C_2T_x$ MXene were mixed and filtered to obtain a 2D/2D heterostructure. This structure effectively integrated the advantages of two materials: MXene offered abundant surface

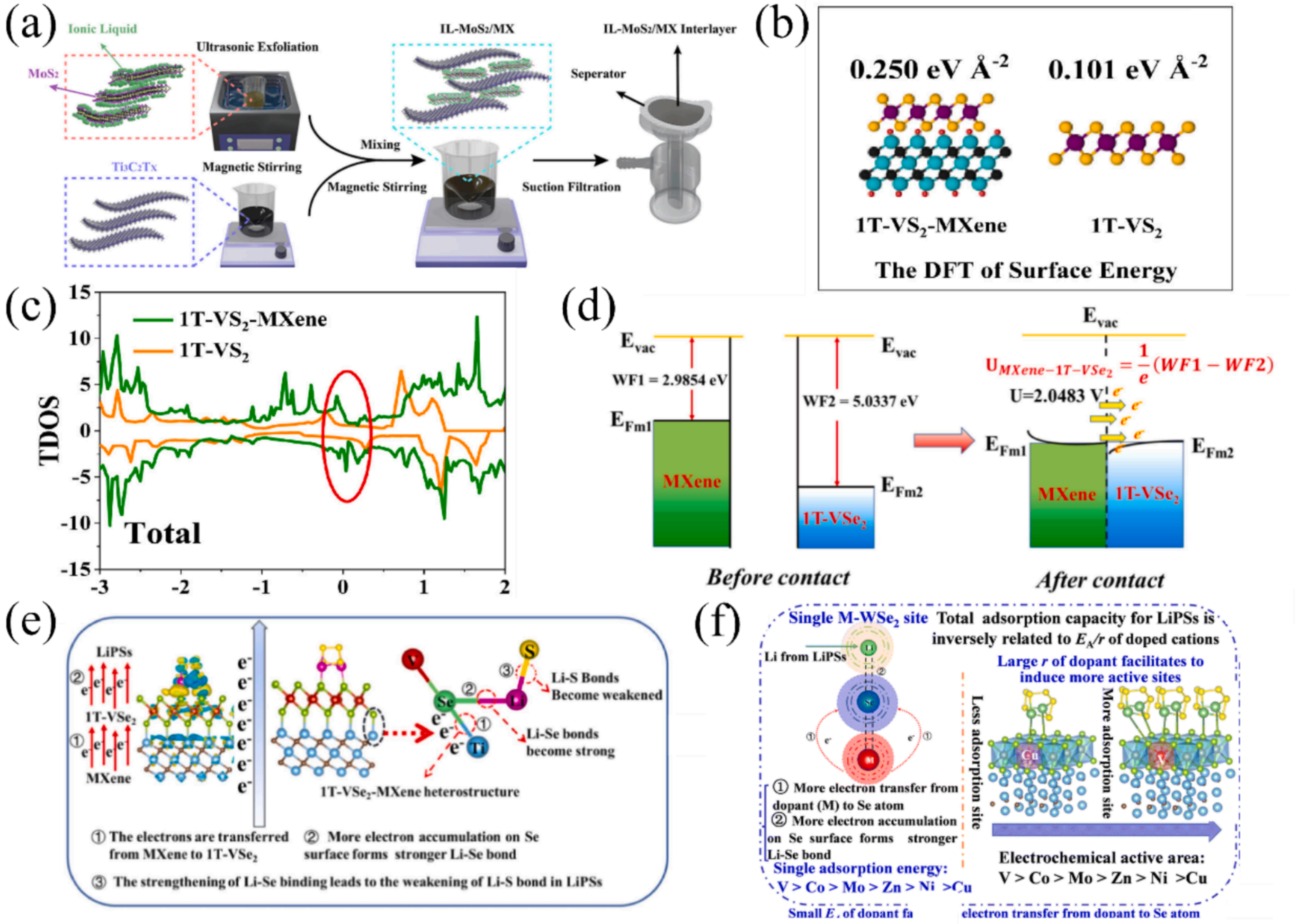

Fig. 14. (a) Schematic of the preparation process and mechanism of IL-MoS_2/MX interlayer. Reproduced with permission: Copyright 2023, Elsevier [167]. (b) Surface energies of the 1 T-VS_2 -MXene heterostructure and 1 T-VS_2. (c) Total density of states (TDOS) plots of main orbital contributions for V and S elements of the 1 T-VS_2-MXene heterostructure and 1 T-VS_2. Reproduced with permission: Copyright 2022, Elsevier [169]. (d) Schematic illustration and work functions of 1 T-VSe_2 and MXene before and after contact each other. (e) Schematic illustration of the adsorption and electro-catalytic mechanism of the 1 T-VSe_2-MXene heterostructure for bidirectional sulfur redox. Reproduced with permission: Copyright 2023, Elsevier [170]. (f) The relationship between adsorption energy and the E_A/r. Reproduced with permission: Copyright 2023, Royal Society of Chemistry [171].

functional groups and high electronic conductivity, while IL-MoS_2 provided the catalytic ability for LiPS conversion [167]. CoS_2 is also regarded as a good catalyst for Li-S batteries due to its high binding energy to LiPS and commercial feasibility. Peng et al. proposed a strategy to load CoS_2 nanoparticles on an alkali-treated $Ti_3C_2T_x$ MXene (MX@CoS_2) [168]. The alkali-treated MXene contained more oxygen groups than pristine MXenes, which promoted the growth of CoS_2 on the MXene surface. Moreover, Ti-O-Co bonds at the interface of MX@CoS_2 guaranteed rapid electron transfer from MXene to CoS_2. CNTs have been further introduced to the MX@CoS_2 to modify the commercial polypropylene (PP) separator (MCCoS/PP). CNTs prevented MXene layers from restacking and retained more active surface sites. This well-designed multi-dimensional frame resulted in rapid reaction kinetics and long cycling stability. The Li-S battery utilizing the MCCoS/PP separator showed a high capacity of 368.6 mAh g^{-1} at an extremely high current density of 20C and a low capacity-decay rate of 0.033% for 1000 cycles at 7C.

The transition metal sulfide-MXene composites have also been used as the sulfur hosting material. For example, compared to the semiconducting 2H-VS_2, the 1 T metallic phase of VS_2 (1 T-VS_2) stands out as a more promising sulfur host material, attributed to its enhanced electronic conductivity, outstanding hydrophilicity, and electrochemically reactive sites. When integrating 1 T-VS_2 with $Ti_3C_2T_x$ MXene, 1 T-VS_2-MXene displayed better electronic properties than bare 1 T-VS_2 [169]. The conductivity of 1 T-VS_2-MXene (98.2 S m^{-1}) was slightly lower than that of pure MXene (102.5 S m^{-1}), yet significantly higher than that of 2H-VS_2(35.2 S m^{-1}). As shown in Fig. 14b, the surface energy of the 1 T-VS_2-MXene heterostructure (0.250 eV Å^{-2}) exceeded that of 1 T-VS_2 nanosheets (0.101 eV Å^{-2}), indicating that the 1 T-VS_2-MXene exhibited more superior catalytic activity for rapid redox kinetics and more uniform Li_2S nucleation than the 1 T-VS_2. The total DOS further revealed a higher E_p position of V and S DOS on 1 T-VS_2-MXene than 1 T-VS_2, suggesting stronger LiPS adsorption on the composite (Fig. 14c). Moreover, the S-loaded 1 T-VS_2-MXene showed a high material density of ~ 1.91 g cm^{-3}. As a result, the S-loaded 1 T-VS_2-MXene achieved a large initial volumetric capacity of 1571 Ah L^{-1} at 0.1C based on the volume of the whole cathode, a gravimetric capacity of ~1430 mAh g^{-1} based on sulfur, and a good long-term cycling stability with ~75% capacity retention after 500 cycles at 1C.

Transition metal selenides show similar crystal structures to the transition metal sulfides because of the similar ionic radius and electronegativity of Se and S. Meanwhile, selenides may be more appealing as sulfur hosts since they possess higher electronic conductivity than sulfides [128]. Similar to the preparation of 1 T-VS_2-MXene, a 1 T-VSe_2-MXene electrocatalyst was synthesized using a simple solvothermal method. The 1 T-VSe_2-MXene exhibited an interfacial built-in electric field (BIEF) effect [170]. Specifically, the electrons would transfer from MXene to 1 T-VSe_2 until a thermodynamic equilibrium was reached in the 1 T-VSe_2-$Ti_3C_2T_x$ (Fig. 14d). The decrease of the charge density near Ti atoms resulted in an accumulation of charge density of the adjacent Se atoms. Such an electron transfer process promoted the formation of strong Li-Se bonding between 1 T-VSe_2 and LiPS. The enhanced Li-Se bonds would weaken the binding energy of Li-S bonds in LiPS/Li_2S, which reduced the energy required for dissociating Li-S bonds and accelerated the conversion of LiPS and nucleation/decomposition of Li_2S (Fig. 14e).

Atomic metal doping into transition-metal dichalcogenides has been explored to promote the multi-step sulfur redox in Li-S batteries. Li et al. proposed a rational design principle for selecting suitable metal-cation dopants to adjust their catalytic activity [171]. Several metal dopants were doped into WSe_2 and mixed with $Ti_3C_2T_x$ to prepare M−WSe_2/MXene (M = V, Co, Mo, Zn, Ni, and Cu) catalysts. In this case, MXene served as the highly conductive scaffold in M−WSe_2/MXene to facilitate the rapid electron transfer. They discovered a strong correlation between catalytic ability and the ratio of E_A/r, where E_A is the electron affinity and r is the ionic radius of metal dopants. The authors further suggested that a low E_A/r value of doped metal atoms could significantly enhance the bidirectional sulfur conversion and reduce the activation energy. Metal-dopants with small electron affinity tend to lose electrons, which leads to electron accumulation on the surface of adjacent atoms, thus affecting the catalytic performance [171]. Metal cation dopants, including V, Co, Mo, Zn, Ni, and Cu, are prone to lose electrons to Se-M bonds following the order: V (1.194 e), Co (0.839 e), Mo (0.640 e), Zn (0.359 e), Ni (0.348 e), and Cu (0.335 e). The reconstruction of electronic structures of M−WSe_2 enhanced the conductivity and catalytic activity, as well as increased the electron density on the Se surface sites. Hence, stronger Li-Se bonds can be formed, leading to increased adsorption capability to LiPS on the surface of M−WSe_2(Fig. 14f). As a result, the V-MSe_2/MXene with the lowest E_A/r presented the highest reversible capacity of 1402.5 mAh g^{-1} at 0.1C and the most stable cycling performance of ~70.8% capacity retention after 800 cycles at 1C.

In addition to the above mentioned transition metal chalcogenides, various other transition metal compounds, including metal oxides [172], phosphides [173], borides [174], and metal nanoparticles [175], have been incorporated with MXene matrix to enhance the performance of Li-S batteries. These composites were designed to modulate the adsorption-diffusion-conversion behavior for sulfur species, yielding significant advancements in performance. Among these composites, Li-S batteries with transition metal selenides and borides usually exhibited better rate performance due to their higher electronic conductivity.

5.3. MXene-MOF composites

Metal-organic frameworks (MOFs) possess favorable properties such as tunable pore size, large surface area, high porosity, and controllable structure. These advantages make MOFs and their derivatives highly attractive for Li-S battery applications [176]. For example, MOF-based separators can act as ionic sieves, which can selectively screen Li^+ ions while efficiently suppressing undesired LiPS shuttling to the anode side [177,178]. However, most MOFs are electrically insulative due to ligands blocking active metal sites, which inevitably worsens the rate capacity.

A novel $Ti_3C_2T_x$/Ni-Co MOF composite was recently reported to enhance the performance of Li-S batteries when used as a multifunctional modifier of a commercial PP separator [179]. During its synthesis, as illustrated in Fig. 15a, Ni^{2+}, Co^{2+}, and 1,4-Benzenedicarboxylic acid were attached spontaneously on the $Ti_3C_2T_x$ surface because of the abundant functional groups of MXene. Then, the ultrathin Ni-Co MOFs with a thickness of about 4 nm were in-situ grown on the surface of $Ti_3C_2T_x$ MXene through continuous ultrasonic treatment. After that, the $Ti_3C_2T_x$/Ni-Co MOF was coated on the PP separator by vacuum filtration. The $Ti_3C_2T_x$/Ni-Co MOF@PP contained relatively smaller and more dense channels than that of pristine PP or $Ti_3C_2T_x$@PP, leading to less LiPS shuttling and lower Li^+ diffusion resistance. The Li_2S nucleation tests with $Ti_3C_2T_x$/Ni-Co MOF as an electrode also exhibited a higher Li_2S precipitation capacity, demonstrating a remarkable electrocatalytic effect toward Li_2S nucleation. As a result, the Li-S battery with the $Ti_3C_2T_x$/Ni-Co MOF modified separator achieved a high reversible capacity of 1260 mAh g^{-1} at 0.2C, along with good cycling stability, retaining 91.1% after 350 cycles at 0.5C.

In another report, the large surface area and high porosity of MOFs were utilized to provide abundant space for sulfur storage, accommodating the volume change and favoring LiPS adsorption. Compared to the layered $Ti_3C_2T_x$ MXene with a limited surface area (58 m^2 g^{-1}) and a small pore volume (0.15 cm^3 g^{-1}), Zr-MOF showed a large specific area of 1054.7 m^2 g^{-1} and pore volume of 0.47 cm^3 g^{-1}. After the in-situ growth of Zr-MOF on $Ti_3C_2T_x$ MXene, the Zr-MOF/$Ti_3C_2T_x$ composite maintained a high surface area of 911.5 m^2 g^{-1} and a high pore volume of 0.36 cm^3 g^{-1} [180].

MOFs exhibit specific 2D or 3D morphologies due to different coordination and metal centers. The MXene-MOF precursor can be utilized to

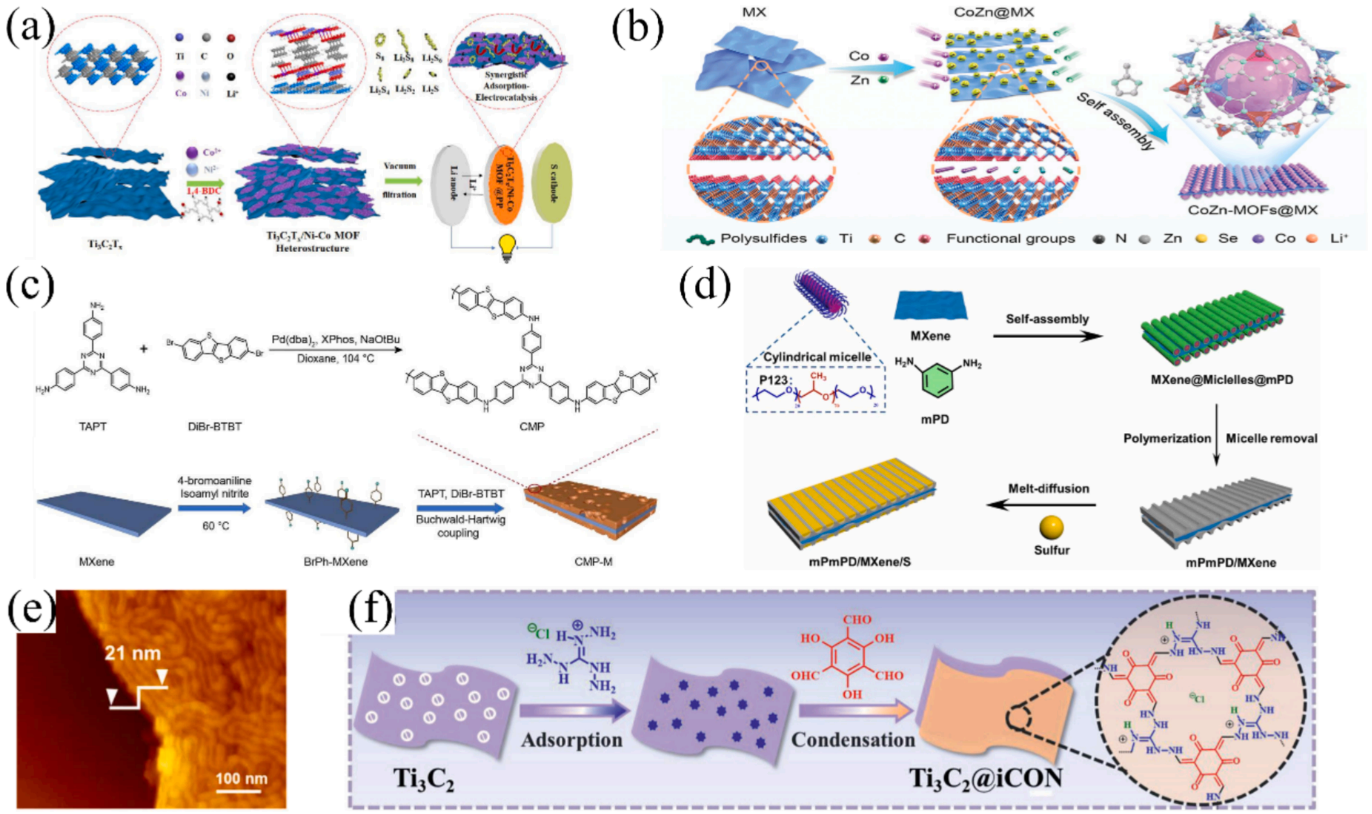

Fig. 15. (a) Schematic illustration of the synthesis of the 2D/2D $Ti_3C_2T_x$/Ni-Co MOF heterostructure. Reproduced with permission: Copyright 2022, Elsevier [179]. (b) Synthesis process illustration of CoZn-Se@N-MX, the structure of the as-prepared electrocatalyst, and the application of catalytic cathode in a Li-S battery. Reproduced with permission: Copyright 2021, Wiley [181]. (c) Synthetic routes used to prepare the CMP and the CMP-M. Reproduced with permission: Copyright 2022, Elsevier [183]. (d) The construction of the 2D mPmPD/MXene heterostructures with in-plane cylindrical mesochannels and their corresponding sulfur loading process. (e) Atomic force microscopy (AFM) height profile of mPmPD/MXene. Reproduced with permission: Copyright 2023, IOP Science [184]. (f) Schematic illustration of the synthesis of Ti_3C_2@iCON. Reproduced with permission: Copyright 2021, Wiley [188].

prepare a morphology-controllable MXene-metal compound composite. As illustrated in Fig. 15b, 0D bimetallic MOF (CoZn-MOF) was attached to 2D Ti_3C_2 MXene via self-assembly [181]. The self-assembly occurred due to the attraction between the electropositive cobalt/zinc ions and the negatively charged MXene. Subsequently, 2-methylimidazole was introduced to form CoZn-MOFs on the surface of MXene. After further selenization, CoSe/ZnSe (CoZn-Se) was in-situ formed. At the same time, the surface of MXene was doped with nitrogen due to the pyrolysis of 2-methylimidazole. This 0D-2D heterostructure (CoZn-Se@N-MX) effectively prevented the clustering of CoZn-Se nanoparticles and avoided the restacking of MXene sheets. Furthermore, CoZn-Se@N-MX exhibited a hierarchical porous architecture, featuring a substantial active area with low Li^+ diffusion resistance. This structure could also reduce the activation energy for Li_2S deposition and dissolution. Consequently, the Li-S battery achieved a high sulfur utilization and demonstrated a high areal capacity of 6.6 mAh g^{-1} at 0.01C, even with a high sulfur loading of 7.8 mAh g^{-1} and a low electrolyte/sulfur ratio of 5 μL mg^{-1} [181].

5.4. Mxene-organic composites

Some polymers with porous structures and large surface areas have also been applied to boost MXene's performance in Li-S batteries [182]. A conjugated polymer was grafted on both sides of the delaminated $Ti_3C_2T_x$ MXene to fabricate a 2D sandwich-structured electrocatalytic sulfur host (named as CMP-M) [183]. The CMP polymer, as displayed in Fig. 15c, was synthesized from 2,4,6-tris(4-aminophenyl)-1,3,5-triazine (TAPT) and 2,7-dibromo[1]benzothieno[3,2-b]benzothiophene (DiBr-BTBT). It was chosen because triazine and benzothiophene units can capture various LiPS. In this composite, MXene facilitated rapid electron transport and accelerated the electrochemical conversions of LiPS. With CMP-M as a sulfur host material, the Li-S cell showed a high specific capacity of 1402 mAh g^{-1} at 0.1C, and an outstanding rate performance of 610 mAh g^{-1} at 4C. It is worth noting that the thick and dense polymer coating on MXene surface could restrict the exposure of active sites and hinder high sulfur loading. To tackle this problem, Mai et al. introduced in-plane mesopores within the polymer and constructed a thin 2D structured $Ti_3C_2T_x$ MXene-poly(m-phenylenediamine) (mPmPD/MXene) composite [184]. The mPmPD/MXene was synthesized by a soft-templating approach, where MXene nanosheets acted as the 2D interface, and the polymer cylindrical micelles functioned as template for creating pores (Fig. 15d). The average pore size of mPmPD/MXene was about 10 nm based on TEM images. These in-plane mesopores resulted in a specific surface area up to 138 m^2 g^{-1}, providing enough room to host sulfur, and facilitating smooth electrolyte infiltration in the cathode. In addition, the thin 2D structure of mPmPD/MXene with a uniform thickness of 21 nm (Fig. 15e) ensured rapid electron transport from inner MXene to the sulfur within the polymer. Benefiting from the above benefits, the Li-S battery utilizing mPmPD/MXene/S cathode performed a notable specific capacity of 1248 mAh g^{-1} at 0.1C and outstanding long-term cycling stability with only a 0.0593% capacity decay rate over 800 cycles at 1C.

Covalent organic frameworks (COFs) with controllable porous structures and adjustable pore size can serve as "ion-sieves", bringing tremendous advantages to block LiPS shuttling [185,186]. The possibility of precisely designing the porous structure and heteroatom composition allows COFs to have controlled chemical interactions with LiPS. However, COFs are typically electronic insulators and cannot be directly used in energy storage devices [187]. One effective solution is to form MXenes and COFs composites, which can improve the overall conductivity and prevent the restacking of MXene. For example, Li et al. reported the synthesis of a guanidinium-based ionic-covalent organic nanosheet (iCON) heterostructure (Ti_3C_2@iCON) by coating the iCON on the surface of Ti_3C_2 MXene utilizing electrostatic and hydrogen bonding interactions (Fig. 15f) [188]. As the positively charged guanidinium units in iCON immobilize the negatively charged LiPS by electrostatic attraction, the iCON can effectively suppress the shuttling effect. Based on the Li_2S nucleation experiments, the responsivity of Li_2S nucleation in Ti_3C_2@iCON is quicker than that on pristine MXene, indicating a lower Li_2S nucleation barrier on the Ti_3C_2@iCON surface. The superior catalytic effect of Ti_3C_2@iCON on LiPS was also evident in its higher Li_2S precipitation capacity. Moreover, the Ti_3C_2@iCON can facilitate the oxidation of solid Li_2S to soluble LiPS. Hence, the Ti_3C_2@iCON provided favorable bidirectional catalytic capabilities, increasing sulfur utilization and improving cycling stability. As a result,

Table 1
The comparison of electrochemical performance of MXene-based Li-S batteries.

Materials	Application	Sulfur loading mg cm^{-2}	Low-rate capacity mAh/g	High-rate capacity mAh/g	Long cycling stability(retention/cycles/current)	Ref.
Cu SA/N-$Ti_3C_2T_x$	separator	1.2–1.4	1468/0.2C	925/3C	76.8%/400/2C	[125]
SA-Zn-MXene	sulfur host	–	1136/0.2C	517/6C	88.7%/400/4C	[121]
I-MXene	separator	1	1308/0.2C	665/2C	58.2%/100/0.2C	[99]
HE-MXene/G	separator	1.2	1358.8/0.2C	1001.5/1C	68.9%/1200/2C	[72]
CNT@MXene	sulfur host	1.1–1.3	1375.1/0.1C	557.3/8C	67.1%/700/6C	[96]
MXene-TiN	sulfur host	1.0–1.2	1161.1/0.2C	593.9/5C	79.8%/1000/5C	[153]
		10.16	8.27 mAh cm^{-2}/0.2C	–	81.6%/80/0.2C	
V_2C/VO_2	sulfur host	–	1360/0.1C	656/5C	40.6%500/5C	[136]
Nb_2C/Nb_2O_5	sulfur host	1.0	1148/0.2C	700/3C	77.9%/500/1C	[141]
TiS_2/TiO_2@MXene	sulfur host	2	1227/0.1C	690/4C	82.7%/500/1C	[152]
$Ti_3C_2T_x$-CoMOF	separator	2.5	1333/0.5	654/3C	94.4%/600/2C	[190]
		7.5	1096/0.2C	–	–	
mPmPD/MXene	sulfur host	1.2	1186.5/0.2C	413.1/5C	535/800/1C	[184]
		5.9	6.8 mAh cm^{-2}/0.1C	–	94.9%/60/0.1C	
Mesoporous Carbon/ MXene	separator	–	952/0.5C	537/5C	68.7%/800/1C	[158]
		7.08	4.5 mAh cm^{-2}/0.1C	–	–	
Fe_3Se_4/FeSe@MXene	separator	1.2	1104.2/0.2C	758.8/4C	65.7%/600/2C	[191]
		5.8	862.6/0.2C	–	92.3%/120/0.2C	
MoS_2/MXene	separator	1.2–1.5	1050.7/0.2C	745.4/1C	58.7%/700/1C	[167]
ZnS/MXene	separator	0.8–1.2	1452.7/0.1C	640.9/5C	76.1%/250/1C	[192]
		5.2	1010.5/0.2C	–	73.6%/60/0.2C	
V-doped WSe_2/MXene	sulfur host	1.2	1402.5/0.1C	732.3/5C	66.3%/500/0.2C	[171]
		7	6.38mAh cm^{-2}/0.1C	–	72.4%/300/0.1C	
1 T-VSe_2-MXene	sulfur host	1.5	1321/0.1C	670/5C	67.8%/550/0.5C	[170]
		6.9	6.42mAh cm^{-2}/0.2C	–	52.3%/300/0.2C	
MXene@$CoSe_2$/NC	separator	–	1063.14/0.2C	646.12/2C	71.3%/1000/1C	[193]
		3.5	3.34mAh cm^{-2}/0.2C	–	–	
La_2O_3-MXene@CNF	sulfur host	1	1165.3/0.2C	747.7/3C	73.3%/1000/2C	[194]
		7	805.4/0.2C	–	86.7%/200/0.2C	
MXene/MoS_2/SnS@C	separator	1.0	1294.3/0.5C	693.4/4C	60.0%/1000/2C	[195]
		5.1	828.1/0.2C	–	–	
SnS_2-MXene	sulfur host	1	1188.5/0.2C	603.6/5C	82.7%/500/1C	[196]
		8.0	917.9/0.05C	–	–	
1 T-VS_2-MXene	sulfur host	1.2	1473/0.1C	517/5C	60.6%/500/1C	[169]
		9.5	7.9 mAh cm^{-2}/0.05C	–	77.0%/50/0.05C	
Ti_3C_2/CoP	separator	1.5	1349.8/0.2C	535.4/5C	54.1%/1150/1C	[173]
		5.3	7.8 mAh cm^{-2}/0.02C	–	56.4%/120/0.1C	
CeO_2/MXene	sulfur host	0.58	1051.1/0.5C	610.3/4C	87.7%/200	[197]
MnO_x/MXene	sulfur host	~1	–/3C	697.8/5C	72.6%/1000	[198]
Co_2B@MXene	separator	–	1577/0.1C	597/5C	83.9%/2000/2C	[174]
		5.1	5.2 mAh cm^{-2}/0.2C	–	78.8%/100/0.2C	
MXene/MoS_2	separator	2	1336/0.1C	652/3C	75.6%/500/1C	[199]
		5	–	1101/1C	63.6%/200/1C	
SiO_2@MXene	sulfur host	~1.2	1263.0/0.2C	829.3/2C	67.0%/1000/1C	[200]
		3.6	1083.4/0.2C	–	73.1%/100/0.2C	
Co_3Se_4@N-C/$Ti_3C_2T_x$	separator	–	1448/0.2C	787/4C	–	[201]
		2.24	1058/0.2C	–	–	
MXene@WS_2	separator	1	1613.7/0.1C	622.2/3C	56.4%/2C/2000	[202]
		6.3	1034.3/0.3C	–	60.0%/0.3C/240	
1 T-$MoSe_2$/MXene	sulfur host	1.0	1307/0.1C	726.3/5C	64.2%/500/0.2C	[203]
		6.5	6.9 mAh cm^{-2}/0.1C	–	73.1%/200/0.1C	
MXene/SnO_2QDs	sulfur host	–	1147.6/0.1C	515.7/2C	62.1%/900/1C	[204]
$VS_4/Ti_3C_2T_x$	separator	1.2	1214/0.2C	673/4C	71%/500/1C	[205]
$Ti_3C_2T_x$@$CoSe_2$	separator	1.2	1183/0.1C	713/3C	54.2%/800/0.5C	[206]
		4	4.27 mAh cm^{-2}/0.2C	–	78.9%/60/0.2C	
Co-$MoSe_2/Ti_3C_2T_x$	sulfur host	1.5	1454/0.1C	759/5C	52.4%/500/0.5C	[207]
		13.5	8.2 mAh cm^{-2}/0.1C	–	65.9%/200/0.1C	
CoTe-MXene	separator	1	1664/0.1C	905/3C	–	[208]
		5.6	7.2 mAh cm^{-2}/0.02C	–	55.6%/50/0.02C	
MCCoS	separator	1.2–1.5	1340.7/0.1C	368.6/20C	71.9%/1000/7C	[168]
GO@MX@VS_4	sulfur host	1.6–1.9	1443.9/0.1C	371.3/5C	79.6%/1200/5C	[209]
		7.39	6.9mAh cm^{-2}/0.05C	–	–	

by coating Ti_3C_2@iCON on a commercial separator, the Li-S cell delivered a remarkable initial capacity of 1186 mAh g^{-1}, corresponding to an areal capacity of 9.01 mAh cm^{-2} or volumetric capacity of 1201 mAh cm^{-3} at 0.1C. Notably, the capacity remained as high as 1092 mAh g^{-1}, 8.29 mAh cm^{-2}, and 1105 mAh cm^{-3} after 200 cycles. Yang et al. reported another COF-MXene-based heterostructure (CTF/TNS) of the 2D covalent triazine framework on $Ti_3C_2T_x$ MXene nanoflakes [189]. The lithiophilic N sites in COF and the sulfurophilic Ti sites on MXene facilitated dual-site chemical adsorption to LiPS, suppressing the shuttle effect effectively. Additionally, the integrity of organic COF with ordered pores and inorganic MXene with high conductivity provided 3D spatial confinement for sulfur and facilitated rapid electron/ion transfer for high reaction kinetics.

Different modification strategies are applied in Li-S batteries, enhancing the battery performance, as shown in Table 1.

6. Applications of MXene in other metal-sulfur batteries

Although Li-S batteries possess the highest theoretical gravimetric energy density (~2672 Wh kg^{-1}) among all metal-sulfur batteries, other nonlithium metal anodes including Na, K, Ca, Mg, and Al, which are more abundant and less expensive than Li, have been considered promising alternatives to the Li anode. In addition, several multivalent metal sulfur batteries, such as Mg-S (3221 Wh L^{-1}), Al-S (2981 Wh L^{-1}), and Ca-S (3202 Wh L^{-1}) batteries, deliver higher volumetric energy density than Li-S batteries (2955 Wh L^{-1}) [7]. Despite these advantages, nonlithium metal-sulfur batteries face significant challenges that currently hinder their practical application. Similar to Li-S batteries, the performance of nonlithium metal-sulfur batteries is challenged by the polysulfides shuttle effect and sluggish polysulfides conversion kinetics. Meanwhile, other problems arise with different metal anodes, such as metal corrosion issues, distinct reaction pathways, and kinetic limitations due to variations in ion sizes and valences [210]. This section describes the application of MXene and MXene-based materials in nonlithium metal-sulfur batteries, with a focus on material design strategies tailored to different types of metal-sulfur batteries.

6.1. Sodium and potassium sulfur batteries

The most common issue for all alkali metal-sulfur batteries is the large solubility of polysulfides in commercial ether-based electrolytes, resulting in rapid capacity degradation due to the shuttle effect. Compared to LiPS, the solubility of sodium polysulfides (NaPS) and potassium polysulfides (KPS) is higher, exacerbating the shuttle effect [211,212]. Moreover, the reaction processes of the S cathodes are also different. For Na-S batteries, Na_2S_2 is commonly identified as one of the discharge products based on XPS, Raman, and DFT calculations [7,211,213]. Meanwhile, in a K-S battery, the discharge product is most probably K_2S_3 at room temperature, because the thermodynamic stability of K_2S_3 ($\Delta G = -528$ kJ mol^{-1}, Gibbs energy of formation at 25 °C) is higher than that of K_2S ($\Delta G = -410$ kJ mol^{-1}) [7,214]. The reaction barrier of the sulfur species is more significant in Na-S and K-S batteries, resulting in slower reaction kinetics. Hence, the modification of MXene should focus not only on enhancing the adsorption ability to polysulfides but also on improving its catalytic performance to accelerate the electrochemical reaction kinetics, which aims to increase the actual energy density of Na/K-S batteries.

Since the relatively similar electrochemistry of Na-S and Li-S batteries, the strategies applied in Li-S batteries may also benefit the design of Na-S batteries. Heteroatom-doping into MXene proves to be an effective approach for improving the performance of Na-S batteries. Wang et al. synthesized porous nitrogen-doped $Ti_3C_2T_x$ MXene@multiwalled CNT microspheres (N-MXene@MWCNT-MP) by a facile spray drying and annealing method (Fig. 16a) [215]. XPS measurements revealed the coexistence of pyridinic N (32.18 at%), Ti-N metal bonds (23.68 at%), pyrrolic N (27.12 at%), and graphic N (17.02 at%) on the N-doped

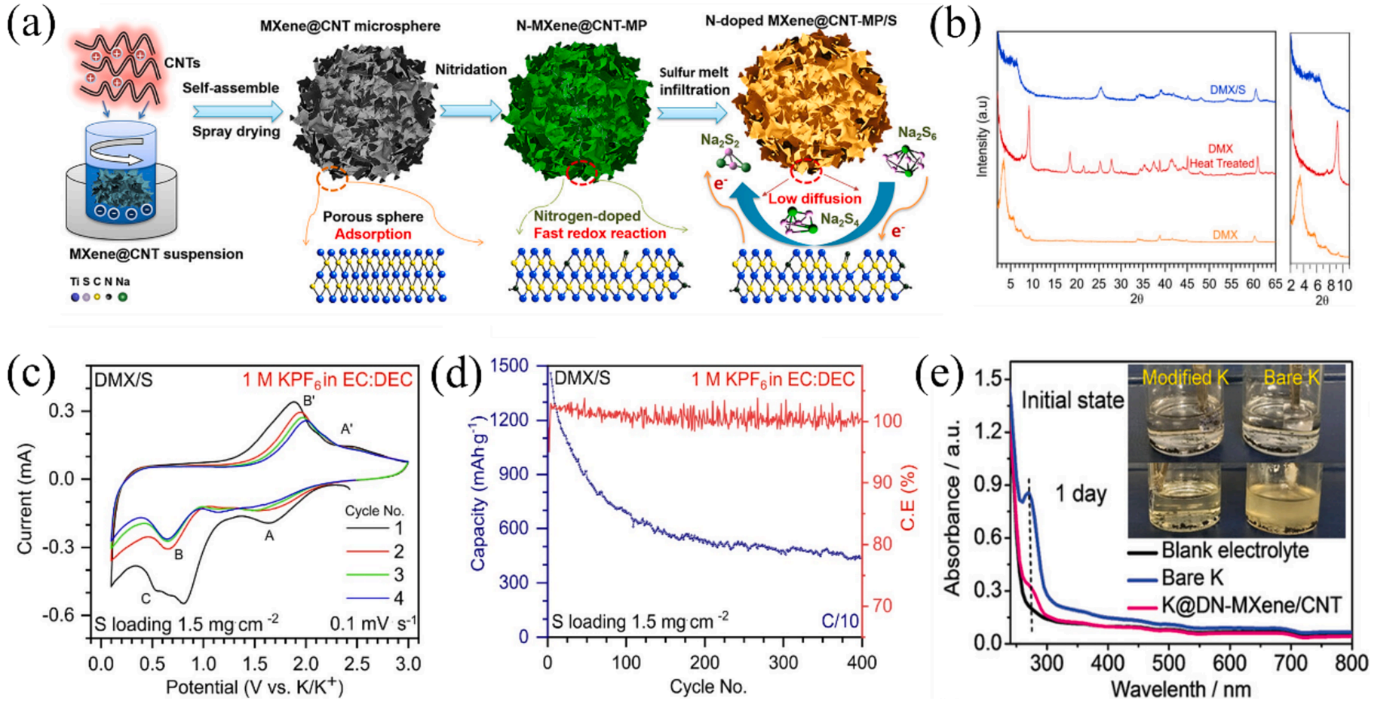

Fig. 16. (a) Schematic preparation procedure of porous N-MXene@MWCNT-MP/S microspheres. Reproduced with permission: Copyright 2021, American Chemical Society [215]. (b) XRD patterns of DMX (orange, bottom), DMX/S after heat treatment (red, middle), and DMX/S (blue, top) powders. (c) CV curves of DMX/S. (d) Cycling stability of DMX/S cathode. Reproduced with permission: Copyright 2022, Elsevier [221]. (e) Digital images (shown in inset) and the corresponding UV–vis spectra of liquid electrolytes in optically transparent devices assembled with K@DN-MXene/CNT anode (or bare K foil) and SPAN powder immersed in liquid electrolytes. Reproduced with permission: Copyright 2019, Wiley [222]. (For interpretation of the references to color in this figure legend, the reader is referred to the web version of this article.)

$Ti_3C_2T_x$. The pyrrolic N and pyridinic N exhibited strong affinity and high binding energy with NaPS due to the Lewis acid-base interaction. Additionally, the introduction of carbon nanotubes prevented the restacking of MXene, thereby enabling high utilization of the N-doped MXene surface. The structure of the microspheres also provided a uniformly porous and highly conductive network that allowed for high sulfur loading and facilitated electron migration. As a result, the N-MXene@MWCNT-MP/S cathode with a high sulfur loading of 5.5 mg cm^{-2}could deliver a high initial specific capacity of 821.7 mAh g^{-1} and maintained 70.28% after 500 cycles at 2C. Another study reported that the sulfur-doped $Ti_3C_2T_x$ MXene (S-$Ti_3C_2T_x$) enhanced affinity to NaPS. This enabled the S-$Ti_3C_2T_x$/S cathode to achieve high cycling performance, maintaining a reversible capacity of 577 mAh g^{-1} after 500 cycles with a high areal sulfur loading of 4.5 mg cm^{-2} [211].

In addition to anion doping, the effect of transition metal doping on the performance of Na-S batteries was also investigated [216]. DFT simulations were conducted on various transition metal (Fe/Co/Ni/Cu) atoms attached to Ti_2CS_2 (TM@Ti_2CS_2), in order to reveal the correlation between metal anchoring and sulfur host performance. The results indicated that single-atom metal doping can enhance the chemical interaction between MXene and NaPS because of the formation of TM-S and Na-S bonds. Additionally, metal doping makes the reduction of NaPS easier to occur on the surface of TM@Ti_2CS_2. In the reverse electrochemical direction, the dissociation barrier of Na_2S is also smaller after metal doping. Hence, in theory, single-atom metal doping has a bidirectional catalytic effect on Na-S batteries.

Similar to Li-S batteries, MXene-based composites have also been prepared to enhance the performance of Na-S batteries. For instance, cobalt nanoparticles were introduced to enhance the catalytic ability of NaPS conversion, and the strong adsorption ability of TiO_2 [217] and Ni$(OH)_2$ [218] was utilized to suppress the shuttle effect. Additionally, composites such as hierarchical hybrid MXenes [219] and MXene@C [220] were applied as separator modifiers to block the NaPS shuttling, thereby improving the cycling stability of Na-S batteries.

To date, only limited works have reported the application of MXene in K-S batteries. Kalra et al. prepared multi-layer $Ti_3C_2T_x$ MXene, enlarged its interlayer spacing via benzyl methyl ammonium chloride (DHT) treatment, and then introduced sulfur by heat treatment [221]. The resulting material (DMX/S) showed enlarged d-spacing after the heat treatment based on XRD measurements, indicating that amorphous sulfur was loaded between its interlayer space (Fig. 16b). When DMX/S was employed as the cathode for a K-S battery, a low cutoff voltage (0.1 V) was required to complete the reduction reaction due to its sluggish kinetics compared to Li-S and Na-S systems (Fig. 16c). Meanwhile, rapid capacity decay was observed at 0.2C due to the severe shuttle effect of KPS (Fig. 16d). This rapid capacity decay was also partially attributed to the destruction of large-sized K^+ (0.276 nm) ions to the SEI layer. To boost the performance of K-S batteries, Tang et al. prepared a titanium-vacancy nitrogen-doped MXene/carbon nanotube freestanding framework (DN-MXene/CNT) and used it as a host for K metal [222]. When immersing the K-based anodes in KPF_6-based electrolytes containing the same amount of sulfur-poly(acrylonitrile) (SPAN) powder, the sample without DN-MXene/CNT turned yellow after aging for 24 h (Fig. 16e). According to UV–Vis spectroscopy, a strong peak located at 220–260 nm was observed, confirming the dissolution of KPS in the electrolyte. The electrolyte with K@DN-MXene/CNT showed a much lighter color, indicating stronger adsorption to KPS and demonstrating its potential to suppress the KPS shuttle effect.

6.2. *Multivalent metal-sulfur batteries*

For multivalent metal-sulfur batteries, including Mg-S, Ca-S, Zn-S, and Al-S batteries, the shuttle effect still exists but is not as severe as for alkali metal-sulfur batteries. The solubility of multivalent metal polysulfides (e.g., MgS_x, CaS_x, and AlS_x) in commonly used ether-based electrolytes is also much lower than that of alkali metal polysulfides [7]. What is different for Zn-S batteries is the commonly utilized aqueous zinc-based solutions [223]. At room temperature, it is thermodynamically more favorable to form $Zn(OH)_4^{2-}$ or $Zn(OH)_2$ ($\Delta G = -156.3$ kJ/mol) rather than ZnS ($\Delta G = -201.3$ kJ/mol), which makes the key challenge for Zn-S batteries is the occurrence of hydrogen evolution reaction (HER). The aqueous electrolytes for Zn-S batteries also affect the electrochemical mechanism of sulfur cathode, as the dissolution of sulfur in aqueous media gives rise to the formation of various species such as HS^-, H_2S, S^{2-}, and S_x^{2-} ($x = 2$–5) [224]. However, the reaction rates of all mentioned multivalent metal-sulfur batteries are much lower compared to alkali metal-sulfur battereis, especially for the oxidation reaction of the discharge products (MgS, CaS, ZnS, and Al_2S_3). These inactive sulfur species accumulate on the cathode due to the large kinetic barrier, leading to cathode passivation and rapid deterioration of battery performance. Therefore, the MXene design strategy for high-performance multivalent sulfur batteries should focus on improving the kinetics.

Compared with carbon, $Ti_3C_2T_x$ MXene has been proved to provide a better conducting environment and Zn ion transport flux, which leads to enhanced Zn ion storage in a flexible S@$Ti_3C_2T_x$ cathode [225]. Paired with Zn metal anode and iodine-added amphiphilic gel electrolyte, the Zn-S battery delivered a high Zn ion storage ability of 772.7 mAh g^{-1} at 300 mA g^{-1}. Yu et al. synthesized a 3D $Ti_3C_2T_x$/rGO composite with in-situ formed TiO_2 nanoparticles attached to MXene (s-MXTO@rGO) and used it in hybrid Li/Mg-S batteries with Li^+ and Mg^{2+} as charge carriers [160]. The synergistic effects between TiO_2-decorated MXene and rGo are summarized in Fig. 17a. Compared with pure MXene, TiO_2 nanoparticles showed a higher adsorption capability towards MgS_x/LiPS, effectively suppressing the shuttle effect. Moreover, DFT simulations indicated that TiO_2 can disperse the positive charge of Mg^{2+} by establishing Mg-O bonds. The strong Mg-O bonds can lower the energy to break Mg-S bonds, accelerating the decomposition of MgS_2 to MgS. Based on this mechanism, TiO_2 nanoparticles on MXene functioned as both adsorptive and catalytic sites for polysulfides to alleviate the shuttle effect and improve the electrochemical reaction kinetics. Meanwhile, MXene flakes with strong mechanical strength can support the porous structure and accommodate the volume expansion during battery cycling. Furthermore, rGO layer can provide smoother Mg^{2+} diffusion for high-rate operations as the migration barrier of Mg^{2+} was computed as 75 eV for MXene and 6.6 eV for rGO. As a result, the s-MXTO@rGO-S cathode achieved a high initial discharge capacity of 1735.7 mAh g^{-1} at 0.2C and an outstanding rate capability of 299.2 mAh g^{-1} 5C. For long cycling tests at 2C, a remarkable capacity of 445.6 mAh g^{-1} was retained after 1000 cycles with a very low decay rate of 0.016%. Other transition metal compound decorated MXenes, such as Ti_3C_2@CoO [226], and Co_3S_4@MXene [227], exhibited a similar function to TiO_2-decorated MXene and enhanced the performance of Mg-S batteries when used as S hosts.

In Al-S batteries, the decomposition barrier for Al_2S_3 is significant, requiring a high energy of 332 kJ mol^{-1} to break one Al-S bond. In comparison, the energy required for each Li-S bond is 312.5 kJ mol^{-1} [228]. A binder-free S@$Ti_3C_2T_x$ film with sulfur nanoparticles homogeneously anchored on the MXene flakes was tested as S hosts in Al-S batteries [229]. MXene exhibited advantageous properties compared to graphene, including higher electronic conductivity and higher binding energies to S_8 and Al_2S_n. Consequently, the free-standing S@$Ti_3C_2T_x$ film exhibited the first discharge capacity of 489 mAh g^{-1} at 300 mA g^{-1} and maintained 415 mAh g^{-1} after 280 cycles with an average Coulombic efficiency of ~95%. In another work, DFT simulation was employed to reveal the effect of single-atom metal doping on the performance of $Ti_3C_2O_2$ MXene-based (SA@MXene) Al-S battery [230]. Binding energies of 20 kinds SA@MXene with several possible Al_2S_n species and S_8 (e.g., S_8*, Al_2S_{18}*, Al_2S_{12}*, Al_2S_6*, and Al_2S_3*) were summarized in Fig. 17b. Among all SA@MXenes, Sc, Pt, V, Cr, Mn, Y, Zr, Nb, Mo, Tc, Ru, Rh, and Pd@$Ti_3C_2O_2$ showed higher binding energies, which indicated stronger adsorption to AlPS and better ability to

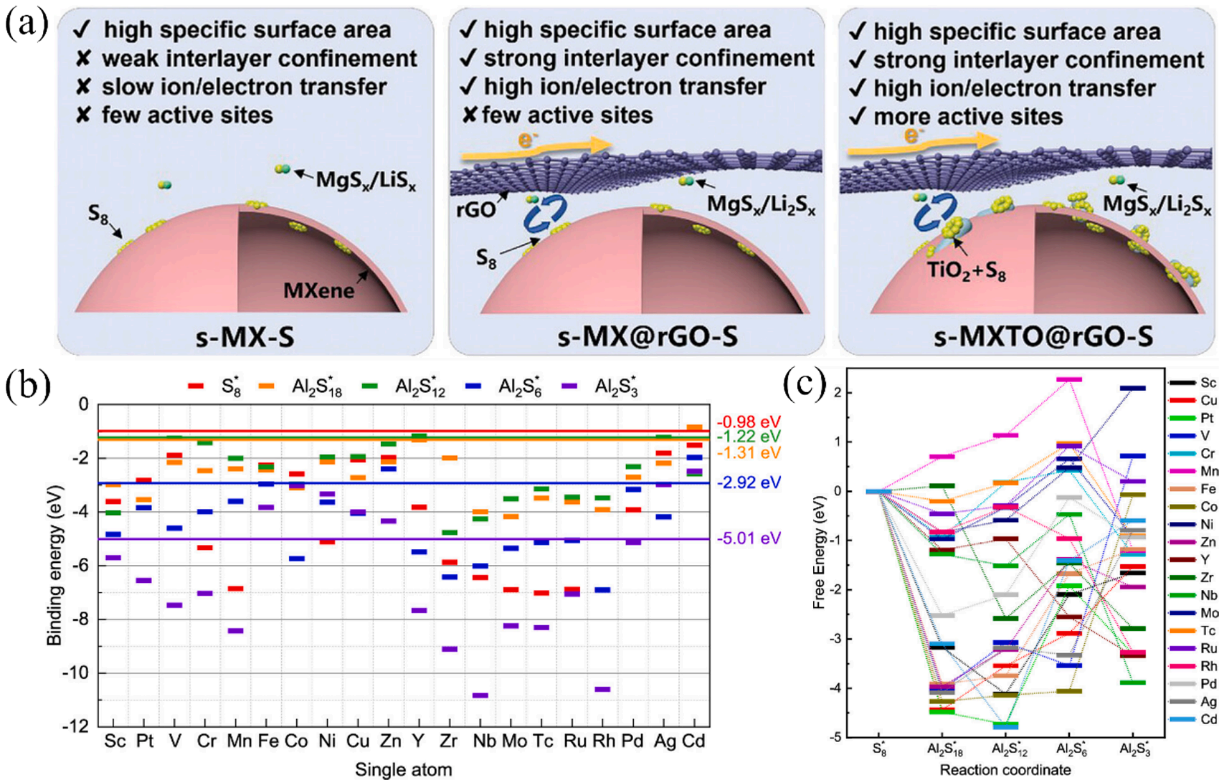

Fig. 17. (a) Schematic diagram of performance improvement mechanism of the s-MX, s-MX@rGO, and s-MXTO@rGO-S electrodes for MLSBs. Reproduced with permission: Copyright 2023, Wiley [160]. (b) Binding energy (E_b) values of S_8 and Al_2S_n species on SA@$Ti_3C_2O_2$ nanosheets, where the E_b values of S_8*, Al_2S_{18}*, Al_2S_{12}*, Al_2S_6*, and Al_2S_3* are shown as short red, orange, green, blue, and purple lines. The colored solid lines represent the binding energies of $Ti_3C_2O_2$ and S_8/Al_2S_n species. (c) Relative Gibbs free energy for the S_8 and Al_2S_n species on SA@$Ti_3C_2O_2$ nanosheets. The complete reaction paths of S_8 and Al_2S_n species are S_8* → Al_2S_{18}* → Al_2S_{12}* → Al_2S_6* → Al_2S_3*. Reproduced with permission: Copyright 2022, American Chemical Society [230]. (For interpretation of the references to color in this figure legend, the reader is referred to the web version of this article.)

suppress the shuttle effect. To investigate the catalytic ability of SA@MXene for AlPS conversion, the authors calculated the Gibbs free energy of the complete reaction pathway from S_8 to Al_2S_n (S_8* → Al_2S_{18}* → Al_2S_{12}* → Al_2S_6* → Al_2S_3*) (Fig. 17c). The highest relative free energy (E_a) is used to determine the rate-limiting step among all steps. Compared to pure $Ti_3C_2O_2$ nanosheets (1.12 eV), Y, Rh, Tc, Mo, and Nb@$Ti_3C_2O_2$ exhibited lower E_a values of 0.23, 0.51, 0.80, 0.99, and 1.05 eV, respectively. These SA@MXenes are expected to demonstrate lower overpotential for AlPS conversion and better catalytic ability compared to pure MXene nanosheets. Taking all factors into consideration, Y, Nb, Mo, and Tc@$Ti_3C_2O_2$ should be the most promising candidates to improve the performance of Al-S batteries.

The electrochemical performance of MXene-based nonlithium metal-sulfur batteries is summarized in Table 2.

7. Summary and perspectives

This work summarizes the design and modification strategies of MXenes and their roles in enhancing the performance of Li-S and other metal-sulfur batteries. The principles guiding the selection and modification of MXene should focus on leveraging their unique properties to effectively address the critical challenges faced by sulfur-based batteries. By tailoring their composition, structure, and surface chemistry, MXene can offer the following benefits: (a) Their metallic conductivity facilitates rapid electron transfer, reducing cathode polarization and enabling high-rate performance, which also improves sulfur utilization

Table 2
The comparison of electrochemical performance of MXene-based nonlithium metal-sulfur batteries.

Type	Materials	Application	Sulfur loading mg cm^{-2}	Initial Capacity mAh/g/Current	Cycle number /Retention	Ref.
Na-S	$Ti_3C_2T_x$/Ni(OH)$_2$/C	sulfur host	1.3–1.5	2399.4/0.22C	100/1175.3	[218]
Na-S	S-$Ti_3C_2T_x$	sulfur host	2.1	970/0.5C	200/690.3	[211]
Na-S	$Ti_3C_2T_x$/$Mo_2Ti_2C_3T_x$	separator	1.0	992/0.1C	100/620	[219]
Na-S	TiO_2-Ti_3C_2	sulfur host	–	1032.2/0.1C	100/435.76	[217]
Na-S	$Ti_3C_2T_x$/RGo/Co	sulfur host	–	683/0.5C	200/360	[231]
Na-S	N-$Ti_3C_2T_x$@MWCNT	sulfur host	2.0	980/1C	500/676.3	[215]
Na-S	MXene@C/Polyolefin/MXene@C	separator	1.5	1159/0.2C	50/1011	[220]
K-S	$Ti_3C_2T_x$	sulfur host	–	~1700/0.05C	300/450	[221]
Zn-S	$Ti_3C_2T_x$	sulfur host	0.8–1.0	772.7/300 mA g^{-1}	–	[225]
Mg-S	Ti_3C_2@CoO	sulfur host	0.5–0.7	–/100 mA g^{-1}	70/540	[226]
Mg-S	MXene-TiO_2/rGO	sulfur host	~0.5	1057.8/0.2C	100/1052.0	[160]
Mg-S	Co_3S_4@MXene	sulfur host	1.5	1220/0.1C	100/528	[227]
Al-S	$Ti_3C_2T_x$	sulfur host	0.54–0.65	489/300 mA g^{-1}	280/415	[229]

and energy density. (b) The surface chemistry of MXenes influences their interaction with polysulfides, enhancing their affinity toward polysulfides and mitigating the shuttle effect. Moreover, certain surface groups can catalytically promote the conversion of sulfur species. (c) The ultrathin layered structure of MXenes provides a large surface area and abundant active sites to interact with sulfur and polysulfides. (d) The negatively charged surface of MXene enables good dispersion in solvents, which facilitates to fabricate diverse morphologies, such as hierarchical structures and 3D conductive networks, offer efficient ion transport pathways and address the volume expansion of cathode during cycling. (e) With over 50 synthesized variants, MXenes offer a wide selection for specific applications. (f) The high mechanical strength of MXenes allows the fabrication of free-standing electrodes, expanding their use in flexible wearable electronics.

Several perspectives for the future development of MXenes in sulfur-based batteries are proposed: (a) Further research into the catalytic effects of MXenes is needed. The catalytic activity can enhance sulfur electrochemical reaction kinetics, but the instability of MXenes complicates this research. More in-situ measurements, such as XRD, Raman, and XPS, are expected to monitor dynamic changes during electrochemical reactions. Post-cycling analysis can also reveal changes in surface chemistry. (b) Anode-free sulfur-based batteries offer a promising direction. In Li-S batteries, excess lithium metal is often used, leading to lithium wastage and low energy density. MXene-Li_2S batteries could eliminate the need for additional cations, with MXenes serving as both the sulfur host and lithium deposition site, significantly improving energy density. (c) MXenes should be explored in solid-state sulfur-based batteries. The shuttle effect in liquid electrolytes can be completely avoided by using solid-state electrolytes, though sulfur conversion remains a challenge due to poor charge transfer. Leveraging MXenes' conductivity could accelerate sulfur conversion, enhancing solid-state battery performance while addressing dendrite formation issues, improving both safety and energy density. (d) Improving MXene stability is crucial. Their vulnerability to oxidation under harsh battery conditions limits their potential in practical application. Developing strategies to stabilize MXenes and prevent degradation during cycling is essential for ensuring the long-term performance of sulfur-based batteries. (e) Investigating MXenes beyond $Ti_3C_2T_x$ is also important. Although $Ti_3C_2T_x$ dominate the recent research due to its high stability and conductivity, exploring other compositions or surface groups could yield materials with superior catalytic and adsorptive properties. (f) Finally, evaluating MXene-based sulfur batteries under realistic conditions is essential. Despite significant progress, few studies have tested MXene-based Li-S batteries at the Ah level. Systematic studies using Ah-level pouch cells and commercial-grade electrodes are needed to assess factors like sulfur loading, electrolyte volume, and cycling stability under practical conditions.

CRediT authorship contribution statement

Hao Wang: Writing – original draft, Software, Resources, Funding acquisition, Formal analysis, Data curation. **Albert de Kogel:** Writing – original draft, Resources. **Zerui Wang:** Resources. **Rujia Zou:** Validation, Supervision. **Xuehang Wang:** Writing – review & editing, Project administration, Funding acquisition.

Declaration of competing interest

The authors declare that they have no known competing financial interests or personal relationships that could have appeared to influence the work reported in this paper.

Acknowledgments

The author Hao Wang is grateful for the scholarship from the China Scholarship Council (202206630042) and the Graduate Student Innovation Fund of Donghua University (CUSF-DH-D-2022007).

Data availability

Data will be made available on request.

References

[1] Z.P. Cano, D. Banham, S.Y. Ye, A. Hintennach, J. Lu, M. Fowler, Z.W. Chen, Batteries and fuel cells for emerging electric vehicle markets, Nat. Energy 3 (2018) 279–289.

[2] Y.J. Liu, X.Y. Tao, Y. Wang, C. Jiang, C. Ma, O.W. Sheng, G.X. Lu, X.W. Lou, Self-assembled monolayers direct a LiF-rich interphase toward long-life lithium metal batteries, Science 375 (2022) 739–745.

[3] Y.S. Tian, G.B. Zeng, A. Rutt, T. Shi, H. Kim, J.Y. Wang, J. Koettgen, Y.Z. Sun, B. Ouyang, T.N. Chen, Z.Y. Lun, Z.Q. Rong, K. Persson, G. Ceder, Promises and challenges of next-generation "beyond Li-ion" batteries for electric vehicles and grid decarbonization, Chem. Rev. 121 (2021) 1623–1669.

[4] E.S. Fan, L. Li, Z.P. Wang, J. Lin, Y.X. Huang, Y. Yao, R.J. Chen, F. Wu, Sustainable recycling technology for Li-ion batteries and beyond: Challenges and future prospects, Chem. Rev. 120 (2020) 7020–7063.

[5] J.P. Pender, G. Jha, D.H. Youn, J.M. Ziegler, I. Andoni, E.J. Choi, A. Heller, B. S. Dunn, P.S. Weiss, R.M. Penner, C.B. Mullins, Electrode degradation in lithium-ion batteries, ACS Nano 14 (2020) 1243–1295.

[6] G. Zhou, H. Chen, Y. Cui, Formulating energy density for designing practical lithium-sulfur batteries, Nat. Energy 7 (2022) 312–319.

[7] H.L. Ye, Y.G. Li, Room-temperature metal-sulfur batteries: What can we learn from lithium-sulfur? InfoMat 4 (2022) e12291.

[8] Y. Chen, T.Y. Wang, H.J. Tian, D.W. Su, Q. Zhang, G.X. Wang, Advances in lithium-sulfur batteries: From academic research to commercial viability, Adv. Mater. 33 (2021) 2003666.

[9] Y. Gong, J. Li, K. Yang, S.Y. Li, M. Xu, G.P. Zhang, Y. Shi, Q. Cai, H.X. Li, Y. L. Zhao, Towards practical application of Li-S battery with high sulfur loading and lean electrolyte: Will carbon-based hosts win this race? Nano-Micro Lett. 15 (2023) 150.

[10] X.Q. Qi, F.Y. Yang, P.F. Sang, Z.L. Zhu, X.Y. Jin, Y.J. Pan, J. Ji, R.N. Jiang, H. R. Du, Y.S. Ji, Y.Z. Fu, L. Qie, Y.H. Huang, Electrochemical reactivation of dead Li_2S for Li-S batteries in non-solvating electrolytes, Angew. Chem. Int. Ed. 62 (2023) e202218803.

[11] D.S. Wu, F.F. Shi, G.M. Zhou, C.X. Zu, C. Liu, K. Liu, Y.Y. Liu, J.Y. Wang, Y. C. Peng, Y. Cui, Quantitative investigation of polysulfide adsorption capability of candidate materials for Li-S batteries, Energy Storage Mater. 13 (2018) 241–246.

[12] C. Yuan, X.C. Song, P. Zeng, G.L. Liu, S.H. Zhou, G. Zhao, H.T. Li, T.R. Yan, J. Mao, H. Yang, T. Cheng, J.P. Wu, L. Zhang, Precisely optimizing polysulfides adsorption and conversion by local coordination engineering for high-performance Li-S batteries, Nano Energy 110 (2023) 108353.

[13] Z.Y. Han, R.H. Gao, Y.Y. Jia, M.T. Zhang, Z.J. Lao, B.A. Chen, Q. Zhang, C. Li, W. Lv, G.M. Zhou, Catalytic effect in Li-S batteries: From band theory to practical application, Mater. Today 57 (2022) 84–120.

[14] W.Y. Zhang, D.H. Hong, Z. Su, S. Yi, L.Y. Tian, B. Niu, Y.Y. Zhang, D.H. Long, Tailored ZnS-ZnO heterostructure enables a rational balancing of strong adsorption and high catalytic activity of polysulfides for Li-S batteries, Energy Storage Mater. 53 (2022) 404–414.

[15] T. Huang, Y.J. Sun, J.H. Wu, Z.X. Shi, Y.F. Ding, M.L. Wang, C.L. Su, Y.Y. Li, J. Y. Sun, Altering local chemistry of single-atom coordination boosts bidirectional polysulfide conversion of Li-S batteries, Adv. Funct. Mater. 32 (2022) 2203902.

[16] W.L. Li, K. Chen, Q.C. Xu, X.Y. Li, Q. Zhang, J. Weng, J. Xu, Mo_2C/C hierarchical double-shelled hollow spheres as sulfur host for advanced Li-S batteries, Angew. Chem. Int. Ed. 60 (2021) 21512–21520.

[17] X.L. Ji, K.T. Lee, L.F. Nazar, A highly ordered nanostructured carbon-sulphur cathode for lithium-sulphur batteries, Nat. Mater. 8 (2009) 500–506.

[18] J.C. Guo, Y.H. Xu, C.S. Wang, Sulfur-impregnated disordered carbon nanotubes cathode for lithium-sulfur batteries, Nano Lett. 11 (2011) 4288–4294.

[19] K. Shen, H.L. Mei, B. Li, J.W. Ding, S.B. Yang, 3D printing sulfur copolymer-graphene architectures for Li-S batteries, Adv. Energy Mater. 8 (2018) 1701527.

[20] G.M. Liang, J.X. Wu, X.Y. Qin, M. Liu, Q. Li, Y.B. He, J.K. Kim, B.H. Li, F.Y. Kang, Ultrafine TiO_2 decorated carbon nanofibers as multifunctional interlayer for high-performance lithium-sulfur battery, ACS Appl. Mater. Interfaces 8 (2016) 23105–23113.

[21] Z.A. Ghazi, X. He, A.M. Khattak, N.A. Khan, B. Liang, A. Iqbal, J.X. Wang, H. S. Sin, L.S. Li, Z.Y. Tang, MoS_2/celgard separator as efficient polysulfide barrier for long-life lithium-sulfur batteries, Adv. Mater. 29 (2017) 1606817.

[22] Z.H. Shen, X. Jin, J.M. Tian, M. Li, Y.F. Yuan, S. Zhang, S.S. Fang, X. Fan, W. G. Xu, H. Lu, J. Lu, H.G. Zhang, Cation-doped ZnS catalysts for polysulfide conversion in lithium-sulfur batteries, Nat. Catal. 5 (2022) 555–563.

[23] R. Wang, J.L. Yang, X. Chen, Y. Zhao, W.G. Zhao, G.Y. Qian, S.N. Li, Y.G. Xiao, H. Chen, Y.S. Ye, G.M. Zhou, F. Pan, Highly dispersed cobalt clusters in nitrogen-doped porous carbon enable multiple effects for high-performance Li-S battery, Adv. Energy Mater. 10 (2020) 1903550.

[24] L. Wang, Z.Y. Wang, J.F. Wu, G.R. Li, S. Liu, X.P. Gao, To effectively drive the conversion of sulfur with electroactive niobium tungsten oxide microspheres for lithium-sulfur battery, Nano Energy 77 (2020) 105173.

[25] T. Zhou, W. Lv, J. Li, G. Zhou, Y. Zhao, S. Fan, B. Liu, B. Li, F. Kang, Q.H. Yang, Twinborn TiO_2-TiN heterostructures enabling smooth trapping-diffusion-

conversion of polysulfides towards ultralong life lithium-sulfur batteries, Energy Environ. Sci. 10 (2017) 1694–1703.

[26] M. Naguib, M. Kurtoglu, V. Presser, J. Lu, J. Niu, M. Heon, L. Hultman, Y. Gogotsi, M.W. Barsoum, Two-dimensional nanocrystals produced by exfoliation of Ti_3AlC_2, Adv. Mater. 23 (2011) 4248–4253.

[27] X. Wang, L. Bannenberg, Design and characterization of 2D MXene-based electrode with high-rate capability, MRS Bull. 46 (2021) 755–766.

[28] K. Li, M. Liang, H. Wang, X. Wang, Y. Huang, J. Coelho, S. Pinilla, Y. Zhang, F. Qi, V. Nicolosi, Y. Xu, 3D MXene architectures for efficient energy storage and conversion, Adv. Funct. Mater. 30 (2020) 2000842.

[29] X.L. Li, Z.D. Huang, C.E. Shuck, G.J. Liang, Y. Gogotsi, C.Y. Zhi, MXene chemistry, electrochemistry and energy storage applications, Nat. Rev. Chem. 6 (2022) 389–404.

[30] M. Khazaei, M. Arai, T. Sasaki, C.Y. Chung, N.S. Venkataramanan, M. Estili, Y. Sakka, Y. Kawazoe, Novel electronic and magnetic properties of two-dimensional transition metal carbides and nitrides, Adv. Funct. Mater. 23 (2013) 2185–2192.

[31] N. Zhang, Y. Hong, S. Yazdanparast, M.A. Zaeem, Superior structural, elastic and electronic properties of 2D titanium nitride MXenes over carbide MXenes: A comprehensive first principles study, 2D Mater. 5 (2018) 045004.

[32] E.S. Sim, G.S. Yi, M.Y. Je, Y.B. Lee, Y.C. Chung, Understanding the anchoring behavior of titanium carbide-based MXenes depending on the functional group in Li-S batteries: A density functional theory study, J. Power Sources 342 (2017) 64–69.

[33] Z.T. Wu, T.X. Shang, Y.Q. Deng, Y. Tao, Q.H. Yang, The assembly of MXenes from 2D to 3D, Adv. Sci. 7 (2020) 1903077.

[34] Y. Gogotsi, Q. Huang, MXenes: Two-dimensional building blocks for future materials and devices, ACS Nano 15 (2021) 5775–5780.

[35] J.L. Qin, R. Wang, P. Xiao, D.L. Wang, Engineering cooperative catalysis in Li-S batteries, Adv. Energy Mater. 13 (2023) 2007509.

[36] X. Liang, A. Garsuch, L.F. Nazar, Sulfur cathodes based on conductive MXene nanosheets for high-performance lithium-sulfur batteries, Angew. Chem. Int. Ed. 54 (2015) 3907–3911.

[37] Y.Z. Wang, T.C. Guo, E. Alhajji, Z.N. Tian, Z.X. Shi, Y.Z. Zhang, H.N. Alshareef, MXenes for sulfur-based batteries, Adv. Energy Mater. 13 (2022) 2202860.

[38] A.M. Liu, X.Y. Liang, X.F. Ren, W.X. Guan, T.L. Ma, Recent progress in MXene-based materials for metal-sulfur and metal-air batteries: Potential high-performance electrodes, Electrochem. Energy Rev. 5 (2022) 112–144.

[39] Y. Gogotsi, The future of MXenes, Chem. Mater. 35 (2023) 8767–8770.

[40] M. Naguib, O. Mashtalir, J. Carle, V. Presser, J. Lu, L. Hultman, Y. Gogotsi, M. W. Barsoum, Two-dimensional transition metal carbides, ACS Nano 6 (2012) 1322–1331.

[41] M. Naguib, J. Halim, J. Lu, K.M. Cook, L. Hultman, Y. Gogotsi, M.W. Barsoum, New two-dimensional niobium and vanadium carbides as promising materials for Li-ion batteries, J. Am. Chem. Soc. 135 (2013) 15966–15969.

[42] K. Maleski, V.N. Mochalin, Y. Gogotsi, Dispersions of two-dimensional titanium carbide MXene in organic solvents, Chem. Mater. 29 (2017) 1632–1640.

[43] P. Urbankowski, B. Anasori, T. Makaryan, D.Q. Er, S. Kota, P.L. Walsh, M.Q. Zhao, V.B. Shenoy, M.W. Barsoum, Y. Gogotsi, Synthesis of two-dimensional titanium nitride Ti_4N_3(MXene), Nanoscale 8 (2016) 11385–11391.

[44] I. Persson, A. el Ghazaly, Q.Z. Tao, J. Halim, S. Kota, V. Darakchieva, J. Palisaitis, M.W. Barsoum, J. Rosen, P. Persson, Tailoring structure, composition, and energy storage properties of MXenes from selective etching of in-plane, chemically ordered max phases, Small 14 (2018) 1703676.

[45] M.K. Han, C.E. Shuck, R. Rakhmanov, D. Parchment, B. Anasori, C.M. Koo, G. Friedman, Y. Gogotsi, Beyond $Ti_3C_2T_x$: MXenes for electromagnetic interference shielding, ACS Nano 14 (2020) 5008–5016.

[46] B. Anasori, Y. Xie, M. Beidaghi, J. Lu, B.C. Hosler, L. Hultman, P.R.C. Kent, Y. Gogotsi, M.W. Barsoum, Two-dimensional, ordered, double transition metals carbides (MXenes), ACS Nano 9 (2015) 9507–9516.

[47] S.K. Nemani, B.W. Zhang, B.C. Wyatt, Z.D. Hood, S. Manna, R. Khaledialidusti, W. C. Hong, M.G. Sternberg, S. Sankaranarayanan, B. Anasori, High-entropy 2D carbide MXenes: $TiVNbMoC_3$ and $TiVCrMoC_3$, ACS Nano 15 (2021) 12815–12825.

[48] Z.G. Du, C. Wu, Y.C.A. Chen, Q. Zhu, Y.L.S. Cui, H.Y. Wang, Y.Z. Zhang, X. Chen, J.X. Shang, B. Li, W.H. Chen, C.T. Liu, S.B. Yang, High-entropy carbonitride MAX phases and their derivative MXenes, Adv. Energy Mater. 12 (2022) 2103228.

[49] A.V. Mohammadi, J. Rosen, Y. Gogotsi, The world of two-dimensional carbides and nitrides (MXenes), Science 372 (2021) 1165.

[50] O. Mashtalir, M. Naguib, V.N. Mochalin, Y. Dall'Agnese, M. Heon, M.W. Barsoum, Y. Gogotsi, Intercalation and delamination of layered carbides and carbonitrides, Nat. Commun. 4 (2013) 7.

[51] A. Al-Temimy, B. Anasori, K.A. Mazzio, F. Kronast, M. Seredych, N. Kurra, M. A. Mawass, S. Raoux, Y. Gogotsi, T. Petit, Enhancement of Ti_3C_2 MXene pseudocapacitance after urea intercalation studied by soft x-ray absorption spectroscopy, J. Phys. Chem. C 124 (2020) 5079–5086.

[52] M. Ghidiu, M.R. Lukatskaya, M.Q. Zhao, Y. Gogotsi, M.W. Barsoum, Conductive two-dimensional titanium carbide 'clay' with high volumetric capacitance, Nature 516 (2014) 78–81.

[53] M.A. Hope, A.C. Forse, K.J. Griffith, M.R. Lukatskaya, M. Ghidiu, Y. Gogotsi, C. P. Grey, NMR reveals the surface functionalisation of Ti_3C_2 MXene, Phys. Chem. Chem. Phys. 18 (2016) 5099–5102.

[54] Y. Zhao, B. Li, C.M. Tian, X.F. Han, Y. Qiu, H. Xiong, K.R. Li, C.Y. Hou, Y.G. Li, H. Z. Wang, Q.H. Zhang, Anhydrous organic etching derived fluorine-rich terminated MXene nanosheets for efficient and stable perovskite solar cells, Chem. Eng. J. 469 (2023) 143862.

[55] Y.X. Li, Y.S. Feng, L.X. Li, X.Z. Yin, F.F. Cao, H. Ye, Green synthesis and applications of MXene for lithium-sulfur batteries, Energy Storage Mater. 67 (2024) 103257.

[56] Y.B. Li, H. Shao, Z.F. Lin, J. Lu, L.Y. Liu, B. Duployer, P. Persson, P. Eklund, L. Hultman, M. Li, K. Chen, X.H. Zha, S.Y. Du, P. Rozier, Z.F. Chai, E. Raymundo-Piñero, P.L. Taberna, P. Simon, Q. Huang, A general Lewis acidic etching route for preparing MXenes with enhanced electrochemical performance in non-aqueous electrolyte, Nat. Mater. 19 (2020) 894–899.

[57] H. Tang, W. Li, L. Pan, C.P. Cullen, Y. Liu, A. Pakdel, D. Long, J. Yang, N. McEvoy, G.S. Duesberg, V. Nicolosi, C. Zhang, In situ formed protective barrier enabled by sulfur@titanium carbide (MXene) ink for achieving high-capacity, long lifetime Li-S batteries, Adv. Sci. 5 (2018) 1800502.

[58] S.Y. Pang, Y.T. Wong, S.G. Yuan, Y. Liu, M.K. Tsang, Z.B. Yang, H.T. Huang, W. T. Wong, J.H. Hao, Universal strategy for HF-free facile and rapid synthesis of two-dimensional MXenes as multifunctional energy materials, J. Am. Chem. Soc. 141 (2019) 9610–9616.

[59] L. Liang, L.Q. Niu, T.L. Wu, D. Zhou, Z.B. Xiao, Fluorine-free fabrication of MXene via photo-fenton approach for advanced lithium-sulfur batteries, ACS Nano 16 (2022) 7971–7981.

[60] M. Li, X.L. Li, G.F. Qin, K. Luo, J. Lu, Y.B. Li, G.J. Liang, Z.D. Huang, J. Zhou, L. Hultman, P. Eklund, P.O.A. Persson, S.Y. Du, Z.F. Chai, C.Y. Zhi, Q. Huang, Halogenated Ti_3C_2 MXenes with electrochemically active terminals for high-performance zinc ion batteries, ACS Nano 15 (2021) 1077–1085.

[61] V. Kamysbayev, A.S. Filatov, H. Hu, X. Rui, F. Lagunas, D. Wang, R.F. Klie, D. V. Talapin, Covalent surface modifications and superconductivity of two-dimensional metal carbide MXenes, Science 369 (2020) 979–983.

[62] X. Pang, Z.R. Lv, S.M. Xu, J.Z. Rong, M.Z. Cai, C.D. Zhao, F.Q. Huang, Ultra-conductive Se-terminated MXene Nb_2CSe_2 one-step synthesis for flexible fast-charging batteries, Energy Storage Mater. 61 (2023) 102860.

[63] C. Xu, L.B. Wang, Z.B. Liu, L. Chen, J.K. Guo, N. Kang, X.L. Ma, H.M. Cheng, W. C. Ren, Large-area high-quality 2D ultrathin Mo_2C superconducting crystals, Nat. Mater. 14 (2015) 1135–1141.

[64] J. Vacík, P. Horák, S. Bakardjieva, V. Bejsovec, G. Ceccio, A. Cannavo, A. Torrisi, V. Lavrentiev, R. Klie, Ion sputtering for preparation of thin MAX and MXene phases, Radiat. Eff. Defects Solids 175 (2020) 177–189.

[65] Z.Q. Sun, T. Liao, Y.H. Dou, S.M. Hwang, M.S. Park, L. Jiang, J.H. Kim, S.X. Dou, Generalized self-assembly of scalable two-dimensional transition metal oxide nanosheets, Nat. Commun. 5 (2014) 3813.

[66] D. Wang, C.K. Zhou, A.S. Filatov, W.J. Cho, F. Lagunas, M.Z. Wang, S. Vaikuntanathan, C. Liu, R.F. Klie, D.V. Talapin, Direct synthesis and chemical vapor deposition of 2D carbide and nitride MXenes, Science 379 (2023) 1242–1247.

[67] T. Zhang, C.E. Shuck, K. Shevchuk, M. Anayee, Y. Gogotsi, Synthesis of three families of titanium carbonitride MXenes, J. Am. Chem. Soc. 145 (2023) 22374–22383.

[68] C.Y. Qiao, H. Wu, X.Y. Xu, Z.X. Guan, W. Ou-Yang, Electrical conductivity enhancement and electronic applications of 2D $Ti_3C_2T_x$ MXene materials, Adv. Mater. Interfaces 8 (2021) 2100903.

[69] T.S. Mathis, K. Maleski, A. Goad, A. Sarycheva, M. Anayee, A.C. Foucher, K. Hantanasirisakul, C.E. Shuck, E.A. Stach, Y. Gogotsi, Modified MAX phase synthesis for environmentally stable and highly conductive Ti_3C_2 MXene, ACS Nano 15 (2021) 6420–6429.

[70] Y. Zhong, X.H. Xia, F. Shi, J.Y. Zhan, J.P. Tu, H.J. Fan, Transition metal carbides and nitrides in energy storage and conversion, Adv. Sci. 3 (2016) 1500286.

[71] L. Jia, S.Q. Zhou, A. Ahmed, Z.C. Yang, S.Q. Liu, H. Wang, F. Li, M. Zhang, Y. J. Zhang, L.Y. Sun, Tuning MXene electrical conductivity towards multifunctionality, Chem. Eng. J. 475 (2023) 146361.

[72] Q. Liang, S.Z. Wang, X.M. Lu, X.H. Jia, J. Yang, F. Liang, Q.Y. Xie, C. Yang, J. Qian, H.J. Song, R.J. Chen, High-entropy MXene as bifunctional mediator toward advanced Li-S full batteries, ACS Nano 18 (2024) 2395–2408.

[73] X.Q. Zhao, M. Liu, Y. Chen, B. Hou, N. Zhang, B.B. Chen, N. Yang, K. Chen, J.L. Li, L.A. An, Fabrication of layered Ti_3C_2 with an accordion-like structure as a potential cathode material for high performance lithium-sulfur batteries, J. Mater. Chem. A 3 (2015) 7870–7876.

[74] X. Liang, Y. Rangom, C.Y. Kwok, Q. Pang, L.F. Nazar, Interwoven MXene nanosheet/carbon-nanotube composites as Li-S cathode hosts, Adv. Mater. 29 (2017) 1603040.

[75] T. Wang, D. Luo, Y.G. Zhang, Z. Zhang, J.Y. Wang, G.L. Cui, X. Wang, A.P. Yu, Z. W. Chen, Hierarchically porous Ti_3C_2 MXene with tunable active edges and unsaturated coordination bonds for superior lithium-sulfur batteries, ACS Nano 15 (2021) 19457–19467.

[76] F.Y. Fan, W.C. Carter, Y.-M. Chiang, Mechanism and kinetics of Li_2S precipitation in lithium-sulfur batteries, Adv. Mater. 27 (2015) 5203–5209.

[77] L. Peng, Z. Wei, C. Wan, J. Li, Z. Chen, D. Zhu, D. Baumann, H. Liu, C.S. Allen, X. Xu, A.I. Kirkland, I. Shakir, Z. Almutairi, S. Tolbert, B. Dunn, Y. Huang, P. Sautet, X. Duan, A fundamental look at electrocatalytic sulfur reduction reaction, Nat. Catal. 3 (2020) 762–770.

[78] Y.N. Zheng, Y.K. Yi, M.H. Fan, H.Y. Liu, X. Li, R. Zhang, M.T. Li, Z.A. Qiao, A high-entropy metal oxide as chemical anchor of polysulfide for lithium-sulfur batteries, Energy Storage Mater. 23 (2019) 678–683.

[79] H.F. Xu, R.M. Hu, Y.Z. Zhang, H.B. Yan, Q. Zhu, J.X. Shang, S.B. Yang, B. Li, Nano high-entropy alloy with strong affinity driving fast polysulfide conversion towards stable lithium sulfur batteries, Energy Storage Mater. 43 (2021) 212–220.

[80] H. Raza, J.Y. Cheng, C. Lin, S. Majumder, G.P. Zheng, G.H. Chen, High-entropy stabilized oxides derived via a low-temperature template route for high-performance lithium-sulfur batteries, EcoMat 5 (2023) e12324.

[81] Y.L. Zhou, L.T. Yin, S.F. Xiang, S. Yu, H.M. Johnson, S.L. Wang, J.Y. Yin, J. Zhao, Y. Luo, P.K. Chu, Unleashing the potential of MXene-based flexible materials for high-performance energy storage devices, Adv. Sci. 11 (2023) 234874.

[82] Z.H. Fu, N. Wang, D. Legut, C. Si, Q.F. Zhang, S.Y. Du, T.C. Germann, J. S. Francisco, R.F. Zhang, Rational design of flexible two-dimensional MXenes with multiple functionalities, Chem. Rev. 119 (2019) 11980–12031.

[83] Z.L. Guo, J. Zhou, C. Si, Z.M. Sun, Flexible two-dimensional Ti_nC_n (n=1, 2 and 3) and their functionalized MXenes predicted by density functional theories, Phys. Chem. Chem. Phys. 17 (2015) 15348–15354.

[84] H. Tang, W. Li, L. Pan, K. Tu, F. Du, T. Qiu, J. Yang, C.P. Cullen, N. McEvoy, C. Zhang, A robust, freestanding MXene-sulfur conductive paper for long-lifetime Li-S batteries, Adv. Funct. Mater. 29 (2019) 1901907.

[85] W. Zhao, Y. Lei, Y. Zhu, Q. Wang, F. Zhang, X. Dong, H.N. Alshareef, Hierarchically structured $Ti_3C_2T_x$ MXene paper for Li-S batteries with high volumetric capacity, Nano Energy 86 (2021) 106120.

[86] C. Yang, X. Wu, H.Y. Xia, J.Z. Zhou, Y.F. Wu, R. Yang, G.M. Zhou, L. Qiu, 3D printed template-assisted assembly of additive-free $Ti_3C_2T_x$ MXene microlattices with customized structures toward high areal capacitance, ACS Nano 16 (2022) 2699–2710.

[87] L. Li, J. Meng, X.R. Bao, Y.P. Huang, X.P. Yan, H.L. Qian, C. Zhang, T.X. Liu, Direct-ink-write 3D printing of programmable micro-supercapacitors from MXene-regulating conducting polymer inks, Adv. Energy Mater. 13 (2023) 2203683.

[88] J.J. Song, D.W. Su, X.Q. Xie, X. Guo, W.Z. Bao, G.J. Shao, G.X. Wang, Immobilizing polysulfides with MXene-functionalized separators for stable lithium-sulfur batteries, ACS Appl. Mater. Interfaces 8 (2016) 29427–29433.

[89] M.R. Lukatskaya, S. Kota, Z. Lin, M.-Q. Zhao, N. Shpigel, M.D. Levi, J. Halim, P.-L. Taberna, M. Barsoum, P. Simon, Y. Gogotsi, Ultra-high-rate pseudocapacitive energy storage in two-dimensional transition metal carbides, Nat. Energy 2 (2017) 17105.

[90] D. Xiong, S. Huang, D. Fang, D. Yan, G. Li, Y. Yan, S. Chen, Y. Liu, X. Li, Y. Von Lim, Y. Wang, B. Tian, Y. Shi, H.Y. Yang, Porosity engineering of MXene membrane towards polysulfide inhibition and fast lithium ion transportation for lithium-sulfur batteries, Small 17 (2021) 2007442.

[91] K. Yang, C. Li, H.Y. Qi, Y.F. Dai, Y.H. Cui, Y.B. He, Developing a MXene quantum dot-based separator for Li-S batteries, J. Mater. Chem. A 11 (2023) 10425–10434.

[92] Y. Dong, S. Zheng, J. Qin, X. Zhao, H. Shi, X. Wang, J. Chen, Z.S. Wu, All-MXene-based integrated electrode constructed by Ti_3C_2 nanoribbon framework host and nanosheet interlayer for high-energy-density Li-S batteries, ACS Nano 12 (2018) 2381–2388.

[93] X.B.A. Liu, X.F. Shao, F. Li, M.W. Zhao, Anchoring effects of S-terminated Ti_2C MXene for lithium-sulfur batteries: A first-principles study, Appl. Surf. Sci. 455 (2018) 522–526.

[94] D. Wang, F. Li, R. Lian, J. Xu, D. Kan, Y. Liu, G. Chen, Y. Gogotsi, Y. Wei, A general atomic surface modification strategy for improving anchoring and electrocatalysis behavior of $Ti_3C_2T_2$ MXene in lithium-sulfur batteries, ACS Nano 13 (2019) 11078–11086.

[95] Y. Wang, J. Shen, L.-C. Xu, Z. Yang, R. Li, R. Liu, X. Li, Sulfur-functionalized vanadium carbide MXene (V_2CS_2) as a promising anchoring material for lithium-sulfur batteries, Phys. Chem. Chem. Phys. 21 (2019) 18559–18568.

[96] H. Wang, S.A. He, Z. Cui, C.T. Xu, J.Q. Zhu, Q. Liu, G.J. He, W. Luo, R.J. Zou, Enhanced kinetics and efficient activation of sulfur by ultrathin MXene coating S-CNTs porous sphere for highly stable and fast charging lithium-sulfur batteries, Chem. Eng. J. 420 (2021) 129693.

[97] G. Li, N. Li, S. Peng, B. He, J. Wang, Y. Du, W. Zhang, K. Han, F. Dang, Highly efficient Nb_2C MXene cathode catalyst with uniform O-terminated surface for lithium-oxygen batteries, Adv. Energy Mater. 11 (2020) 2002721.

[98] Y.S. He, Y. Zhao, Y.G. Zhang, Z.K. He, G.H. Liu, J.D. Li, C.Y. Liang, Q. Li, Building flexibly porous conductive skeleton inlaid with surface oxygen-dominated MXene as an amphiphilic nanoreactor for stable Li-S pouch batteries, Energy Storage Mater. 47 (2022) 434–444.

[99] W.B. Yu, S.B. Ma, M.X. He, R.A. Li, H. Yang, Y. Li, G.P. Yin, P.J. Zuo, Immobilization and kinetic acceleration of lithium polysulfides by iodine-doped MXene nanosheets in lithium-sulfur batteries, J. Phys. Chem. C 126 (2022) 10986–10994.

[100] M.Y. Peng, M.L. Dong, W. Wei, H.J. Xu, C.T. Liu, C.Y. Shen, The introduction of amino termination on Ti_3C_2 MXene surface for its flexible film with excellent property, Carbon 179 (2021) 400–407.

[101] M.Y. Peng, Z.W. Wu, W. Wei, H.J. Xu, C.T. Liu, C.Y. Shen, Amino termination of Ti_3C_2 MXene induces its graphene hybridized film with enhanced ordered nanostructure and excellent multiperformance, Adv. Mater. Interfaces 9 (2022) 2102418.

[102] C.K. Zhou, D. Wang, F. Lagunas, B. Atterberry, M. Lei, H.C. Hu, Z.R. Zhou, A. S. Filatov, D.E. Jiang, A.J. Rossini, R.F. Klie, D.V. Talapin, Hybrid organic-inorganic two-dimensional metal carbide MXenes with amido- and imido-terminated surfaces, Nat. Chem. 15 (2023) 1722–1729.

[103] T.P. Zhang, W.L. Shao, S.Y. Liu, Z.H. Song, R.Y. Mao, X. Jin, X.G. Jian, F.Y. Hu, A flexible design strategy to modify $Ti_3C_2T_x$ MXene surface terminations via nucleophilic substitution for long-life Li-S batteries, J. Energy Chem. 74 (2022) 349–358.

[104] J. Zhang, L.J. Jia, H.Z. Lin, J. Wang, Advances and prospects of 2D graphene-based materials/hybrids for lithium metal-sulfur full battery: From intrinsic property to catalysis modification, Adv. Energy Sustain. Res. 3 (2022) 2100187.

[105] Q.C. Li, Y.Z. Song, R.Z. Xu, L. Zhang, J. Gao, Z. Xia, Z.N. Tian, N. Wei, M. H. Rümmeli, X.L. Zou, J.Y. Sun, Z.F. Liu, Biotemplating growth of nepenthes-like N-doped graphene as a bifunctional polysulfide scavenger for Li-S batteries, ACS Nano 12 (2018) 10240–10250.

[106] C. Lu, L. Yang, B. Yan, L. Sun, P. Zhang, W. Zhang, Z. Sun, Nitrogen-doped Ti_3C_2 MXene: Mechanism investigation and electrochemical analysis, Adv. Funct. Mater. 30 (2020) 2000852.

[107] Y. Song, Z. Sun, Z. Fan, W. Cai, Y. Shao, G. Sheng, M. Wang, L. Song, Z. Liu, Q. Zhang, J. Sun, Rational design of porous nitrogen-doped Ti_3C_2 MXene as a multifunctional electrocatalyst for Li-S chemistry, Nano Energy 70 (2020) 104555.

[108] B. Ding, W.J. Ong, J.Z. Jiang, X.Z. Chen, N. Li, Uncovering the electrochemical mechanisms for hydrogen evolution reaction of heteroatom doped M_2C MXene (m = Ti, Mo), Appl. Surf. Sci. 500 (2020) 143987.

[109] G. Jiang, N. Zheng, X. Chen, G. Ding, Y. Li, F. Sun, Y. Li, In-situ decoration of MOF-derived carbon on nitrogen-doped ultrathin MXene nanosheets to multifunctionalize separators for stable Li-S batteries, Chem. Eng. J. 373 (2019) 1309–1318.

[110] Y.Z. Luo, Z.C. Ye, L.H. Mo, B.Y. Li, S.F. Li, A freestanding nitrogen-doped MXene/graphene cathode for high-performance Li-S batteries, Nanoscale Adv. 4 (2022) 2189–2195.

[111] J. Wang, Z. Zhang, X. Yan, S. Zhang, Z. Wu, Z. Zhuang, W.Q. Han, Rational design of porous N-Ti_3C_2 MXene@CNT microspheres for high cycling stability in Li-S battery, Nano-Micro Lett. 12 (2020) 4.

[112] C. Wei, M. Tian, Z. Fan, L. Yu, Y. Song, X. Yang, Z. Shi, M. Wang, R. Yang, J. Sun, Concurrent realization of dendrite-free anode and high-loading cathode via 3D printed N-Ti_3C_2 MXene framework toward advanced Li-S full batteries, Energy Storage Mater. 41 (2021) 141–151.

[113] G.Q. Zhao, S. Liu, X. Zhang, Y.M. Zhang, H. Shi, Y. Liu, L.R. Hou, C.Z. Yuan, Construction of Co@N-CNTs grown on N-Mo_xC nanosheets for separator modification to enhance adsorption and catalytic conversion of polysulfides in Li-S batteries, J. Mater. Chem. A 11 (2023) 1856–1865.

[114] Y. Wen, R. Li, J. Liu, Z. Wei, S. Li, L. Du, K. Zu, Z. Li, Y. Pan, H. Hu, A temperature-dependent phosphorus doping on $Ti_3C_2T_x$ MXene for enhanced supercapacitance, J. Colloid Interf. Sci. 604 (2021) 239–248.

[115] H. Yuan, J. Yang, Y.W. Zhang, S-doped $Ti_3C_2F_2$ MXene as an ideal sulfur cathode host for high-performance rechargeable lithium-sulfur batteries, J. Mater. Chem. A 11 (2023) 17841–17847.

[116] M. Fatima, J. Fatheema, N.B. Monir, A.H. Siddique, B. Khan, A. Islam, D. Akinwande, S. Rizwan, Nb-doped MXene with enhanced energy storage capacity and stability, Front. Chem. 8 (2020) 168.

[117] Z.W. Gao, W.R. Zheng, L.Y.S. Lee, Highly enhanced pseudocapacitive performance of vanadium-doped MXenes in neutral electrolytes, Small 15 (2019) 1902649.

[118] D.A. Kuznetsov, Z.X. Chen, P.V. Kumar, A. Tsoukalou, A. Kierzkowska, P. M. Abdala, O.V. Safonova, A. Fedorov, C.R. Müller, Single site cobalt substitution in 2D molybdenum carbide (MXene) enhances catalytic activity in the hydrogen evolution reaction, J. Am. Chem. Soc. 141 (2019) 17809–17816.

[119] W. Peng, M. Luo, X.D. Xu, K. Jiang, M. Peng, D.C. Chen, T.S. Chan, Y.W. Tan, Spontaneous atomic ruthenium doping in Mo_2CT_x MXene defects enhances electrocatalytic activity for the nitrogen reduction reaction, Adv. Energy Mater. 10 (2020) 2001364.

[120] Y.Z. Song, Y.J. Sun, L. Chen, L.X. Song, Q. Yang, Z.X. Shi, L. Chen, W.L. Cai, Seeding Co atoms on size effect-enabled V_2C MXene for kinetically boosted lithium-sulfur batteries, Adv. Funct. Mater. 34 (2024) 2409748.

[121] D. Zhang, S. Wang, R. Hu, J. Gu, Y. Cui, B. Li, W. Chen, C. Liu, J. Shang, S. Yang, Catalytic conversion of polysulfides on single atom zinc implanted MXene toward high-rate lithium-sulfur batteries, Adv. Funct. Mater. 2002471 (2020).

[122] M.Y. Wang, J.J. Mao, Y.D. Pang, X.L. Zhang, H.Y. Wang, Z.X. Yang, Z.S. Lu, S. T. Yang, Theoretical identification of the superior anchoring effect and electrochemical performance of Ti_2CS_2 by single atom Zn doping for lithium-sulfur batteries, Phys. Chem. Chem. Phys. 25 (2023) 19795–19803.

[123] Q.H. Gu, Y.J. Qi, J.N. Chen, M. Lu, B.S. Zhang, Cobalt nanoparticles loaded on MXene for Li-S batteries: Anchoring polysulfides and accelerating redox reactions, Small 18 (2022) 2204005.

[124] M. Zheng, Z.H. Luo, Y. Song, M.X. Zhou, C. Guo, Y. Shi, L. Li, Q. Sun, B. Shi, Z. L. Yi, F.Y. Su, J.J. Shao, G.M. Zhou, Carbon-coated nitrogen, vanadium co-doped MXene interlayer for enhanced polysulfide shuttling inhibition in lithium-sulfur batteries, J. Power Sources 580 (2023) 233445.

[125] H.F. Gu, W. Yue, J.Q. Hu, X.F. Niu, H. Tang, F.J. Qin, Y. Li, Q. Yan, X.M. Liu, W. J. Xu, Z.Y. Sun, Q.Q. Liu, W.S. Yan, L.R. Zheng, Y. Wang, H. Wang, X.Y. Li, L. Zhang, G.M. Xia, W.X. Chen, Asymmetrically coordinated Cu-N_1C_2 single-atom catalyst immobilized on $Ti_3C_2T_x$ MXene as separator coating for lithium-sulfur batteries, Adv. Energy Mater. 13 (2023) 2204014.

[126] Z.L. Liu, F.H. Xue, X. Zhao, Z. Chen, H.W. Zheng, R.J. Ding, P.Y. Li, L.L. Xu, J. H. Xiong, Q.Y. Peng, X.D. He, Anti-stacking synthesis of MXene-reduced graphene oxide sponges for aqueous zinc-ion hybrid supercapacitor with improved performance, J. Mater. Sci. Technol. 154 (2023) 22–29.

[127] Q.H. Gu, Y.Q. Cao, J.N. Chen, Y.J. Qi, Z.F. Zhai, M. Lu, N. Huang, B.S. Zhang, Fluorine-modulated MXene-derived catalysts for multiphase sulfur conversion in lithium–sulfur battery, Nano-Micro Lett. 16 (2024) 266.

[128] S.Y. Wu, X. Li, Y.Z. Zhang, Q.H. Guan, J. Wang, C.Y. Shen, H.Z. Lin, J.T. Wang, Y. L. Wang, L. Zhan, L.C. Ling, Interface engineering of MXene-based heterostructures for lithium-sulfur batteries, Nano Res. 16 (2023) 9158–9178.

[129] H. Zhang, L. Yang, P.G. Zhang, C.J. Lu, D.W. Sha, B.Z. Yan, W. He, M. Zhou, W. Zhang, L. Pan, Z.M. Sun, MXene-derived Ti_nO_{2n-1} quantum dots distributed on

porous carbon nanosheets for stable and long-life Li-S batteries: Enhanced polysulfide mediation via defect engineering, Adv. Mater. 33 (2021) 2008447.

[130] S.G. Deng, T.Z. Guo, J. Heier, C.F. Zhang, Unraveling polysulfide's adsorption and electrocatalytic conversion on metal oxides for Li-S batteries, Adv. Sci. 10 (2023) 2204930.

[131] Z. Li, C. Zhou, J. Hua, X. Hong, C. Sun, H.W. Li, X. Xu, L. Mai, Engineering oxygen vacancies in a polysulfide-blocking layer with enhanced catalytic ability, Adv. Mater. 32 (2020) 1907444.

[132] X. Liu, J.Q. Huang, Q. Zhang, L.Q. Mai, Nanostructured metal oxides and sulfides for lithium-sulfur batteries, Adv. Mater. 29 (2017) 1601759.

[133] M.P. Yu, J.S. Ma, H.Q. Song, A.J. Wang, F.Y. Tian, Y.S. Wang, H. Qiu, R.M. Wang, Atomic layer deposited TiO_2 on a nitrogen-doped graphene/sulfur electrode for high performance lithium-sulfur batteries, Energy Environ. Sci. 9 (2016) 1495–1503.

[134] X. Wang, D. Luo, J. Wang, Z. Sun, G. Cui, Y. Chen, T. Wang, L. Zheng, Y. Zhao, L. Shui, G. Zhou, K. Kempa, Y. Zhang, Z. Chen, Strain engineering of a MXene/CNT hierarchical porous hollow microsphere electrocatalyst for a high-efficiency lithium polysulfide conversion process, Angew. Chem. Int. Ed. 60 (2021) 2371–2378.

[135] L. Jiao, C. Zhang, C. Geng, S. Wu, H. Li, W. Lv, Y. Tao, Z. Chen, G. Zhou, J. Li, G. Ling, Y. Wan, Q.H. Yang, Capture and catalytic conversion of polysulfides by in situ built TiO_2-MXene heterostructures for lithium-sulfur batteries, Adv. Energy Mater. 9 (2019) 1900219.

[136] M.Y. Xu, T.L. Wu, J. Qi, D. Zhou, Z.B. Xiao, V_2C/VO_2 nanoribbon intertwined nanosheet dual heterostructure for highly flexible and robust lithium-sulfur batteries, J. Mater. Chem. A 9 (2021) 21429–21439.

[137] T. Wang, Y.Y. Liu, X.M. Zhang, J.Y. Wang, Y.G. Zhang, Y.B. Li, Y.J. Zhu, G.R. Li, X. Wang, Interspersing partially oxidized V_2C nanosheets and carbon nanotubes toward multifunctional polysulfide barriers for high-performance lithium-sulfur batteries, ACS Appl. Mater. Interfaces 13 (2021) 56085–56094.

[138] Z. Wang, K. Yu, Y. Feng, R. Qi, J. Ren, Z. Zhu, VO_2(p)-V_2C(MXene) grid structure as a lithium polysulfide catalytic host for high-performance Li-S battery, ACS Appl. Mater. Interfaces 11 (2019) 44282–44292.

[139] C. Wei, M. Tian, M. Wang, Z. Shi, L. Yu, S. Li, Z. Fan, R. Yang, J. Sun, Universal in situ crafted Mo_x-MXene heterostructures as heavy and multifunctional hosts for 3D-printed Li-S batteries, ACS Nano 14 (2020) 16073–16084.

[140] D.K. Lee, Y. Chae, H. Yun, C.W. Ahn, J.W. Lee, CO_2-oxidized $Ti_3C_2T_x$-MXenes components for lithium-sulfur batteries: Suppressing the shuttle phenomenon through physical and chemical adsorption, ACS Nano 14 (2020) 9744–9754.

[141] C.L. Song, W. Zhang, Q.W. Jin, Y.G. Zhang, X. Wang, Z. Bakenov, In-situ constructed accordion-like Nb_2C/Nb_2O_5 heterostructure as efficient catalyzer towards high-performance lithium-sulfur batteries, J. Power Sources 520 (2022) 230902.

[142] H. Zhang, Y.W. Zhang, L. Li, H.X. Zhou, M.C. Wang, L.X. Li, X. Geng, B.G. An, C. G. Sun, A rational design of titanium-based heterostructures as electrocatalyst for boosted conversion kinetics of polysulfides in Li-S batteries, J. Colloid Interface Sci. 633 (2023) 432–440.

[143] A. Rafieerad, A. Amiri, G.L. Sequiera, W.A. Yan, Y.J. Chen, A.A. Polycarpou, S. Dhingra, Development of fluorine-free tantalum carbide MXene hybrid structure as a biocompatible material for supercapacitor electrodes, Adv. Funct. Mater. 31 (2021) 2100015.

[144] Q. Liang, S.Z. Wang, X.H. Jia, J. Yang, Y. Li, D. Shao, L. Feng, J.X. Liao, H.J. Song, MXene derivative Ta_4C_3-Ta_2O_5 heterostructure as bi-functional barrier for Li-S batteries, J. Mater. Sci. Technol. 151 (2023) 89–98.

[145] Y. Wang, R. Zhang, J. Chen, H. Wu, S. Lu, K. Wang, H. Li, C.J. Harris, K. Xi, R. V. Kumar, S. Ding, Enhancing catalytic activity of titanium oxide in lithium-sulfur batteries by band engineering, Adv. Energy Mater. 9 (2019) 1900953.

[146] E.H.M. Salhabi, J. Zhao, J. Wang, M. Yang, B. Wang, D. Wang, Hollow multi-shelled structural TiO_{2-x} with multiple spatial confinement for long-life lithium-sulfur batteries, Angew. Chem. Int. Ed. 58 (2019) 9078–9082.

[147] L. Ma, Y.Q. Zhang, S. Zhang, L. Wang, C.X. Zhang, Y.J. Chen, Q. Wu, L.B. Chen, L. J. Zhou, W.F. Wei, Integrating energy band alignment and oxygen vacancies engineering of TiO_2 anatase/rutile homojunction for kinetics-enhanced Li-S batteries, Adv. Funct. Mater. 33 (2023) 2305788.

[148] Q. Li, Z.T. Xiao, W.N. Jia, Q. Li, X.G. Li, W.T. Wang, Copper nanowires decorated with TiO_{2-x} from MXene for enhanced electrocatalytic nitrogen oxidation into nitrate under vacuum assistance, Nano Res. 16 (2023) 12357–12362.

[149] D.Y. Zhang, H.K. Liu, M.R. Younis, S. Lei, Y.Z. Chen, P. Huang, J. Lin, In-situ TiO_{2-x} decoration of titanium carbide MXene for photo/sono-responsive antitumor theranostics, J. Nanobiotechnol. 20 (2022) 53.

[150] Y.W. Wang, X.S. Hu, H.R. Song, Y. Cai, Z. Li, D.Y. Zu, P.X. Zhang, D.T. Chong, N. B. Gao, Y.M. Shen, C.P. Li, Oxygen vacancies in actiniae-like Nb_2O_5/Nb_2C MXene heterojunction boosting visible light photocatalytic no removal, Appl. Catal. B-Environ. 299 (2021) 120677.

[151] J. Xia, R.H. Gao, Y. Yang, Z. Tao, Z.Y. Han, S.C. Zhang, Y.L. Xing, P.H. Yang, X. Lu, G.M. Zhou, Ti_nO_{2n-1}/MXene hierarchical bifunctional catalyst anchored on graphene aerogel toward flexible and high-energy Li-S batteries, ACS Nano 16 (2022) 19133–19144.

[152] V.P. Nguyen, J.S. Park, H.C. Shim, J.M. Yuk, J.H. Kim, D. Kim, S.M. Lee, Accelerated sulfur evolution reactions by TiS_2/TiO_2@MXene host for high-volumetric-energy-density lithium-sulfur batteries, Adv. Funct. Mater. 33 (2023) 2303503.

[153] H. Wang, Z. Cui, S.A. He, J.Q. Zhu, W. Luo, Q. Liu, R.J. Zou, Construction of ultrathin layered MXene-TiN heterostructure enabling favorable catalytic ability for high-areal-capacity lithium-sulfur batteries, Nano-Micro Lett. 14 (2022) 189.

[154] Y. Yao, H. Wang, H. Yang, S. Zeng, R. Xu, F. Liu, P. Shi, Y. Feng, K. Wang, W. Yang, X. Wu, W. Luo, Y. Yu, A dual-functional conductive framework embedded with TiN-VN heterostructures for highly efficient polysulfide and lithium regulation toward stable Li-S full batteries, Adv. Mater. 32 (2020) 1905658.

[155] K. Wu, G.D. Lu, B. Huang, Z.W. Hu, Y. Lv, H.A. Younus, X.W. Wang, Z.X. Liu, S. G. Zhang, Entropy-driven highly chaotic MXene-based heterostructures as an efficient sulfur redox electrocatalysts for Li-S battery, Adv. Funct. Mater. 34 (2024) 2404976.

[156] C.L. Song, W. Zhang, Q.W. Jin, Y. Zhao, Y.G. Zhang, X. Wang, Z. Bakenov, Oxidized Nb_2C MXene as catalysts for lithium-sulfur batteries: Mitigating the shuttle phenomenon by facilitating catalytic conversion of lithium polysulfides, J. Mater. Sci. Technol. 119 (2022) 45–52.

[157] Z.L. Tan, S. Liu, X. Zhang, J.X. Wei, Y. Liu, L.R. Hou, C.Z. Yuan, Few-layered V_2C MXene derived 3d V_3S_4 nanocrystal functionalized carbon flakes boosting polysulfide adsorption and catalytic conversion towards Li-S batteries, J. Mater. Chem. A 10 (2022) 18679–18689.

[158] X. Li, Q.H. Guan, Z.C. Zhuang, Y.Z. Zhang, Y.H. Lin, J. Wang, C.Y. Shen, H.Z. Lin, Y.L. Wang, L. Zhan, L.C. Ling, Ordered mesoporous carbon grafted MXene catalytic heterostructure as Li-ion kinetic pump toward high-efficient sulfur/sulfide conversions for Li-S battery, ACS Nano 17 (2023) 1653–1662.

[159] B. Zhang, C. Luo, G. Zhou, Z.Z. Pan, J. Ma, H. Nishihara, Y.B. He, F. Kang, W. Lv, Q.H. Yang, Lamellar MXene composite aerogels with sandwiched carbon nanotubes enable stable lithium-sulfur batteries with a high sulfur loading, Adv. Funct. Mater. 31 (2021) 2100793.

[160] M. Guo, C.Y. Yuan, T. Xu, S.L. Zhong, W.B. Wang, T.X. Zou, T.F. Zhang, X.B. Yu, In situ built nanoconfined TiO_2 particles in robust-flexible MXene@rGO conductive framework enabling high-performance hybrid magnesium-sulfur batteries, Adv. Energy Mater. 13 (2023) 2300417.

[161] L.Y. Cao, C.W. Wang, Y.X. Huang, Structure optimization of graphene aerogel-based composites and applications in batteries and supercapacitors, Chem. Eng. J. 454 (2023) 140094.

[162] J. Song, X. Guo, J. Zhang, Y. Chen, C. Zhang, L. Luo, F. Wang, G. Wang, Rational design of free-standing 3D porous MXene/rGO hybrid aerogels as polysulfide reservoirs for high-energy lithium-sulfur batteries, J. Mater. Chem. A 7 (2019) 6507–6513.

[163] X.Y. Tang, R.Y. Gan, L.Q. Tan, C. Tong, C.P. Li, Z.D. Wei, 3D net-like GO-d-$Ti_3C_2T_x$ MXene aerogels with catalysis/adsorption dual effects for high-performance lithium-sulfur batteries, ACS Appl. Mater. Interfaces 13 (2021) 55235–55242.

[164] P. Liu, L. Qu, X. Tian, Y. Yi, J. Xia, T. Wang, J. Nan, P. Yang, T. Wang, B. Fang, M. Li, B. Yang, $Ti_3C_2T_x$/graphene oxide free-standing membranes as modified separators for lithium-sulfur batteries with enhanced rate performance, ACS Appl. Energy Mater. 3 (2020) 2708–2718.

[165] J. Wu, T. Ye, Y.C. Wang, P.Y. Yang, Q.C. Wang, W.Y. Kuang, X.L. Chen, G. H. Duan, L.M. Yu, Z.Q. Jin, J.Q. Qin, Y.P. Lei, Understanding the catalytic kinetics of polysulfide redox reactions on transition metal compounds in Li-S batteries, ACS Nano 16 (2022) 15734–15759.

[166] T.L. Li, Y.Z. Liu, J. Wang, H. Hao, Z.Y. Yu, H.X. Liu, Constructing metal telluride-grafted MXene as electron "donor-acceptor" heterostructure for accelerating redox kinetics of high-efficiency Li-S batteries, J. Mater. Chem. A 12 (2024) 12691–12701.

[167] F.W. Xie, C.J. Xu, Y.C. Song, Q. Liang, J.J. Ji, S.Z. Wang, 2D-2D heterostructure of ionic liquid-exfoliated MoS_2/MXene as lithium polysulfide barrier for Li-S batteries, J. Colloid Interface Sci. 636 (2023) 528–536.

[168] S.H. Tian, Q. Zeng, G. Liu, J.J. Huang, X. Sun, D. Wang, H.C. Yang, Z. Liu, X. C. Mo, Z.X. Wang, K. Tao, S.L. Peng, Multi-dimensional composite frame as bifunctional catalytic medium for ultra-fast charging lithium-sulfur battery, Nano-Micro Lett. 14 (2022) 196.

[169] S.Y. Wu, W. Wang, J.W. Shan, X.Y. Wang, D.Z. Lu, J.L. Zhu, Z.G. Liu, L.G. Yue, Y. Y. Li, Conductive 1T-VS_2-MXene heterostructured bidirectional electrocatalyst enabling compact Li-S batteries with high volumetric and areal capacity, Energy Storage Mater. 49 (2022) 153–163.

[170] W. Wang, X.Y. Wang, L. Chen, D.Z. Lu, W.L. Zhou, Y.Y. Li, Conductive metal-metal phase and built-in electric field of 1T-VSe_2-MXene hetero-structure to accelerate dual-directional sulfur conversion for high-performance Li-S batteries, Chem. Eng. J. 461 (2023) 152100.

[171] W. Wang, X.Y. Wang, J.W. Shan, L.G. Yue, Z.H. Shao, L. Chen, D.Z. Lu, Y.Y. Li, Atomic-level design rules of metal-cation-doped catalysts: Manipulating electron affinity/ionic radius of doped cations for accelerating sulfur redox kinetics in Li-S batteries, Energy Environ. Sci. 16 (2023) 2669–2683.

[172] C.Y. Song, Q. Yan, T.R. Zhang, H. Lin, H.L. Ye, Q.F. Yao, S.L. Zhang, Y. Li, G. L. Wang, J.Y. Lee, Enhanced polysulfide conversion through metal oxide-support interaction in mnox/MXene, Chem. Eng. J. 420 (2021) 130452.

[173] Y.L. Ren, B. Wang, H.L. Liu, H. Wu, H.F. Bian, Y.J. Ma, H.M. Lu, S.C. Tang, X. K. Meng, CoP nanocages intercalated MXene nanosheets as a bifunctional mediator for suppressing polysulfide shuttling and dendritic growth in lithium-sulfur batteries, Chem. Eng. J. 450 (2022) 138046.

[174] B. Guan, X. Sun, Y. Zhang, X. Wu, Y. Qiu, M. Wang, L. Fan, N. Zhang, The discovery of interfacial electronic interaction within cobalt boride@MXene for high performance lithium-sulfur batteries, Chinese Chem. Lett. 32 (2021) 2249–2253.

[175] Z.W. Hu, Z.X. Liu, B. Huang, Y. Gao, F. Song, H.A. Younus, X.W. Wang, S. G. Zhang, MXene supported transition metal nanoparticles accelerate sulfur reduction reaction kinetics, J. Mater. Chem. A 10 (2022) 13758–13768.

[176] Z. Zhu, Y.X. Zeng, Z.H. Pei, D.Y. Luan, X. Wang, X.W. Lou, Bimetal-organic framework nanoboxes enable accelerated redox kinetics and polysulfide trapping for lithium-sulfur batteries, Angew. Chem. Int. Edit. 62 (2023) 202305828.

[177] S.Y. Bai, X.Z. Liu, K. Zhu, S.C. Wu, H.S. Zhou, Metal-organic framework-based separator for lithium-sulfur batteries, Nat. Energy 1 (2016) 16094.

[178] Y.H. Liu, L.X. Li, A.Y. Wen, F.F. Cao, H. Ye, A Janus MXene/MOF separator for the all-in-one enhancement of lithium-sulfur batteries, Energy Storage Mater. 55 (2023) 652–659.

[179] Y.L. Ren, Q.X. Zhai, B. Wang, L.B. Hu, Y.J. Ma, Y.M. Dai, S.C. Tang, X.K. Meng, Synergistic adsorption-electrocatalysis of 2D/2D heterostructure toward high performance Li-S batteries, Chem. Eng. J. 439 (2022) 135535.

[180] C.Y. Wen, D.H. Guo, X.Z. Zheng, H.F. Li, G.B. Sun, Hierarchical nMOF-867/MXene nanocomposite for chemical adsorption of polysulfides in lithium-sulfur batteries, ACS Appl. Energy Mater. 4 (2021) 8231–8241.

[181] Z.Q. Ye, Y. Jiang, L. Li, F. Wu, R.J. Chen, Self-assembly of 0D-2D heterostructure electrocatalyst from MOF and MXene for boosted lithium polysulfide conversion reaction, Adv. Mater. 33 (2021) 2101204.

[182] X.W. Geng, C.G. Liu, C. Zhao, Z.J. Jiang, E.G. Lim, Y.J. Wang, I. Mitrovic, L. Yang, P.F. Song, Sulfydryl-modified MXene as a sulfur host for highly stable Li-S batteries, Electrochim. Acta 441 (2023) 141877.

[183] Y.W. Cao, Y.C. Jia, X.D. Meng, X.Y. Fan, J. Zhang, J. Zhou, D. Matoga, C. W. Bielawski, J.X. Geng, Covalently grafting conjugated porous polymers to MXene offers a two-dimensional sandwich-structured electrocatalytic sulfur host for lithium-sulfur batteries, Chem. Eng. J. 446 (2022) 137365.

[184] H.S. Xu, H. Zhang, Y.F. Wang, C. Tang, T.Y. Xiao, Z. Xu, H. Li, F.G. Xu, Y.Y. Mai, Two-dimensional sandwich-like MXene-conductive polymer nanocomposite with in-plane cylindrical mesopores for long cycling lithium-sulfur batteries, 2D Mater. 10 (2023) 025006.

[185] J. Xu, S.H. An, X.Y. Song, Y.J. Cao, N. Wang, X. Qiu, Y. Zhang, J.W. Chen, X. L. Duan, J.H. Huang, W. Li, Y.G. Wang, Towards high performance Li-S batteries via sulfonate-rich COF-modified separator, Adv. Mater. 33 (2021) 2105178.

[186] T.L. Li, W.T. Liu, Y.Z. Liu, J. Wang, H. Hao, Z.Y. Yu, H.X. Liu, Covalent organic frameworks integrated MXene as selective "ion-sieving" heterostructure catalyst for kinetics-reinforced Li-S batteries, Chem. Eng. J. 498 (2024) 155817.

[187] J. Xu, W.Q. Tang, C. Yang, I. Manke, N. Chen, F.L. Lai, T. Xu, S.H. An, H.L. Liu, Z. L. Zhang, Y.J. Cao, N. Wang, S.L. Zhao, D.F. Niu, R.J. Chen, A highly conductive COF@CNT electrocatalyst boosting polysulfide conversion for Li-S chemistry, ACS Energy Lett. 6 (2021) 3053–3062.

[188] P. Li, H. Lv, Z. Li, X. Meng, Z. Lin, R. Wang, X. Li, The electrostatic attraction and catalytic effect enabled by ionic-covalent organic nanosheets on MXene for separator modification of lithium-sulfur batteries, Adv. Mater. 33 (2021) 2007803.

[189] R. Meng, Q. Deng, C. Peng, B. Chen, K. Liao, L. Li, Z. Yang, D. Yang, L. Zheng, C. Zhang, J. Yang, Two-dimensional organic-inorganic heterostructures of in situ-grown layered COF on Ti_3C_2 MXene nanosheets for lithium-sulfur batteries, Nano Today 35 (2020) 100991.

[190] G. Zhang, C. Zhou, J.C. Long, Y. Li, L. Lv, K.J. Yan, X.H. Chen, C.X. Dong, X. Xu, L. Q. Mai, Bottom-up synthesis of 2D heterostructures enables effective polysulfides inhibition and conversion, Nano Res. 16 (2023) 8488–8496.

[191] X.Y. Zhou, Y.C. Cui, X. Huang, Q.Y. Zhang, B. Wang, S.C. Tang, Interface engineering of Fe_3Se_4/FeSe heterostructures encapsulated in MXene for boosting LiPS conversion and inhibiting shuttle effect, Chem. Eng. J. 457 (2023) 141139.

[192] C.L. Wei, B.J. Xi, P. Wang, Y.Z. Liang, Z.R. Wang, K.D. Tian, J.K. Feng, S.L. Xiong, In situ anchoring ultrafine ZnS nanodots on 2D MXene nanosheets for accelerating polysulfide redox and regulating Li plating, Adv. Mater. 35 (2023) 2303780.

[193] T.T. Li, L.P. Liang, Z.Y. Chen, J.L. Zhu, P.K. Shen, Hollow $Ti_3C_2T_x$ MXene@$CoSe_2$/N-doped carbon heterostructured composites for multiphase electrocatalysis process in lithium-sulfur batteries, Chem. Eng. J. 474 (2023) 145970.

[194] Z.M. Huang, Y.X. Zhu, Y. Kong, Z.X. Wang, K.L. He, J.D. Qin, Q.T. Zhang, C.L. Su, Y.L. Zhong, H. Chen, Efficient synergism of chemisorption and wackenroder reaction via heterostructured La_2O_3-$Ti_3C_2T_x$-embedded carbon nanofiber for high-energy lithium-sulfur pouch cells, Adv. Funct. Mater. 33 (2023) 2303422.

[195] Y.C. Cui, X.Y. Zhou, X. Huang, L. Xu, S.C. Tang, Binary transition-metal sulfides/MXene synergistically promote polysulfide adsorption and conversion in lithium-sulfur batteries, ACS Appl. Mater. Interfaces 15 (2023) 49223–49232.

[196] L. Chen, L.G. Yue, X.Y. Wang, S.Y. Wu, W. Wang, D.Z. Lu, X. Liu, W.L. Zhou, Y. Y. Li, Synergistically accelerating adsorption-electrocataysis of sulfur species via interfacial built-in electric field of SnS_2-MXene mott-schottky heterojunction in Li-S batteries, Small 19 (2023) 2206462.

[197] X.C. Chen, L.B. Li, Y.H. Shan, D. Zhou, W.J. Cui, Y.M.Y. Zhao, Notes in accordions-organized MXene equipped with CeO_2 for synergistically adsorbing and catalyzing polysulfides for high-performance lithium-sulfur batteries, J. Energy Chem. 70 (2022) 502–510.

[198] Z.H. Fan, C. Zhang, W.X. Hua, H. Li, Y. Jiao, J.Y. Xia, C.N. Geng, R.W. Meng, Y. X. Liu, Q.J. Tang, Z.Y. Lu, T.X. Shang, G.W. Ling, Q.H. Yang, Enhanced chemical trapping and catalytic conversion of polysulfides by diatomite/MXene hybrid interlayer for stable Li-S batteries, J. Energy Chem. 62 (2021) 590–598.

[199] Y.T. Jiang, P. Liang, M.J. Tang, S.P. Sun, H.H. Min, J.C. Han, X.D. Shen, H. Yang, D.L. Chao, J. Wang, A high-throughput screening permeability separator with high catalytic conversion kinetics for Li-S batteries, J. Mater. Chem. A 10 (2022) 22080–22092.

[200] C.Y. Zhang, J.A. Feng, X. Guo, J.Q. Zhang, W.X. Zhang, L.X. Zhang, J.J. Song, G. J. Shao, G.X. Wang, Blocking polysulfide by physical confinement and catalytic conversion of SiO_2@MXene for Li-S battery, Appl. Phys. Lett. 122 (2023) 193901.

[201] X.J. Wang, B.C. Zhu, D.F. Xu, Z.C. Gao, Y. Yao, T. Liu, J.G. Yu, L.Y. Zhang, Synergistic effects of Co_3We_4 and $Ti_2C_3T_{(x)}$ for performance enhancement on lithium-sulfur batteries, ACS Appl. Mater. Interfaces 15 (2023) 26882–26892.

[202] Q. Wang, A.M. Liu, S.M. Qiao, Q. Zhang, C.H. Huang, D. Lei, X.S. Shi, G.H. He, F. X. Zhang, Mott-schottky MXene@WS_2 heterostructure: Structural and thermodynamic insights and application in ultra stable lithium-sulfur batteries, ChemSusChem 16 (2023) e202300507.

[203] W. Wang, X.Y. Wang, J.W. Shan, L.G. Yue, W.L. Wang, Y.Y. Li, Conductive few-layered 1T-$MoSe_2$/MXene as a highly-efficient catalyst for accelerating bidirectional sulfur redox kinetics in Li-S batteries, J. Alloy. Compd. 936 (2023) 168250.

[204] R.T. Guo, W. Li, R.Q. Huang, M.Q. Chen, Z. Liu, G.C. Han, Shuttle-inhibited 3D sandwich MXene/SnO_2QDs sulfur host for high-performance lithium-sulfur batteries, J. Alloy. Compd. 937 (2023) 168427.

[205] D. Chen, T.J. Zhu, S. Shen, Y.A. Cao, Y.Y. Mao, W.J. Wang, E.C. Bao, H.F. Jiang, In situ synthesis of VS_4/$Ti_3C_2T_x$ MXene composites as modified separators for lithium-sulfur battery, J. Colloid Interface Sci. 650 (2023) 480–489.

[206] L.C. Cai, H.J. Ying, P.F. Huang, Z. Zhang, H. Tan, Q.Z. Han, W.Q. Han, In-situ grown $Ti_3C_2T_x$@$CoSe_2$ heterostructure as trapping-electrocatalyst for accelerating polysulfides conversion in lithium-sulfur battery, Chem. Eng. J. 474 (2023) 145862.

[207] W. Wang, L.Y. Huai, S.Y. Wu, J.W. Shan, J.L. Zhu, Z.G. Liu, L.G. Yue, Y.Y. Li, Ultrahigh-volumetric-energy-density lithium-sulfur batteries with lean electrolyte enabled by cobalt-doped $MoSe_2$/$Ti_3C_2T_x$ MXene bifunctional catalyst, ACS Nano 15 (2021) 11619–11633.

[208] Z.Q. Ye, Y. Jiang, L. Li, F. Wu, R.J. Chen, Enhanced catalytic conversion of polysulfide using 1D CoTe and 2D MXene for heat-resistant and lean-electrolyte Li-S batteries, Chem. Eng. J. 430 (2022) 132734.

[209] S.H. Tian, J.J. Huang, H.C. Yang, G. Liu, Q. Zeng, D. Wang, X. Sun, K. Tao, G. H. Liu, S.L. Peng, Self-supporting multicomponent hierarchical network aerogel as sulfur anchoring-catalytic medium for highly stable lithium-sulfur battery, Small 18 (2022) 2205163.

[210] X.D. Hong, J. Mei, L. Wen, Y.Y. Tong, A.J. Vasileff, L.Q. Wang, J. Liang, Z.Q. Sun, S.X. Dou, Nonlithium metal-sulfur batteries: Steps toward a leap, Adv. Mater. 31 (2019) 1802822.

[211] W. Bao, C.E. Shuck, W. Zhang, X. Guo, Y. Gogotsi, G. Wang, Boosting performance of Na-S batteries using sulfur-doped $Ti_3C_2T_x$ MXene nanosheets with a strong affinity to sodium polysulfides, ACS Nano 13 (2019) 11500–11509.

[212] Y.J. Lei, H.L. Yang, Y.R. Liang, H.W. Liu, B.W. Zhang, L. Wang, W.H. Lai, Y. X. Wang, H.K. Liu, S.X. Dou, Progress and prospects of emerging potassium-sulfur batteries, Adv. Energy Mater. 12 (2022) 2202523.

[213] F.C. Zheng, Y.H. Zhang, G.H. Ding, Y. Xiao, L.Z. Wei, J.W. Su, C.L. Wang, Q. W. Chen, H. Wang, Pentagon defects accelerating polysulfides conversion enabled high-performance sodium-sulfur batteries, Adv. Funct. Mater. 34 (2023) 2310598.

[214] X.M. Yuan, B. Zhu, J.K. Feng, C.G. Wang, X. Cai, K. Qiao, R.M. Qin, Electrochemical insights, developing strategies, and perspectives toward advanced potassium-sulfur batteries, Small 16 (2020) 2003386.

[215] W. Bao, R. Wang, C. Qian, Z. Zhang, R. Wu, Y. Zhang, F. Liu, J. Li, G. Wang, Porous heteroatom-doped $Ti_3C_2T_x$ MXene microspheres enable strong adsorption of sodium polysulfides for long-life room-temperature sodium-sulfur batteries, ACS Nano 15 (2021) 16207–16217.

[216] N. Li, Y.L. Zhan, H.S. Wu, J. Fan, J.F. Jia, Synergistically boosting the anchoring effect and catalytic activity of MXenes as bifunctional electrocatalysts for sodium-sulfur batteries by single-atom catalyst engineering, Nanoscale 15 (2023) 2747–2755.

[217] B.S. Reddy, G.B. Cho, N.S. Reddy, H.J. Ahn, J.H. Ahn, T. Maiyalagan, K.K. Cho, Layered-like structure of TiO_2-Ti_3C_2 MXene as an efficient sulfur host for room-temperature sodium-sulfur batteries, J. Alloy. Compd. 883 (2021) 160910.

[218] S.Y. Qian, Z.Y. Yuan, G.S. Li, D.D. Li, J.Z. Li, W. Han, 3d layered structure $Ti_3C_2T_x$ MXene/$Ni(OH)_2$/C with strong catalytic and adsorption capabilities of polysulfides for high-capacity sodium-sulfur battery, Chem. Eng. J. 471 (2023) 144528.

[219] Z.F. Huang, S.J. Wang, X. Guo, J. Safaei, Y.J. Lei, W.H. Lai, X.Y. Zhang, B. Sun, D. Shanmukaraj, M. Armand, T. Rojo, G.X. Wang, A hierarchical hybrid MXenes interlayer with triple function for room-temperature sodium-sulfur batteries, Adv. Mater. Technol. 8 (2023) 2202147.

[220] C.Z. Wang, K.H. Wu, J.Q. Cui, X.L. Fang, J. Li, N.F. Zheng, Robust room-temperature sodium-sulfur batteries enabled by a sandwich-structured MXene@c/polyolefin/MXene@c dual-functional separator, Small 18 (2022) 2106983.

[221] R. Pai, V. Natu, M. Sokol, M. Carey, T. Greszler, M.W. Barsoum, V. Kalra, Sulfur confined MXene hosts enabling the use of carbonate-based electrolytes in alkali metal (Li/Na/K)-sulfur batteries, Mater. Today Energy 27 (2022) 101000.

[222] X. Tang, D. Zhou, P. Li, X. Guo, B. Sun, H. Liu, K. Yan, Y. Gogotsi, G.X. Wang, MXene-based dendrite-free potassium metal batteries, Adv. Mater. 32 (2020) 1906739.

[223] H. Shahali, R. Sellers, A. Rafieerad, A.A. Polycarpou, A. Amiri, Progress and prospects of zinc-sulfur batteries, Energy Storage Mater. 65 (2024) 103130.

[224] M.M. Gross, A. Manthiram, Rechargeable zinc-aqueous polysulfide battery with a mediator-ion solid electrolyte, ACS Appl. Mater. Interfaces 10 (2018) 10612–10617.

[225] K.K. Sonigara, J.V. Vaghasiya, C.C. Mayorga-Martinez, M. Pumera, Flexible aqueous Zn-S battery based on an S-decorated $Ti_3C_2T_x$ cathode, NPJ 2D Mater, Appl. 7 (2023) 45.

[226] H. Xu, D. Zhu, W. Zhu, F.Z. Sun, J.X. Zou, R.M. Laine, W.J. Ding, Rational design of high concentration electrolytes and MXene-based sulfur host materials toward high-performance magnesium sulfur batteries, Chem. Eng. J. 428 (2022) 131031.

[227] Q.N. Zhao, R.H. Wang, Y.X. Zhang, G.S. Huang, B. Jiang, C.H. Xu, F.S. Pan, The design of Co_3O_4@MXene heterostructure as sulfur host to promote the electrochemical kinetics for reversible magnesium-sulfur batteries, J. Magnes. Alloy. 9 (2021) 78–89.

[228] Y. Guo, H.C. Jin, Z.K. Qi, Z.Q. Hu, H.X. Ji, L.J. Wan, Carbonized-MOF as a sulfur host for aluminum-sulfur batteries with enhanced capacity and cycling life, Adv. Funct. Mater. 29 (2019) 1807676.

[229] X. Zheng, Z.L. Wang, J.J. Li, L.M. Wei, Binder-free S@$Ti_3C_2T_x$ sandwich structure film as a high-capacity cathode for a stable aluminum-sulfur battery, Sci. China Mater. 65 (2022) 1463–1475.

[230] Z.L. Wang, X. Zheng, A. Chen, Y.Q. Han, L.M. Wei, J.J. Li, Unraveling the anchoring effect of MXene-supported single atoms as cathodes for aluminum-sulfur batteries, ACS Mater. Lett. 4 (2022) 1436–1445.

[231] Q.J. Yang, T.T. Yang, W. Gao, Y.R. Qi, B.S. Guo, W. Zhong, J. Jiang, M.W. Xu, An MXene-based aerogel with cobalt nanoparticles as an efficient sulfur host for room-temperature Na-S batteries, Inorg. Chem. Front. 7 (2020) 4396–4403.